Title

TEMPERATURE DEPENDENCE OF THE HYPERFINE INTERACTION IN DILUTE NICKEL ALLOYS USING GAMMA-GAMMA PERTURBED ANGULAR CORRELATION

Author

Rosenblum, Stephen Saul.

Publication Date

1969

UCRL-18675

ey 2

TEMPERATURE DEPENDENCE OF THE HYPERFINE INTERACTION IN DILUTE NICKEL ALLOYS USING GAMMA-GAMMA PERTURBED ANGULAR CORRELATION

Stephen Saul Rosenblum
(Ph. D. Thesis)

January 1969

LAWRENCE RADIATION LABORATORY
UNIVERSITY of CALIFORNIA BERKELEY

UCRL-18675

ey 2

DISCLAIMER

"There are more things in heaven and earth, Horatio, than are dreamt of in your philosophy."

Hamlet, Act I

TABLE OF CONTENTS

CONTENTS (continued)

TEMPERATURE DEPENDENCE OF THE HYPERFINE INTERACTION IN DILUTE NICKEL ALLOYS USING GAMMA-GAMMA PERTURBED ANGULAR CORRELATION

Stephen Saul Rosenblum*

Department of Chemistry, and Lawrence Radiation Laboratory
University of California, Berkeley, California 94720

January 1969

ABSTRACT

Perturbed angular correlation studies of temperature-dependent hyperfine fields at ^{111}Cd, ^{99}Ru, and ^{100}Rh solutes in nickel above and below the Curie point are presented. For ^{111}Cd<u>Ni</u> it is found that the hyperfine field is proportional to the lattice magnetization over the entire range of temperatures studied. For ^{99}Ru<u>Ni</u> this is not the case, and a molecular field model is described which accounts for this behavior by postulating a local moment on the ruthenium atom. For ^{100}Rh<u>Ni</u> all data was taken for $T_c \lesssim T \leq 1.2\ T_c$ and the hyperfine field was found to be proportional to the lattice magnetization. In addition, a time dependent interaction is seen in this case, which is accounted for by a model based on the exchange-narrowing of a broadened Zeeman transition. Angular-correlation apparatus capable of 0.1% accuracy and a furnace capable of ±.5°C stability over 24 hours for use with this apparatus are also described.

I. INTRODUCTION

Since the discovery of hyperfine fields in ferromagnetic metals,[1,2] these interactions have proven themselves to be sensitive probes of the detailed behavior of electronic wave functions. Since the rigorous explication of the hyperfine structure of a metal requires the solution of the many-body problem it has not yet been done. As in all problems which cannot be solved exactly, one tries to determine the most important interactions. It is here that the experimental work has provided an understanding of the major mechanisms that give rise to hyperfine fields in ferromagnets.

In fact, in recent years, these mechanisms have apparently become well enough understood that hyperfine fields are being used as a tool to study metals. Since the discovery by Samoilov, Sklyarevskii, and Stepanov[3] that hyperfine fields also occur at nuclei of "nonmagnetic" metals as solutes in ferromagnets the range of application of hyperfine fields has expanded greatly. Solute fields are of considerable interest because they can be used to study separately the particular interactions that give rise to hyperfine fields.

The techniques that have been used to investigate these fields include nuclear magnetic resonance (NMR), both by continuous wave and pulse techniques, Mössbauer effect, nuclear orientation, nuclear specific heat, and the technique used here, perturbed angular correlation (PAC). Recent review articles describe and compare these techniques in detail.[4,5]

Of these methods, the NMR technique has provided results of the highest accuracy. As experimental methods have improved, the technique

of time differential perturbed angular correlations (TDPAC) has become competitive with NMR in accuracy. The work on ^{111}Cd described here is accurate to a few tenths percent. TDPAC and NMR are formally equivalent, the correlation function being the Fourier transform of the NMR line shape. TDPAC has the advantages over NMR of wider applicability (any temperature, pressure, and magnetic field) and much higher sensitivity.

In the TDPAC technique, one examines the multipole radiation pattern of a nuclear cascade. In the absence of external perturbation, the angular distribution of two γ-transitions in cascade can be predicted exactly from angular momentum theory and is given by a sum of Legendre polynomials. If one applies a perturbation to the intermediate state, the pattern will rotate. For all cases described in this paper, this rotation arises from the interaction of the nuclear dipole moment and the electronic magnetic hyperfine field. For such a system, the magnetic dipole precesses in the static field at the Larmor frequency. In a TDPAC experiment we observe this precession as a function of time. A more rigorous discussion of these points will be given in Section II.

All the data reported here have been taken by the TDPAC technique except for that on ^{99}Ru<u>Ni</u> above the Curie point which was taken by the less accurate time-integral perturbed angular correlation method. The hyperfine fields of ^{111}Cd in nickel and ^{99}Ru in nickel were investigated over the temperature range of 4°K to 725°K. The case of ^{111}Cd<u>Ni</u> shows a particularly simple behavior, the hyperfine field being proportional to the lattice magnetization over the entire temperature range. A simple conduction electron polarization model is described to account for this.

The hyperfine field of ^{99}Ru in Ni deviates markedly from the lattice magnetization. A similar behavior was seen in the temperature dependence of the hyperfine field of ^{55}Mn in iron[6] and described by Jaccarino, Walker and Wertheim[7] using a molecular field model with a local moment on the Mn atom. The data on ^{99}Ru are, to our knowledge, the first determinations of the temperature dependence of the hyperfine field of a 4d impurity in a ferromagnet. A molecular field model is used to describe this behavior, which, along with Jaccarino et al.,[7] assumes a local moment on the Ru atom, but also takes account of the expected large contribution of conduction electron polarization to the hyperfine field.

On the basis of systematics discussed in Section III, ^{100}Rh in nickel is also expected to show local moment behavior similar to that of ^{99}Ru<u>Ni</u>. Since the hyperfine interaction is very large in ^{100}Rh, it was only possible to carry out measurements above the Curie point where it is seen that the hyperfine field is proportional to the lattice magnetization indicating that there is <u>no</u> local moment above the Curie point.

Because of the very large hyperfine interaction and long lifetime of the intermediate state in ^{100}Rh, a time dependent interaction is seen here which is described by a model employing the theory of exchange narrowing of a broadened Zeeman transition. This model, using the molecular field approximation, predicts that the relaxation rate should be proportional to the square of the induced lattice magnetization, a prediction which is substantiated by the measurements.

II. PAC FORMALISM

Because several treatments of the theory of γ-γ PAC are available,[8-10] the discussion presented here will be given principally in the interest of completeness. In addition to the published works cited in refs. 8-10 the author is indebted to two sets of unpublished lecture notes by R. M. Steffen which greatly clarified his own understanding of the formalism. One set was compiled at the Tata Institute of Fundamental Research[11] and the second (and more detailed set) at Purdue University.[12] The treatment in these notes forms the substance of the outline given here.

The most general type of correlation function describes the relationship between two coherent quantum mechanical transitions of a system. Examples of nuclear systems described by correlation functions are angular distributions following nuclear reaction, Coulomb excitation, particle-particle correlations, particle-gamma correlations, and gamma-gamma correlations. In the simplest case, one measures only the direction of emission (or absorption) of the quanta. This is a <u>directional correlation</u>. If one measures the polarization of one of the emissions in addition, one has a <u>polarization-directional correlation</u>. If one measures the polarization of both transitions one has a <u>polarization-polarization</u> correlation.

The formalism for describing all these experiments is exactly the same. The theory, as described here, makes use of three principal tools: 1) the rotation matrices, $D^{L}_{M\mu}(\alpha,\beta,\gamma)$, 2) Racah algebra, 3) the density matrix.

1) The rotation matrices allow one to describe the two transitions with respect to convenient quantization axes. After the matrix elements are calculated with respect to these convenient axes, we can use the $D^{L}_{M\mu}(\alpha,\beta,\gamma)$ to rotate them so that the emitted radiations appear in the desired observation directions. This procedure is acceptable because the Hamiltonian is a scalar operator and is thus rotationally invariant.

2) Racah algebra, as developed by Gardner,[13] allows the summation over m-substates to be carried out and written down in closed form.

3) The density matrix formalism was first applied to angular correlations by Fano[14] and by Coester and Jauch.[15,16] This mathematical tool permits a very elegant treatment of two principal problems of angular correlation of nuclear radiations. First, since nuclei may decay by a transition of mixed multipolarity (e.g. M1-E2), one is often dealing with an impure state. Second, one is almost never able to examine a single nucleus, but must look at an ensemble, all of whose members are developing in time in a purely statistical manner. This incoherent mixture of impure states can be described without any simplification by direct application of this simple and powerful mathematical tool.

A. The Unperturbed Correlation Function

In order to clarify the discussion we will consider the gamma cascade shown in Fig. II-1. (This can be easily generalized, however, to any type of correlation.) In this case we begin with an initial nuclear state described by a density matrix ρ_i with total angular momentum (or "spin") I_i and with $(I_i)_z = m_i$. Using bra and ket notation, we have

$|I_i m_i\rangle$. This state decays to the intermediate level via radiation R_1 in direction $(\vec{k}_1)$, producing a state $|Im\rangle$ described by density matrix $\rho(\vec{k}_1)$. This state, in turn, decays via radiation R_2 in direction $\vec{k}_2$ to the final state $|I_f m_f\rangle$ described by density matrix $\rho(\vec{k}_1,\vec{k}_2)$. Thus $\rho(\vec{k}_1,\vec{k}_2)$ describes <u>both</u> the nuclear ensemble and the radiation pattern.

Let H_1 be the Hamiltonian describing transition R_1 so that

$$\langle Im|\rho(\vec{k}_1)|Im'\rangle = S_1 \sum_{m_i m_i'} \langle Im|H_1|I_i m_i\rangle\langle I_i m_i|\rho_i|I_i m_i'\rangle \times \langle Im'|H_1|I_i m_i'\rangle^* \qquad \text{(II.1)}$$

where S_1 denotes summation over all unobserved properties.

Similarly, if H_2 is the Hamiltonian for the second transition,

$$\langle I_f m_f|\rho(\vec{k}_1,\vec{k}_2)|I_f m_f'\rangle = S_2 \sum_{mm'} \langle I_f m_f|H_2|Im\rangle\langle Im|\rho(\vec{k}_1)|Im'\rangle \times \langle I_f m_f'|H_2|Im'\rangle^* \qquad \text{(II-2)}$$

where S_2 denotes summation over all unobserved properties.

Substituting Eq. (II.1) in (II.2)

$$\langle I_f m_f|\rho(\vec{k}_1,\vec{k}_2)|I_f m_f'\rangle = S_1 S_2 \sum_{\substack{m_i m_i' \\ mm'}} \langle I_f m_f|H_2|Im\rangle\langle Im|H_1|I_i m_i\rangle \times \langle I_i m_i|\rho_i|I_i m_i'\rangle\langle Im'|H_1|I_i m_i'\rangle^*\langle I_f m_f'|H_2|Im'\rangle^* \qquad \text{(II.3)}$$

Let us only consider the case where the initial state is isotropic,

$$\langle I_i m_i|\rho_i|I_i m_i'\rangle = (2I_i + 1)^{-1}\,\delta_{m_i m_i'} \tag{II.4}$$

Also, since we will observe all orientations of the final state in a normal directional correlation experiment, we can sum over m_f.

Thus the correlation function is,

$$W(\vec{k}_1,\vec{k}_2) = \sum_{m_f} P(m_f) = \sum_{m_f} \langle I_f m_f|\rho(\vec{k}_1,\vec{k}_2)|I_f m_f\rangle \tag{II.4a}$$

where $P_f(m_f)$ is the probability of finding the nucleus in final state $|I_f m_f\rangle$. Thus,

$$W(\vec{k}_1,\vec{k}_2) = S_1 S_2 \sum_{\substack{m_f m_i \\ m\ m'}} \langle I_f m_f|H_2|Im\rangle\langle Im|H_1|I_i m_i\rangle$$

$$\times \langle Im'|H_1|I_i m_i\rangle^*\langle I_f m_f|H_2|Im'\rangle^* \tag{II.5}$$

We must now evaluate these matrix elements. Picking $\langle Im|H_1|I_i m_i\rangle$ as a typical example, the final state consists of the nucleus in state $|Im\rangle$ and plane wave $|\vec{k}\sigma\rangle$, in direction $\vec{k}$ with polarization σ.

Expanding the plane wave in spherical waves the matrix element becomes

$$\langle Im\vec{k}\sigma|H_1|I_i m_i\rangle = \sum_{L\,M\,\Pi} \langle Im\vec{k}\sigma|L\,M\,\Pi\rangle\langle Im\;L\,M\,\Pi|H_1|I_i m_i\rangle \qquad (II.5a)$$

If we now separate this function into a nuclear part and a radiation part, and make use of the Wigner-Eckart theorem we can evaluate the matrix element:

$$\langle Im\vec{k}\sigma|H_1|I_i m_i\rangle = \sum_{L\,\Pi} (-1)^{-I+L-m_i} \begin{pmatrix} I & L & I_i \\ m & M & -m_i \end{pmatrix}$$

$$\times \langle \vec{k}\sigma|L\,M\,\Pi\rangle\langle I\|(L\,\Pi)\|I_i\rangle \qquad (II.6)$$

Now, we make use of the rotation matrices to transform the radiation from an arbitrary z-axis to the direction of emission,

$$\langle Im\vec{k}\sigma|H_1|I_i m_i\rangle = \sum_{L\,\mu\,\Pi} (-1)^{-I+L-m_i} \begin{pmatrix} I & L & I_i \\ m & M & -m_i \end{pmatrix}$$

$$\times \langle 0\sigma|L\,\mu\,\Pi\rangle\, D^{L^*}_{M\mu}\,(\vec{z}\rightarrow\vec{k})\langle I\|(L\,\Pi)\|I_i\rangle \qquad (II.7)$$

This is the desired result. If we now carry out the same procedure for the other three matrix elements, perform some Racah algebra to carry out the summations over m-substates we obtain the expression for the <u>unperturbed correlation</u>,

$$W(\vec{k}_1,\vec{k}_2) = (-1)^{2I-I_i-I_f} \sum_{mm'} \sum_{k_1 k_2} \sum_{\substack{L_1 L_1' \\ L_2 L_2'}} \sum_{\substack{N_1 N_2 \\ \tau_1 \tau_2}} (-1)^{k_2-L_1'-L_2'}$$

$$\times [(2k_1+1)(2k_2+1)]^{1/2} \begin{pmatrix} I & I & k_1 \\ m' & -m & N_1 \end{pmatrix} \begin{pmatrix} I & I & k_2 \\ m' & -m & N_2 \end{pmatrix} \begin{Bmatrix} I & I & k_1 \\ L_1 & L_1' & I_i \end{Bmatrix}$$

$$\times \begin{Bmatrix} I & I & k_2 \\ L_2 & L_2' & I_f \end{Bmatrix} \langle I_f \| (L_2 \Pi_2) \| I \rangle \langle I_f \| (L_2' \Pi_2') \| I \rangle^*$$

$$\times \langle I \| (L_1 \Pi_1) \| I_i \rangle \langle I \| L_1' \Pi_1' \| I_i \rangle^*$$

$$\times C_{k_1 \tau_1}(L_1' L_1) C^*_{k_2 \tau_2}(L_2 L_2') \mathcal{D}^{k_1}_{N_1 \tau_1}(\vec{z} \to \vec{k}_1) \mathcal{D}^{k_2^*}_{N_2 \tau_2}(\vec{z} \to \vec{k}_2) \tag{II.8a}$$

where the $C_{k\tau}(L'L)$, the radiation parameters, are given by

$$C_{k\tau}(LL') = S \sum_{\mu\mu'} (-1)^{L'-\mu'} (2k+1)^{1/2} \begin{pmatrix} L & L' & k \\ \mu & -\mu' & \tau \end{pmatrix} \langle O\sigma | L\, \mu\, \Pi \rangle \langle O\sigma' | L' \mu' \Pi' \rangle^* \tag{II.8b}$$

These radiation parameters contain <u>all</u> the information about the properties of the radiation which are observed in the experiment.

Since, in Eq. (II.8a), only the 3-j symbols depend on m and m', the summation over m and m' can be easily carried out using the orthogonality relation for 3-j symbols. This will not be done, however, since we wish to determine the <u>perturbed</u> correlation function. The perturbation

mixes up the m-substates and no longer allows us to perform this summation easily.

If we now specialize this expression to directional correlations $\tau_1 = \tau_2 = 0$, and eliminate extraneous phase factors,

$$W(k_1,k_2) = \sum_{mm'} \sum_{k_1 k_2} \sum_{N_1 N_2} \begin{pmatrix} I & I & k_1 \\ m' & -m & N_1 \end{pmatrix} \begin{pmatrix} I & I & k_2 \\ m' & -m & N_2 \end{pmatrix} (2)$$

$$\times A'_{k_1}(L_1 L_1' I_i I)\, A'_{k_2}(L_2 L_2' I_f I)\, Y^{N_1^*}_{k_1}(\vec{k}_1)\, Y^{N_2}_{k_2}(\vec{k}_2) \qquad (II.9)$$

where

$$A'_{k_1}(L_1 L_1' I_i I) = \sum_{L_1 L_1'} (-1)^{L_1} C^*_{k0}(L_1 L_1') \begin{Bmatrix} I & I & k_1 \\ L_1 & L_1' & I_i \end{Bmatrix} \langle I \| (L_1 \Pi_1) \| I_i \rangle$$

$$\times \langle I \| (L_1' \Pi_1') \| I_i \rangle^* \qquad (II.9a)$$

and likewise for $A'_{k_2}(L_2 L_2' I_f I)$. These A'_{k_i} are not yet normalized.

B. The Perturbed Directional Correlation Function for Static Interaction

If we now go through this derivation again, but remove the restriction that the density matrix for the second transition is the same matrix that is produced by the first transition, i.e., if we allow the density matrix of the intermediate state to change in time, we can arrive at the formalism for perturbed directional correlations.

It is a general result that if the evolution of a density matrix is caused by a time-independent Hamiltonian, the density matrix at time t is given by

$$\rho(t) = e^{-iKt/\hbar}\, \rho(t=0) e^{+iKt/\hbar}$$

where K is the Hamiltonian of the interaction.

Thus

$$\rho(\vec{k}_1,t) = e^{-iKt/\hbar}\, \rho(\vec{k}_1,t=0) e^{+iKt/\hbar}$$

where $\rho(\vec{k}_1,t=0)$ is the density matrix produced by the first transition.

All we need do now is replace the matrix element $\langle Im|\rho(\vec{k}_1)|Im'\rangle$ in Eq. (II.2) with this result. This gives

$$\begin{aligned}\langle I_f m_f|\rho(\vec{k}_1,\vec{k}_2,t)|I_f' m_f'\rangle = S_2 \sum_{m_a m_b} & \langle I_f m_f|H_2|I_a m_a\rangle \\ & \times \langle Im_a|e^{-iKt/\hbar}\, \rho(\vec{k}_1,t=0)\, e^{+iKt/\hbar}\, |Im_b\rangle \\ & \times \langle I_f m_f'|H_2|Im_b\rangle^* \end{aligned} \qquad \text{(II.10)}$$

If we now make use of the properties of the projection operator, $\sum_m |Im\rangle\langle Im|$,[17] set $\Lambda(t) = e^{-iKt/\hbar}$ and insert the expression for $\langle Im|\rho(\vec{k}_1,t=0)|Im'\rangle$ from Eq. (II.1), we get

$$\langle I_f m_f|\rho(\vec{k}_1,\vec{k}_2,t)|I_f m_f'\rangle = \sum_{m_i m_i'} \sum_{mm'} \sum_{m_a m_b} \langle I_f m_f|H_2|Im_a\rangle$$

$$\times \langle Im_a|\Lambda(t)|Im\rangle\langle Im|H_1|I_i m_i\rangle\langle I_i m_i|\rho_i|I_i m_i'\rangle$$

$$\times \langle Im'|H_1|I_i m_i'\rangle^*\langle Im'|\Lambda^*(t)|Im_b\rangle\langle I_f m_f'|H_2|Im_b\rangle^* \qquad (II.11)$$

If we again make the assumption that the initial density matrix is isotropic and summing over final states we find

$$W(\vec{k}_1,\vec{k}_2,t) = S_1 S_2 \sum_{m_f m_i} \sum_{mm'} \sum_{m_a m_b} \langle I_f m_f|H_2|Im_a\rangle\langle Im|H_1|I_i m_i\rangle$$

$$\times \langle Im'|H_1|I_i m_i\rangle^*\langle I_f m_f|H_2|Im_b\rangle^*$$

$$\times \langle Im_a|\Lambda(t)|Im\rangle\langle Im_b|\Lambda(t)|Im'\rangle^* \qquad (II.12)$$

This is the same result as found in Eq. (II.5) except that we have inserted a coupling matrix

$$\langle Im_a m_b|G(t)|Imm'\rangle = \langle Im_a|\Lambda(t)|Im\rangle\langle Im_b|\Lambda(t)|Im'\rangle^* \qquad (II.13)$$

If we proceed the same way as before, we obtain an equation analogous to Eq. (II.9)

$$w(\vec{k}_1,\vec{k}_2,t) = \sum_{\substack{k_1 k_2 \\ N_1 N_2}} A_{k_1}(L_1 L_1' I_i I)\, A_{k_2}(L_2 L_2' I_f I)[(2k_1+1)(2k_2+1)]^{-1/2}$$

$$\times\ G^{N_1 N_2}_{k_1 k_2}(t)\, Y^{N_1 *}_{k_1}(\vec{k}_1)\, Y^{N_2}_{k_2}(\vec{k}_2) \qquad \text{(II.14)}$$

where the A_{k_i} are those given in Eq. (II.9a) but have been normalized so that $A_o\,(LL'I_1I_2) = 1$ and

$$G^{N_1 N_2}_{k_1 k_2}(t) = \sum_{m_1 m_a} (-1)^{2I+m_a+m_b}[(2k_1+1)(2k_2+1)]^{1/2} \begin{pmatrix} I & I & k_1 \\ m' & -m & N_1 \end{pmatrix}$$

$$\times \begin{pmatrix} I & I & k_2 \\ m_b & -m_a & N_2 \end{pmatrix} \langle Im_a|\Lambda(t)|Im\rangle \langle Im_b|\Lambda(t)|Im'\rangle^* \qquad \text{(II.15)}$$

This is the general form of the perturbation factor for static fields.

1. Perturbation Factor for Special Cases

In order to evaluate the perturbation factor one must first find the eigenvalues and eigenvectors of $\Lambda(t)$ in the $|Im\rangle$ representation.

a. Axially symmetric interaction. If the interaction is axially symmetric it can be easily shown that[8,10,11,12]

$$G_{k_1k_2}^{N_1N_2}(t) = G_{k_1k_2}^{NN}(t) = \sum_{mm'} [(2k_1+1)(2k_2+1)]^{1/2} \begin{pmatrix} I & I & k_1 \\ m' & -m & N \end{pmatrix} \begin{pmatrix} I & I & k_2 \\ m' & -m & N \end{pmatrix}$$

$$\times e^{-i(E_m - E_{m'})t/\hbar} \qquad \text{(II.16)}$$

provided that the axis of symmetry is chosen as the quantization axis. The total time-integrated attenuation factor for this case is

$$\overline{G_{kk}(\infty)} = \sum_m \begin{pmatrix} I & I & k \\ m' & -m & N \end{pmatrix}^2 \left[1 + \left(\frac{E_m - E_{m'}}{\hbar} t \right)^2 \right]^{-1} \qquad \text{(II.16a)}$$

If one has a collection of microcrystals, the interaction is randomly oriented. If the interaction has axial symmetry, one integrates over all angles and obtains

$$G_{k_1k_2}^{N_1N_2}(t) = G_{kk}(t) = [2k+1]^{-1} + \sum_{p\neq 0} \begin{pmatrix} I & I & k \\ m' & -m & p \end{pmatrix}^2 \cos \left(\frac{E_m - E_{m'}}{\hbar} \right) t$$

$$= (2k+1)^{-1} \sum_N G_{kk}^{NN}(t) \qquad \text{(II.17)}$$

The total time integrated attenuation factor for this case is the same as Eq. (II.16a).

b. Static magnetic fields. For a static magnetic field,

$$E_m - E_{m'} = -Ng\mu_N H$$

Substituting this in Eq. (II.16) and using the orthogonality relation of 3-j symbols, we get

$$G_{kk}^{NN}(t) = e^{-iN\omega_L t} \tag{II.18}$$

where $\omega_L = \frac{g\mu_N H}{\hbar}$ is the Larmor frequency.

The directional correlation for the case in which the external field, H, is perpendicular to the detector plane becomes

$$W_{\perp}(\theta,t,H) = \sum_{\substack{k=0 \\ \text{even}}}^{k_{max}} A_k(R_1)A_k(R_2)P_k[\cos(\theta-\omega_L t)] \tag{II.19}$$

where θ is the angle between the detectors.

The total time-integrated attenuation factor for this case is, from Eq. (II.16a)

$$\overline{G_{kk}^{NN}(\infty,H)} = \{(2k+1)[1 + (N\omega_L\tau)^2]\}^{-1} \tag{II.19a}$$

For a randomly oriented magnetic interaction, from Eq. (II.17) one obtains the attenuation factor

$$G_{kk}(t) = (2k+1)^{-1}\sum_N G_{kk}^{NN}(t) = (2k+1)^{-1}\sum_N \cos N\omega_L t \tag{II.20}$$

which, in turn, leads to a correlation function of the form

$$W(\theta,t) = (4\Pi)^{-1} \sum_k A_k(R_1)A_k(R_2) \left[(2k+1)^{-1} \sum_N \cos N\omega_L t \right] P_k(\cos\theta) \tag{II.21}$$

Again, θ is the angle between the detectors.

The time-integrated attenuation factor for this case is the same as that given in Eq. (II.19a).

C. The Perturbed Directional Correlation Function for Combined Static and Time Dependent Interaction - The Superoperator Formalism

In recent work by Helmut Gabriel[18] a new theoretical approach to the calculation of the perturbation factor has been developed.

In this treatment, one works in a Liouville space spanned by the normalized spherical tensor operators, $U_N^{(k)}$. In this space the perturbation factor $G_{k_1k_2}^{N_1N_2}(t)$ becomes a time-dependent superoperator transforming the spherical tensor $U_{N_1}^{(k_1)}$ to the tensor $U_{N_2}^{(k_2)}$. Thus Eq. (II.14) can be written

$$W(\vec{k}_1,k_2,t) = \sum_{\substack{k_1N_1 \\ k_2N_2}} \left(\rho(\vec{k}_2)|U_{N_2}^{(k_2)}\right)\left(U_{N_2}^{(k_2)}|\hat{\Omega}(t)|U_{N_1}^{(k_1)}\right) \times \left(U_{N_1}^{(k_1)} \mid \rho(\vec{k}_1,t=0)\right) \tag{II.22}$$

where

$$G^{N_1N_2}_{k_1k_2}(t) = \left(U^{(k_2)}_{N_2} \,|\, \hat{\Omega}(t) \,|\, U^{(k_1)}_{N_1} \right)$$

and

$$\left(\rho(k)|U^{(k)}_N\right) = A_k \, Y^N_k(\theta,\phi) \, [4\Pi/(2k+1)]^{1/2} \qquad \text{(II.22a)}$$

Aside from the greatly simplified notation, this change of representation also provides a convenient form for deriving the symmetry relations and general properties of the perturbation matrix $G^{N_1N_2}_{k_1k_2}(t)$.

The details of the derivation are too complex to present here and the reader is referred to Gabriel's paper[18] for them. Gabriel's treatment also separates the density matrix of the coupled nuclear and electronic system into a nuclear part and an average over the unobserved electronic part using Zwanzig's projection operator technique.[19] The properties of the electrons and any applied fields enter the theory via second-order correlation functions, which are defined in terms of thermal equilibrium ensemble averages of the operators describing these interactions.

The results which Gabriel derives, which are of specific interest for the work presented here, are applicable under the following restrictions:

1) Purely magnetic interactions with the nucleus

2) High temperature limit, i.e., $\hbar\omega_L \ll kT$

3) $\tau_c \ll (\tau_N, \omega_L^{-1}, T_1, T_2)$ i.e., the correlation time of the electrons is much shorter than any other time of interest.

The time differential perturbation factor is given by

$$G_{kk}^{NN}(t) = e^{-i\nu_{kN}t-\lambda_{kN}t} \qquad \text{(II.23)}$$

where

$$\nu_{kN} = N\omega_L$$

$$\lambda_{kN} = (g\mu_N)^2 \left\{ N^2\left[J_{10}^{10}(0) + J_{1\bar{1}}^{11}(-\omega_L)\right] - k(k+1)\, J_{1\bar{1}}^{11}(-\omega_L)\right\}$$

$$J_{10}^{10}(\omega) = \frac{1}{2}\int_{-\infty}^{\infty} dt\, e^{i\omega t} \left\langle \frac{1}{2}\left[h_z(t),\, h_z(0)\right]_+ \right\rangle_R$$

$$J_{1\bar{1}}^{11}(\omega) = -\frac{1}{2}\int_{-\infty}^{\infty} dt\; e^{i\omega t} \left\langle \frac{1}{2}\left[h_+(t),\, h_-(0)\right]_+ \right\rangle_R$$

$$h = \vec{H}_{eff} - \langle H_{eff}\rangle_R \qquad \text{(II.23)}$$

The J's are the spectral density functions which are the Fourier transforms of the ensemble averages of the magnetic fluctuations, the correlation functions.

The main difference between this result and that of Abragam and Pound[20] is that there is a different value of λ_{kN}, the relaxation constant, for each multipole orientation.

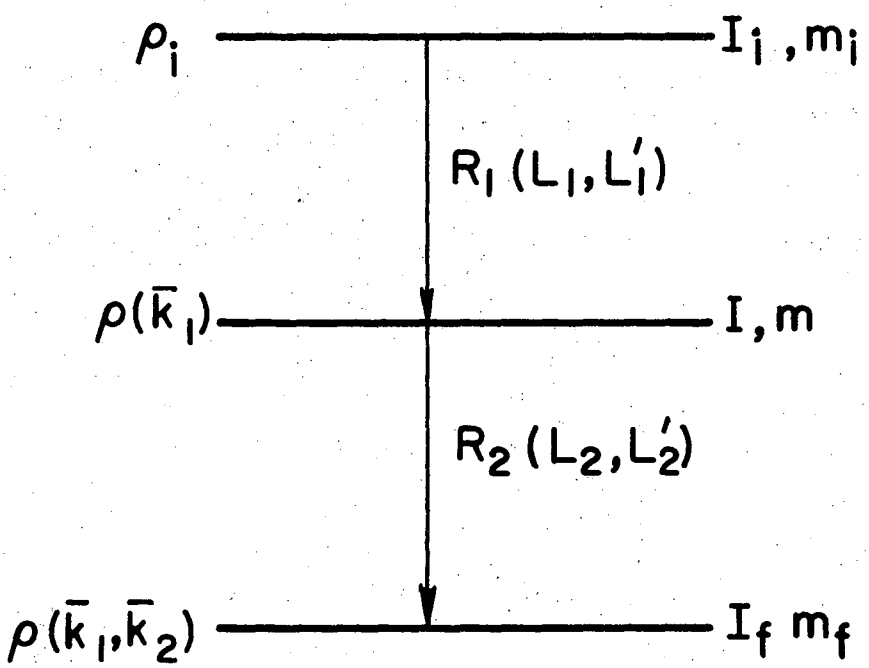
ρ_i
I_i, m_i
$R_1 (L_1, L_1')$
$\rho(\bar{k}_1)$
I, m
$R_2 (L_2, L_2')$
$\rho(\bar{k}_1, \bar{k}_2)$
$I_f\ m_f$
XBL6812-7497

Figure II.1

III. HYPERFINE FIELDS IN FERROMAGNETS

A. Formal Hamiltonian

A completely rigorous understanding of hyperfine interactions in ferromagnets awaits further theoretical work on the many-body problem. In order to point out the approximations which are presently made to obtain a tractable theoretical model, it is best to write down a formal Hamiltonian for the problem and then simplify it. A Hamiltonian which is applicable to both a ferromagnetic host metal and solutes is:[21]

$$\mathcal{H} = V_{cf} + 2\beta\vec{H}_{ex} \cdot \vec{S} + \lambda\vec{L} \cdot \vec{S} - \gamma_I\vec{H}_c \cdot \vec{I}$$

$$+ 2\beta\gamma_I\langle r^{-3}\rangle \{\vec{L} \cdot \vec{I} + [\xi L(L+1) - \kappa]\, \vec{S} \cdot \vec{I}$$

$$- \frac{3}{2}\xi\, [(\vec{L} \cdot \vec{S})(\vec{L} \cdot \vec{I}) + (\vec{L} \cdot \vec{I})(\vec{L} \cdot \vec{S})]\} \qquad \text{(III.1)}$$

where β is the Bohr Magneton.

In using this Hamiltonian we pick a particular atom, characterized by the quantum numbers L, S, and I, acted upon by all the other atoms in the lattice characterized by V_{cf}, the crystal field interaction, $\vec{H}_{ex}$, the exchange field, and $\vec{H}_c$, the conduction electron polarization. The $\lambda\vec{L} \cdot \vec{S}$ term is the electronic spin-orbit interaction and the terms in curly brackets represent the magnetic hfs interaction in operator equivalent notation.[22] The $\vec{L} \cdot \vec{I}$ term represents the interaction of the electronic orbital magnetism with the nuclear spin, the $\kappa\vec{S}\cdot\vec{I}$ term, the core polarization and the three terms in ξ the interaction of the electronic spin

with the nuclear spin. $\langle r^{-3} \rangle$ is evaluated for all unfilled atomic shells on the atom in question.

The first three terms are the largest and must be evaluated first to give the zero order wave functions. Except for rare earth solutes, the $\lambda \vec{L} \cdot \vec{S}$ is smaller than the other two terms, leading to a good deal of simplification. The rare earth case will not be discussed here. The reader is referred to recent work by Shirley et al.[21] for this case.

For the situation in which the spin-orbit coupling is smaller than both the crystal field and the exchange field (which obtains for all cases described in this paper), we can assume that the electronic orbital angular momentum is quenched by the crystal field. If we restrict ourselves to cubic lattices, we can rewrite our Hamiltonian, Eq. (III.1) as a sum of two parts,

$$\mathcal{H} = \mathcal{H}_1 + \mathcal{H}_2 \tag{III.2}$$

where $\mathcal{H}_1 = V_{cf}$, which determines the zero order wave functions and

$$\begin{aligned} \mathcal{H}_2 &= 2\beta \vec{H}_{ex} \cdot \vec{S} - \gamma_I \vec{H}_c \cdot \vec{I} - 2\beta\gamma_I \langle r^{-3} \rangle \kappa \vec{S} \cdot \vec{I} \\ &= 2\beta \vec{H}_{ex} \cdot \vec{S} - \gamma_I \vec{I} \cdot [\vec{H}_c + 2\beta \langle r^{-3} \rangle \kappa \vec{S}] \\ &= 2\beta \vec{H}_{ex} \cdot \vec{S} - \gamma_I \vec{I} \cdot \vec{H}_{hf} \end{aligned} \tag{III.2b}$$

The second term above is in the form of a magnetic field acting on the nuclear moment.

Of the terms in $\mathcal{H}_2$, the exchange term is the largest. We may imagine that it is evaluated first to give $\langle S_z \rangle$ allowing us to rewrite $\vec{H}_{hf}$ as a scalar

$$H_{hf} = H_c + 2\langle S_z \rangle H_d \qquad \text{(III.3)}$$

where $H_d = \beta\kappa\langle r^{-3} \rangle$, the core polarization hyperfine field arising from a single unpaired d-electron.

Following Shirley and Westenbarger[23] we write, $H_c = pH_{ns}$ where H_{ns} is the hyperfine field arising from a free atom ns state. This substitution is permissible because we expect that conduction band s-wave states resemble the atomic functions near the nucleus.

Thus our final equation is

$$H_{hf} = pH_{ns} + 2\langle S_z \rangle H_d \qquad \text{(III.4)}$$

The first term on the right is the conduction electron polarization (CEP) contribution and the second is the core polarization (CP) contribution, which arises only in cases where there are unpaired magnetic electrons (i.e., open p,d shells). This equation should be valid for all impurities in ferromagnets except for those with incomplete f-shells, because we assumed $V_{cf} >> \lambda \vec{L} \cdot \vec{S}$. This equation will be used later in this section to relate the appearance of local moments to large core polarization contributions to the solute hyperfine field.

B. Models for Ferromagnetic Metals

The exchange interaction is the underlying phenomenon of all ferromagnetic behavior. The most obvious macroscopic manifestation of ferromagnetic behavior is the spontaneous magnetization, the sample magnetization in the absence of an applied magnetic field.

In the case of iron, cobalt and nickel, the electrons involved in this exchange interaction are the unpaired d-electrons. If one considers that these d-electrons are localized on individual atoms (a reasonably good approximation) the spontaneous magnetization can be considered to arise from the summation of all the atomic moments. It is these same d-electrons which are also responsible for the large magnetic hyperfine fields at the nuclei of atoms in ferromagnets. In cubic ferromagnets, these fields arise principally from the Fermi contact interaction of s-electrons which have been polarized by the d-electrons. The mechanism by which this polarization is created is not quantitatively understood at present, but there is much theoretical endeavor directed toward such an understanding.[24] Because of this, most approaches to the explication of the behavior of magnetic hyperfine fields have made use of the theories used to describe macroscopic magnetization.

A theoretical justification for this assumption has been given by W. Marshall[25] and has been borne out in several cases cited in Sec. III.C.1. It is therefore useful to summarize here the characteristics of the principal models describing ferromagnetic behavior and to indicate some of their relative strengths and weaknesses.

The exchange interaction arises from purely electrostatic forces as a result of the Pauli exclusion principle and is written most generally as

$$\mathcal{H}_e = -2 \sum_{i \neq j} J_{ij} \vec{S}_i \cdot \vec{S}_j \qquad \text{(III.5)}$$

where J_{ij} is the strength of the interaction and S_i and S_j are electron spin operators. The summation is carried out for all atoms i with all other atoms $j \neq i$. The exchange interaction is not generally isotropic.

From this point, two basic approaches to the problem proceed. The historically older approach is based on the idea that the magnetic electrons are localized on individual atoms and are interacting principally with nearest neighbors. These models include the Weiss model (classical), the Heisenberg model, the Ising model, the spin-wave model, and the various types of cluster-expansion models.

The other approach is based on the idea that the magnetic electrons are itinerant, forming bands of spin-up and spin-down electrons which are split apart by the exchange interaction. These comprise principally models using time-dependent Green's functions.

Some of the strengths and weaknesses of these models will be pointed out here but no attempt will be made at completeness. Those interested in further enlightenment are heartily recommended to any of the many excellent books[26] on the subject.

1. Localized Electron Models

The Weiss molecular field model is the oldest (1907) description of ferromagnetic behavior still in active use. It is based on the idea that a molecular field of (at the time) unknown origin acts on an assembly of ideal paramagnets to produce a net magnetization, even in the absence of applied fields. This model gives the well-known Brillouin function dependence of magnetization on temperature.

Aside from its main advantage of conceptual simplicity and analytical solubility this model gives information on the entire range of temperature, above and below T_c. It is also found to be in good qualitative agreement with measurements on ferromagnetic systems. However, its detailed agreement is poor. Aside from this, it is not quantum-mechanical, so that it is not expected to lead to any microscopic understanding of cooperative phenomena.

Both the Ising and Heisenberg models provide information over all temperatures but have the disadvantage of not being exactly soluble for a 3-dimensional lattice. The Ising model is the simpler of the two, its Hamiltonian being

$$\mathcal{H}_I = -2 J_e \sum_{i \neq j} S_{zi} S_{zj} - g\beta H_o \sum_i \vec{S}_{zi} \qquad \text{(III.6)}$$

where H_o is an applied field.

The exchange interaction constant, J_e, is assumed to be isotropic and x and y spin components are replaced by their time averages,

assumed to be zero. This is a very tractable Hamiltonian since all operators in it commute.

The Heisenberg model retains the non-diagonial spin components, its Hamiltonian being

$$\mathcal{H}_H = -2J_e \sum_{i \neq j} \vec{S}_i \cdot \vec{S}_j + g\beta H_o \sum_i S_{zi} \qquad \text{(III.7)}$$

The exchange coupling constant is still assumed to be isotropic.

In calculations using these models one is usually required to carry out the first summation only over nearest or next neighbors in order to keep the calculation tractable. This is only valid to the extent that long range interactions can be neglected, a very dubious assumption in metallic ferromagnets. The predictive ability of these models is limited to a large extent by the ingenuity of the theoretician in making the correct approximations for the system under consideration, two of the most successful ones being the spin wave theory (valid only at low temperatures $T < T_c/10$) and the Bethe-Peierls-Weiss cluster expansion method (valid for $T \geq T_c$).

The spin wave model is based on the idea that the ground state of a ferromagnetic system is that in which all the spins are aligned parallel. The lowest excitation of this sytem would be the case in which a single spin is inverted. Simple considerations show that the exchange Hamiltonian does not permit this as an eigenstate. This deviation travels throughout the lattice as a collective spin excitation,

a magnon. This theory predicts a $T^{3/2}$ dependence of the spontaneous magnetization at low temperatures, in very good agreement with experiment.

The Bethe-Peierls-Weiss cluster expansion technique is based on the idea that in the neighborhood of the Curie temperature one can neglect the long-range order in the sample and evaluate the Heisenberg Hamiltonian only for the nearest neighbors to spin i and approximate the interaction of the rest of the atoms with this cluster by an effective field, i.e., the Hamiltonian is

$$\mathcal{H}_{BPW} = -2J_e \vec{S}_i \cdot \sum_{nn} \vec{S}_j - g\beta \vec{H}_f \cdot \sum_{nn} \vec{S}_j - g\beta \vec{H}_o \cdot \vec{S}_i \qquad \text{(III.8)}$$

where H_f is the effective field acting on the cluster.

This Hamiltonian neglects the interactions between nearest neighbors. This model gives good results for $T > T_c$ but for $T < T_c$ predicts a spontaneous magnetization increasing to a maximum and then dropping to zero as temperature decreases. The idea of the magnetic cluster has recently been exploited by Kouvel and Rodbell[27] in discussing magnetic fluctuations at the critical temperature.

2. Itinerant Electron Models

The earliest itinerant electron theory was that proposed by Stoner[28] based on a self consistent field solution for the Hamiltonian

$$\mathcal{H}_s(\vec{k},\sigma) = \varepsilon_k + \sum_{k',\sigma'} [V - \delta_{\sigma\sigma'}\, \nu(\vec{k}-\vec{k}')] n(k',\sigma') \qquad \text{(III.9)}$$

where ε_k is the energy of the unperturbed Bloch electrons, V is the electrostatic repulsion term, $\nu(k-k')$ is the exchange interaction between electrons of like spin, and $n(k'\sigma')$ is the density of electrons of quantum number (k',σ'). This model leads to an exchange splitting of the electrons near the Fermi surface into two bands.

The more recent approaches to this problem have made use of time-dependent Green's functions, a mathematical tool developed to treat the many-body problem in quantum electrodynamics. The essential element of this technique is that it allows a perturbation-theoretic approach to the solution of an essentially infinite set of coupled equations, i.e., those describing two body interactions, three body interactions, etc. It allows the summation of chosen interactions to infinite order--the evaluation of a series expansion of the particular interaction matrix element in closed form while neglecting completely other lower order but weaker interactions. It is this last point that taxes the ingenuity of the theoretician in reaching a good solution.

The Green's function method, as described by Callen[29] uses the Heisenberg Hamiltonian (Eq. (III.7)) to predict temperature dependence of the magnetization over the entire temperature range, giving a $T^{3/2}$ result at low temperatures in agreement with spin-wave theory and experiment and at high temperatures gives a susceptibility $\chi \propto 1/T + T_c/T^2$ in agreement with the result derived by a rigorous expansion of the susceptibility in powers of $1/T$.[30] In the region below T_c the one adjustable parameter permits good fits to the magnetization data.

This is in contrast to the Stoner model which gives a T^2 temperature dependence at low temperatures and not enough curvature for $T > T_c$. The Stoner model also has the severe disadvantage of being difficult to interpret analytically, it generally being necessary to give predictions in tabulated numerical form.

C. Temperature Dependence of the Hyperfine Field at Impurities in Ferromagnets

1. Non-local Moments

In view of what has been discussed in the earlier parts of this section we clearly might assume that the hyperfine field at the impurity atom is proportional to the lattice magnetization. This is almost certainly true for the host lattice itself and has been demonstrated experimentally by Nagle[31] et al., Benedek and Armstrong,[32] and Preston, Hanna, and Heberle[33] for pure Fe and by Streever and Bennett[34] for pure Ni. This assumption has also been demonstrated to be true for some impurities e.g., CoNi,[35] FeNi.[36]

For the case of ^{111}CdNi described in Sec. V, the hyperfine field at the ^{111}Cd nucleus is clearly seen to be proportional to the lattice magnetization over the entire temperature range that we studied. To describe this case, we make use of a model developed by Lovesey and Marshall[37] based on the molecular field model. This model will be used in Sec. V.C.

2. Local Moments

For cases in which the impurity hyperfine field is not proportional to the lattice magnetization, it is not clear how to proceed. This is the case for ^{99}RuNi, which will be described in Sec. VI and is possibly the case for ^{100}RhNi, to be described in Sec. VII.

The first question to be answered is to determine why these impurities are different from Cd. After this question is analyzed we can then attempt to incorporate our conclusions into a model for the system.

a. Local Moments--Why? So far as magnetic properties are concerned, the most obvious difference between Ru and Rh on one hand, and Cd on the other is that the former two have incomplete 4d electron shells. Since unpaired d-electrons are responsible for ferromagnetism, there is good cause to expect Ru and Rh to behave differently from Cd.

If we now consider the impurity magnetic hyperfine field to be described by Eq. (III.4) we see that whereas Ru and Rh are expected to have contributions to H_{hf} from both CEP and CP, Cd will only have contributions from the former. As is pointed out by Shirley, Rosenblum, and Matthias[21] the CEP can be very well described by

$$H_{hf} = .027\mu H_{ns}$$

where μ is the host magnetic moment and H_{ns} is the magnetic hyperfine field arising from an unpaired atomic ns-electron.

In Fig. III.1 is shown a plot of the existing data on the magnetic hyperfine fields for 4d and 5d impurities in an iron host. The solid

curve is calculated by Eq. (III.10). It is clear that the fit is quite good for the first half of the d-shell, but the fields deviate quite markedly at Ru and Os before returning to the CEP baseline at Ag and Au. This is strong evidence for the existence of unpaired d-electrons on the impurity atom. In fact, by assuming that this deviation is solely due to CP, and making use of derived values of $H_{4d} = -370$ kG[38] and $H_{5d} = -1180$ kG,[39] the fields due to a single unpaired 4d and 5d electron respectively, we can calculate an impurity magnetic moment. These calculated moments are compared to those determined by magnetic scattering of neutrons from the work of Collins and Low[40] and Campbell[41] in Fig. III.2. The agreement is quite good considering the approximations in our model and the fact that the two methods measure somewhat different quantities, viz, the spin density at the solute nucleus versus a magnetic disturbance near the solute atom.

It can clearly be inferred from these data that the first half of each transition series have small or zero localized d-electron unpairing in iron. The unpaired d-electrons are mostly itinerant in the early members while for the latter half of the transition series they are more localized on the impurity atom (or equivalently, more weakly coupled to the lattice). It is these latter impurities which we call local moments.

b. Local Moments--Temperature Dependence of the Hyperfine Field below T_c. A third method for studying local moments is through the temperature dependence of the hyperfine field, a technique which was suggested and used by Jaccarino, Walker, and Wertheim (JWW).[7] These workers explained the

temperature dependence of H_{hf} on ^{55}Mn in iron in terms of a molecular field model involving a localized moment on the Mn atom. In further work on this idea, Callen, Hone, and Heeger[42] and later Hone, Callen and Walker[43] outlined the conditions under which the molecular field theory could be expected to rigorously describe the impurity moment. Following this, Low,[44] and Shirley, Rosenblum, and Matthias[21] pointed out that the JWW model neglected the CEP contribution to the hyperfine field and were able to fit the ^{55}MnFe data with a different set of parameters. We will first describe the work of Callen, Hone, and Heeger which justifies the use of the molecular field model, then the JWW model, and finally the JWW model modified to take account of CEP.

In the treatment of Callen, Hone and Heeger, and Hone, Callen and Walker, the Green's function theory of ferromagnetism is used to predict the thermal average impurity magnetic moment. They first define the quantity $A_g(T,E)$ which gives the spectral distribution of spin excitations in terms of the imaginary part of the retarded Green's function $G_{gg}(E)$. The Green's function formalism in the random phase approximation is then used to calculate the mean occupation number of the excitation spectrum which is then set equal to the distribution function of a fictitious boson of a "quasi-boson energy," $\Omega(g)$ which in turn leads to

$$\langle S_I^z \rangle = S_I B_{S_I} [\Omega(g)/kT] \qquad \text{(III.10)}$$

where $B_s(y)$ is a Brillouin function.

If $\Omega(g)$ were to be proportional to the host magnetization this would lead to the molecular field theory. The two necessary conditions for this to occur are demonstrated to be:

1) that the impurity either be more strongly or more weakly coupled to the host lattice than a host atom.
2) the spin flip excitation spectrum $A_g(T,E)$ of the impurity spin should consist of a single sharply defined energy, proportional to the host magnetization.

Jaccarino, et al.,[7] obtained very good fits for NMR data on ^{55}Mn in iron[6] using a model in which a localized moment on the manganese atom is oriented in the exchange field, $H_{ex} = \zeta(\sigma_T/\sigma_o)(kT_c/gB)$. Here H_{ex} is scaled to the reduced lattice magnetization (σ_T/σ_o) by a constant ζ that takes account of the host-solute exchange energy being smaller than the host-host exchange energy. The hyperfine field is then proportional to $B_j(y)$, the Brillouin function of spin j, with $y = gBH_{ex}/kT$. These workers found a good fit (<0.5%) for $H_{hf}(T)$, using $j = 3/2$, and rather poorer fits for other values of j.

This model took no account of contributions to H_{hf} from conduction electrons. Such contributions are clearly present in many other cases and are expected to be present, to some extent, in all ferromagnetic metals. A conduction-electron term in H_{hf} is expected to follow the lattice magnetization rather closely. Along with Shirley et al.[21] and Low[44] we shall assume that contributions from conduction electrons and from localized moments, $H_c(T)$ and $H_L(T)$ are additive, and that $H_c(T)$ is proportional to the lattice magnetization and we have,

$$H_{hf}(T) = H_c(0)\frac{\sigma_T}{\sigma_0} + H_L(o)B_j(y) \qquad \text{(III.11)}$$

If we compare this to Eq. (III.4) we see that the forms are identical if we identify $H_c(0) = p_o H_{ns}$ and $\langle S_z \rangle_T = \langle S_z \rangle_o B_j(y)$ with $H_L(0) = 2\langle S_z \rangle_o H_d$. Shirley et al.[21] also showed that using Eq. (III.11) they got equally good fits for all values of $\frac{1}{2} \leq j \leq \frac{5}{2}$ for ^{55}MnFe.

The model is conveniently summarized by defining the reduced lattice magnetization $\sigma_R = \sigma_T/\sigma_o$, and by denoting by $f = H_L(0)/H_{hf}(0)$ the fraction of $H_{hf}(0)$ that has local origin. The reduced hyperfine field at the solute nucleus is then

$$\frac{H_{hf}(T)}{H_{hf}(0)} = fB_j(y) + (1-f)\sigma_R \qquad \text{(III.12)}$$

This is a relation which, for any j, we may try to fit $H_{hf}(T)$ using two adjustable parameters, j and f. We shall use this model in Sec. VI to fit our ^{99}RuNi data.

3. High Temperature Behavior of Impurity Hyperfine Fields

For a given j, the independent variables in Eq. (III.12) are the absolute temperature, T, and the lattice magnetization, σ_T. In a given host lattice, these variables are related, below T_c, by the magnetization curve, and there is no way to study the dependence of $H_{hf}(T)/H_{hf}(0)$ on σ or T alone. In a case such as FeMn, for which excellent fits are obtained

for several values of j, but with quite different values of f(j), it is desirable to determine f (and thus j) by varying σ and T separately. This is possible within the framework of the model because H_c depends on σ alone, while H_L depends, through B_j, on σ/T.

For $T > T_c$, σ and T can be varied separately. For a given applied field, H_o, the effective field is given by

$$H_{eff} = H_o(1+K) = H_o + H_c(0)\frac{\sigma_{T,H}}{\sigma_0} + H_L(0)B_j(y) \qquad \text{(III.13)}$$

if Eq. (III.11) is still applicable. Here K is a paramagnetic Knight shift. If one then adjusts H_o to keep $\sigma_{T,H}/\sigma_0$ constant, one obtains the dependence of K(T) on T alone. This shift is negative, and for $T \gtrsim T_c$ can be as large as 100%. For $T >> T_c$ it approaches zero asymptotically. The behavior of this curve should be insensitive to the value of j if one uses the values of f and ζ found below T_c. Of course, this treatment is based on the assumption that local moments exist above T_c if they exist below T_c, and that Eq. (III.12) is still applicable.

For the case of ^{99}RuNi, it appears as if there is a local moment above T_c, since the hyperfine field is not proportional to the induced magnetization. However, as pointed out in Sec. VI.D we have reason to suspect the reliability of these results.

For both the case of ^{100}RhNi and ^{111}CdNi, described in Sec. VII and V respectively, the hyperfine magnetic field is found to be proportional to the lattice magnetization indicating that there is no local moment above T_c in either case.

For the case of ^{100}RhNi, in addition to the static hyperfine interaction we also find a time-dependent interaction which manifests itself as an exponential attenuation of the TDPAC spectrum. The temperature and magnetic field dependence of this relaxation rate lead us to believe that it arises from exchange narrowing.[45,46]

The origin of this behavior can be understood on the basis of a simple model. Let us consider a system of atoms within which a ferromagnetic exchange interaction exists, and an impurity whose hyperfine field is produced by indirect hyperfine interactions with neighboring magnetic atoms. This should clearly be true for ^{111}CdNi and ^{100}RhNi above T_c. Fluctuations of the electronic spins on the nickel atoms causes spin-lattice relaxation and time-dependent attenuation of the anisotropy. At very high temperature, the spins are uncorrelated and make random contributions to the fluctuating hyperfine field at the nucleus. With decreasing temperature the paramagnetic nickel spins develop parallel correlations. In the high temperature limit (Zeeman energy << kT), the hyperfine fields remain random, but increase in magnitude as the temperature is lowered and exchange correlations become increasingly more effective.

In recent work in cubic Laves phase XAl_2 compounds (X = rare earth) Silbernagel et al.[47] have proposed a model based on this idea to account for the temperature dependence of the relaxation rate of the aluminum nuclei in the paramagnetic region using a Hamiltonian analogous to our Eq. (III.2b). They calculate the second moment of the NMR lineshape taking account only of correlation between pairs of paramagnetic atoms. Since their work was carried out at $T >> T_c$, this is expected to be a reasonable

approximation, and indeed proves to predict the correct trend of the relaxation rate. However, our data on ^{100}RhNi had all been taken in the range $T_c < T \leq 1.2T_c$ and we expect that we need consider higher order correlations than pairs.

In order to arrive at a tractable model we make use of the Hamiltonian of Eq. (III.2b) to create a hyperfine field at the impurity nucleus. To evaluate H_{ex}, the exchange field, we make use of the molecular field approximation

$$\vec{H}_{ex} = \frac{J_e}{g\beta} \sum_j \langle \vec{S}_j \rangle \qquad \text{(III.14a)}$$

where J_e = isotropic exchange constant, and $\langle \vec{S}_j \rangle$ = average spin contribution at a host atom i due to all other host atoms j.

If we now allow for an externally applied field, H_o, we get a Zeeman term,

$$\mathcal{H}_z = g\beta \vec{H}_o \cdot \sum_i \vec{S}_i \qquad \text{(III.14b)}$$

We neglect the direct effect of the applied field on the nucleus.

If we further assume the H_o and H_{ex} are colinear, and along the z-axis we obtain the total Hamiltonian,

$$\mathcal{H} = g\beta(H_o + H_e) \sum_i S_{iz} - \gamma_I \vec{I} \cdot \vec{H}_{hf} \qquad \text{(III.14c)}$$

As a final assumption, we set

$$H_{hf} = \frac{A}{\gamma_I} \sum_{\substack{i \\ \text{Ni atoms}}} S_{iz} \qquad \text{(III.15a)}$$

i.e., indirect hyperfine interaction and thus

$$\mathcal{H} = g\beta H_{eff} \sum_{\substack{i \\ \text{Ni atoms}}} S_{iz} - AI_z \sum_{\substack{i \\ \text{Ni atoms}}} S_{iz} \qquad \text{(III.15b)}$$

Using the equation of motion method we find that the Fourier transform of the second moment of the NMR lineshape is

$$\langle \omega^2 \rangle = \frac{A^2}{\hbar^2} \frac{T_r\left\{ e^{-\beta_o \mathcal{H}} \left(\sum_i S_{iz} \right)^2 I_x^2(0) \right\}}{T_r\left\{ e^{-\beta_o \mathcal{H}} I_x^2(0) \right\}} \qquad \text{(III.16)}$$

$$[\beta_o = 1/kT]$$

If we assume now that $A \ll J_e$ we find

$$\langle \omega^2 \rangle = \frac{A^2}{\hbar^2} \left[\sum_{\substack{i<j \\ \text{Ni atoms}}} \langle S_{iz} S_{jz} \rangle + \sum_{\substack{i \\ \text{Ni atoms}}} \langle S_{iz} \rangle^2 \right] \qquad \text{(III.17)}$$

where

$$\langle S_{iz} S_{jz} \rangle = \frac{T_{r_{el}} \left\{ e^{-\beta_o g\beta H_{eff} \sum_k S_{kz}} S_{iz} S_{jz} \right\}}{T_{r_{el}} \left\{ e^{-\beta_o g\beta H_{eff} \sum_k S_{kz}} \right\}} \qquad \text{(III.18)}$$

the trace being taken only over electronic variables. This leads to the well known results

$$\langle S_{iz} S_{jz} \rangle = \left\{ S B_s(\beta_o g\beta H_{eff} S) \right\}^2$$

and

$$\langle S_{iz}^2 \rangle = \left\{ S B_s(\beta_o g\beta H_{eff} S) \right\}^2 + S^2 \frac{dB_s(\beta_o g\beta H_{eff} S)}{d(\beta_o g\beta H_{eff} S)} \qquad \text{(III.19)}$$

where S = electronic spin and $B_s(y)$ is the Brillouin function. If we now assume the high temperature limit, i.e., $\beta_o g\beta H_{eff} \ll 1$, $dB_s(y)/dy$ is independent of y. Thus

$$\langle \omega^2 \rangle = (A/\hbar)^2 \, 3 \left\{ S B_s(\beta_o g\beta H_{eff} S) \right\}^2 + \text{constant} \qquad \text{(III.20)}$$

Making use of the result from molecular field theory that the induced magnetization σ, for N atoms, is

$$\sigma = N g \beta S B_s(y) \qquad \text{(III.21)}$$

we find

$$\langle \omega^2 \rangle = 3(A/\hbar)^2 \, (\sigma/Ng\beta)^2 + \text{constant} \qquad \text{(III.22)}$$

Following Kubo,[48] we write the relaxation rate, in the exchange narrowed limit,

$$\frac{1}{T_1} \approx \frac{1}{T_2} = \frac{\pi}{2\sqrt{3}} \langle \omega^2 \rangle \left[\frac{\langle \omega^2 \rangle}{\langle \omega^4 \rangle} \right]^{1/2} = \frac{\pi}{2\sqrt{3}} \langle \omega^2 \rangle \, \tau_c \qquad \text{(III.23a)}$$

where τ_c = the spin-spin correlation time.

This, in turn, gives

$$\frac{1}{T_1} \approx \frac{1}{T_2} = \frac{\pi}{2\sqrt{3}} (A/\hbar)^2 \, \tau_c \left(\frac{\sigma}{Ng\beta} \right)^2 + \text{constant} \qquad \text{(III.23b)}$$

This simple model is able to describe the relaxation behavior of the Rh nucleus in Ni above the Curie temperature surprisingly well and will be discussed further in Sec. VII.

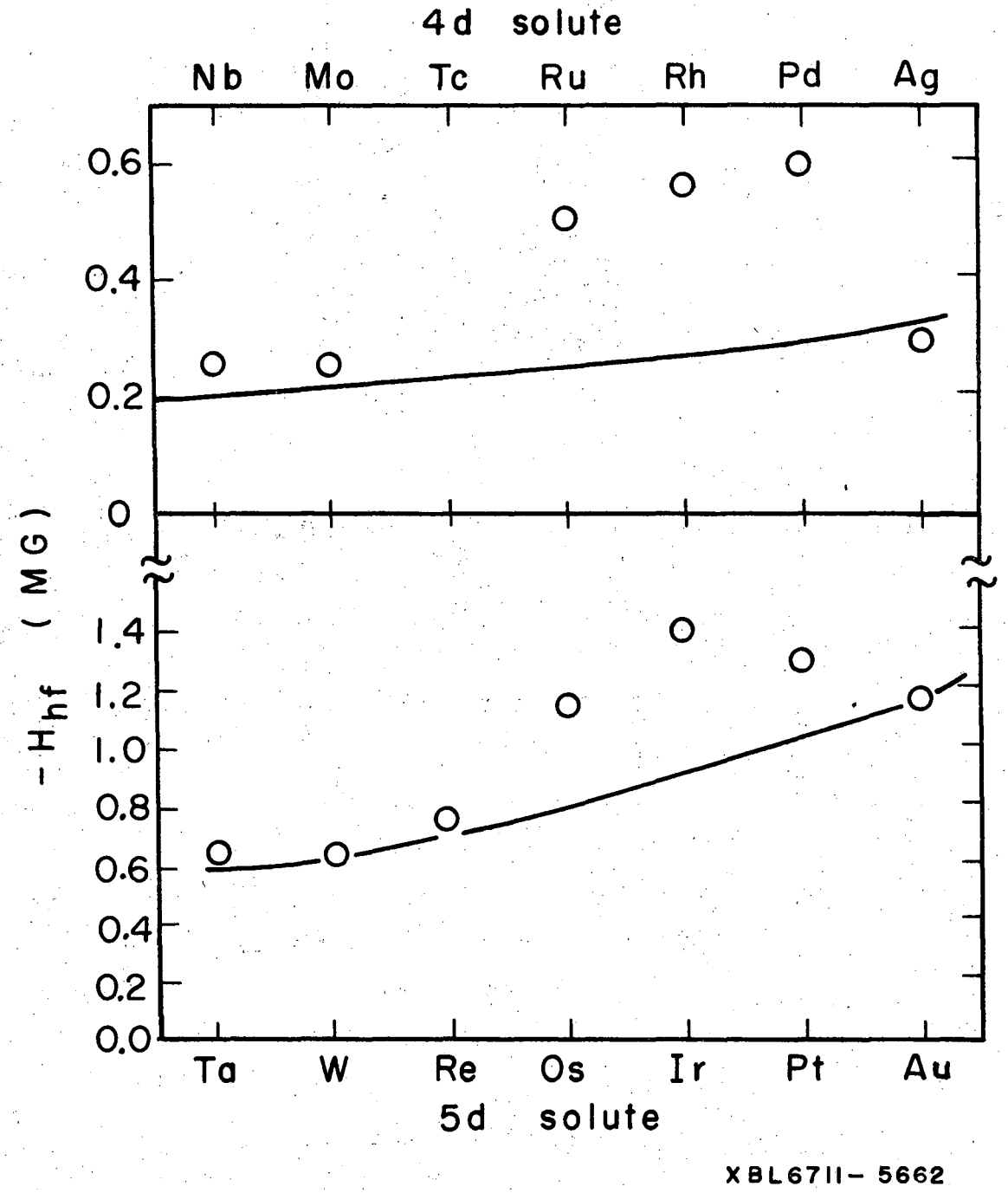
4d solute
Nb
Mo
Tc
Ru
Rh
Pd
Ag
0.6
0.4
0.2
0
$-H_{hf}$ (MG)
1.4
1.2
1.0
0.8
0.6
0.4
0.2
0.0
Ta
W
Re
Os
Ir
Pt
Au
5d solute
XBL6711-5662

Figure III.1

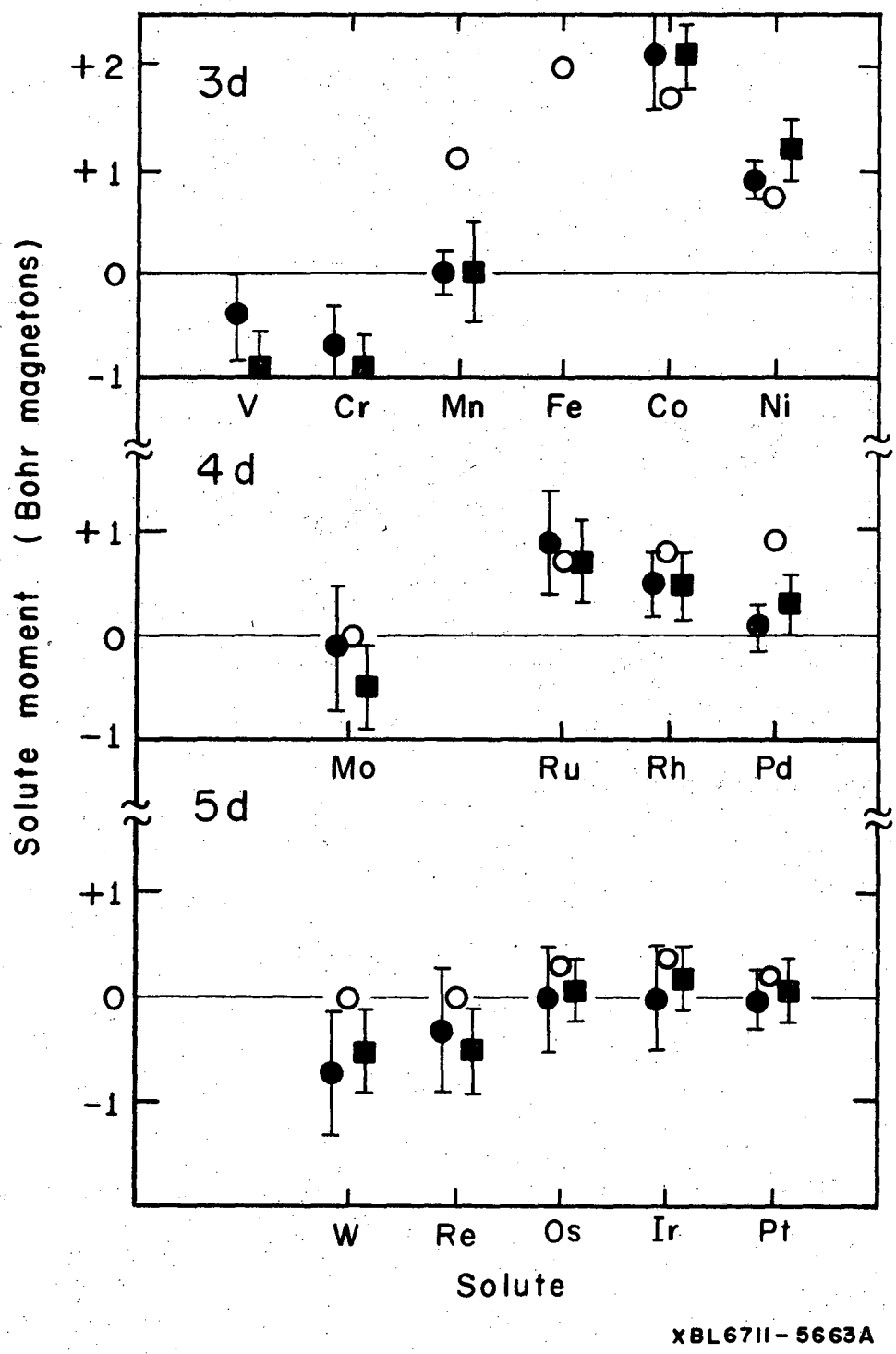
3d
4d
5d
+2
+1
0
-1
V
Cr
Mn
Fe
Co
Ni
Mo
Ru
Rh
Pd
W
Re
Os
Ir
Pt
Solute moment (Bohr magnetons)
Solute
XBL6711-5663A

Figure III.2

IV. APPARATUS

A. The Perturbed Angular Correlation Spectrometer

In spite of the misleading implication in the above title, no single configuration can be described as the spectrometer. During the course of the work described here many modifications and improvements were made to the apparatus so that the specific description given in this section will be only representative of basic configurations.

Except for the data on ^{99}RuNi above T_c, all experiments described here were carried out by time-differential PAC; for ^{99}RuNi above T_c, $\omega_L\tau$ was too small to permit this so that the less accurate time integral PAC method was used.

1. Time-Differential Apparatus

There are two basic configurations included under this heading. One is that used in the earlier experiments on ^{99}Ru and ^{111}Cd where sodium iodide scintillators were used, and the other is that used for ^{100}Rh employing lithium-drifted germanium detectors. Both are basically of the "fast-slow" type as described in the basic references.[8,9,10]

2. Spectrometer Using NaI(Tl) Scintillators

In Fig. IV.1 is shown a block diagram of the system. The "x" numbers in the blocks are the Electronics Engineering drawing numbers for LRL designed equipment.

The scintillators used were usually 1-1/2"×1-1/2" crystals mounted directly onto the photomultiplier tube. For the work carried out in the

large electromagnet (^{111}CdNi above T_c and all work on ^{99}RuNi), the scintillators were mounted onto 12" long optical quality quartz light pipes which were, in turn, cemented to the photomultiplier tubes. These light pipes did not significantly degrade the system characteristics.

The photomultipliers used with the light-pipes were Amperex 56AVP tubes. Those used without light-pipes were Amperex XP1020 tube. In all cases the tubes were surrounded by concentric magnetic shields of mu-metal and soft iron.

The rest of the block diagram is fairly straightforward. The "slow" circuit allows energy selection to be carried out. The output coincidence pulses are used to open the gate of the Packard multi-channel analyzer.

The "fast" circuit retains the timing information of the detector pulses and feeds the linear input of the multi-channel analyzer.

The time resolution for this system was typically 2.0 nsec for 511 keV annihilation radiation from ^{22}Na.

3. Spectrometer Using Ge(Li) Detectors

In Fig. IV.2 is shown a block diagram of this arrangement. Here, again the "x" numbers indicate the Electronics Engineering drawing numbers of LRL-designed-and-built equipment.

The detectors used here were designed to provide good time resolution at low γ-ray energy. Both detectors were rectangles of 2.6×2.0 cm and 0.5 cm thick. The bias applied to them was in the region of 300-400 volts. The preamplifiers used a cooled field-effect transistor as an input stage.

The "slow" circuit consisted of a linear amplifier system designed by F. Goulding and D. Landis. This system contains a linear amplifier and shaper, a single channel analyzer, a linear gate, and a fast coincidence unit. In these experiments, only the first three units were used. The single channel outputs were fed into delay and gate generators in order to stretch and amplify them. They were then fed into a slow coincidence network which gave a resolving time $2\tau_o$ = 3 μsec. The output of this unit provided the pulses which opened the linear gate for the time pulses.

The "fast" circuit consisted of 2 wideband amplifiers of gain ×10 in series, followed by a tunnel-diode discriminator, which, in turn, fed the time to amplitude converter (TAC). After amplification, the TAC output was fed into a delay network consisting of 50 ohm cable in order to restore the time relation between the "fast" and "slow" signals. This insured that the linear ("fast") signals were properly gated by the gate ("slow") signals. The linear output was then fed into a multi-channel analyzer.

The time resolution of this system for the prompt 128-105 keV cascade in ^{177}Hf was 10.0 nsec.

4. Time-Integral Apparatus

As was mentioned in the beginning of Sec. IV, only for the case of ^{99}RuNi above T_c was the time-integral technique used. In Fig. IV.3 is shown a block diagram of the electronics. It is similar to that shown in Fig. IV.1, but it is much simpler since the requirements on the time

resolution were much less stringent (≈10 half-lives of the 20.7 nsec state in ^{99}Ru).

The "slow" output of both detectors was fed into a linear amplifier and shaping network to give a double-delay-line differentiated linear output. The amplifier output was then split. For both γ_1 and γ_2 one part of the output was fed into a lower level discriminator set just below the peak of interest. The discriminator output was fed into a fast coincidence unit set to a resolving time $2\tau_o$ = 200 nsec and thence into a variable delay to allow the alignment of the two parts of the signal. The fast signal was then fed into one side of the slow coincidence unit with $2\tau_o$ = 2 μsec.

The other part of the γ_1 signal was fed into a single channel analyzer to select the transition energy. The single channel analyzer output fed the other arm of the slow coincidence unit.

The coincidence output was used to open the delayed gate of a multi-channel analyzer. The linear input of the multi-channel analyzer was the other part of the γ_2 output. Thus, one obtains an energy spectrum which is coincident with the γ_1 peak, within a resolving time of 200 nsec. All experiments are normalized with the γ_1 counting rate as measured by the scaler.

5. Time Calibration

In the early experiments on ^{99}Ru and ^{111}Cd time calibrations were carried out using calibrated lengths of RG 63 B/U cable to delay the prompt coincidence peak of a ^{22}Na source. The centroids of the peaks were

located and plotted vs. cable delay to give the calibration in time/channel.

This method suffered from several difficulties:

1) It took approximately 2 hours to do a calibration since one had to count coincidences at each delay.

2) It was difficult to find the centroid of the peak accurately.

3) The longer cables (or equivalently longer delays) tended to attenuate the pulse height because of resistive losses, leading to increasing errors at long delays.

All these difficulties led to time calibrations of 1% accuracy.

To improve on this accuracy a quartz crystal oscillator controlled delay generator was used in later experiments. This device, the Eldorado Electronics Digital Delay Generator, Model 610,* generates a "start" and a "stop" pulse separated by a thumb-wheel selected delay. It permits time calibrations of an accuracy of 1 part in 10^4 and a reproducibility of 0.1%.

B. Magnets

Three different arrangements were used to produce magnetic fields;

1) a large H-frame iron core electromagnet, which was capable of producing a maximum field of 20 kOe over a 2.5 inch gap with a diameter of 4 inches. The magnet was fed by a current-regulated motor-generator set. The field stability was ±1% for all runs in this magnet.

*Eldorado Electronics, 601 Chaldnar Road, Concord, California.

2) a smaller, C-frame iron core electromagnet which was capable of producing a maximum field of 3 kOe over a 2 inch gap with a diameter of 2 inches. The magnet was fed by Perkin Regulated D.C. Power Supply, Model MTR 636-30. The stability of the field was 0.1% over a typical run of 2 days. All experiments on ^{100}RhNi were carried out in this magnet.

3) a set of small, iron, permanent magnets producing fields up to 5 kOe over a 1.5 cm gap with a 2 cm diameter. These magnets, of course, had very good long term stability, but the inhomogeneity of the field in the gap led to an uncertainty of ±10 Oe in the value of the field.

The fields of the magnets were measured by either a Hall probe (Bell Model 240) or a rotating coil gaussmeter [George Associates Model 203A]. The readings of these instruments were then compared to those of an NMR probe in a high homogeneity electromagnet in order to obtain the accurate absolute values of the fields. Thus, errors in fields are due principally to inhomogeneities and drift.

C. Temperature Control

1. Below Room Temperature

Data were taken at three temperatures in this region: 4.2°K (boiling point of liquid helium), 77°K (boiling point of liquid nitrogen) and 194.5°K (dry ice-acetone bath). The last two measurements were carried out in a glass dewar with a 2 cm O.D. thin-wall glass tip. For the measurements at 4.2°K, a second glass dewar with an 8 mm O.D. tip was inserted inside the first. Liquid helium was transferred into the inner dewar while liquid nitrogen was in the outer dewar.

2. Above Room Temperature

a. Early furnace. In Fig. IV.4 is shown a schematic diagram of the simple arrangement used in the measurements on ^{99}RuNi and most of the data on ^{111}CdNi. The furnace consisted of an alumina tube with heating tape wrapped around it, followed by a covering of aluminum foil and then asbestos tape for insulation. The thermocouple was a calibrated Pt vs. Pt-10% Rh junction, which was held in place by a piece of Pyrex glass tubing. These connections were made by using a high temperature adhesive.* This cement was also used to mount the sample on the thermocouple.

The thermocouple output was measured by using a Leeds and Northrup K-2 Potentiometer. The furnace temperature was controlled by adjusting the voltage applied to the heating tape with a variable transformer. It was found that by using regulated AC line voltage as a power source, the temperature variation of the furnace was less than ±2°C over the entire range of temperatures reported for periods up to two days.

b. Gamma furnace. When this series of experiments was first conceived it was clear that a better apparatus than that described above should be designed and built to carry out PAC experiments at elevated temperatures. The main criteria established for this apparatus were:

1) it should have only low atomic-number materials (e.g.,Be, BeO) between the source and the detectors

*Sauereisen Adhesive Cement no. 1, Sauereisen Cement Co., Pittsburgh, Pa.

2) it should be capable of attaining 1500°C

3) its temperature stability and accuracy should both be better than 1°C over a period of 2 days

4) it should fit between the pole tips of the 20 kOe electromagnet described previously. The resulting apparatus is shown in the schematic drawing of Fig. IV.5 and the photographs (Figs. IV.6 and IV.7).

Figure IV.5 shows the hot zone of the furnace. The rest of the system just consists of a stainless steel pipe and an 8 liter/sec Varian Vac-Ion Pump which acts as a holding pump for the system.

The radioactive samples, generally .002" thick disc-shaped Ni foils, were spotwelded to the platinum sample mount. This mount is a tight press-fit on the platinum thermocouple head. The mating surfaces were polished to a high finish in order to maximize the contact area. The thermocouple, consisting of .010" O.D. chromel and alumel wires, was pressure fitted into the head. Around the sample holder is a close-fitting beryllium-oxide heat shield around which the heater wire was wound. The heater wire was .007 in. O.D. tungsten.

Surrounding the entire heater assembly was a second beryllium oxide heat shield which was, in turn, surrounded by as many as 3 beryllium heat shields. All heat shields have a wall thickness of approximately .010". They were produced by a combination of mechanical and chemical machining.

The vacuum wall surrounding this consists of a water-cooled aluminum housing with .010" thick beryllium windows welded into it by means of an electron-beam welder. The assembled furnace and two window assemblies are shown in Fig. IV.6.

A typical experimental arrangement used in the measurements of ^{100}RhNi is shown in Fig. IV.7. Here the two furnace windows are at 135° to each other. The furnace is inside the pole tips of a small electromagnet (described in Sec. IV.D.2) and the two lithium-drifted germanium detectors (described in Sec. IV.A.3) in counting geometry inside their cryostats.

The furnace was temperature controlled by a conventional feedback system consisting of a Barber-Colman silicon control rectifier power unit [Model 621B] driven by a Barber-Colman Differential Galvanometer [Model 354A] whose output was steplessly proportional to the difference between the set point established by a Barber-Colman zener-stabilized Voltage Reference Source [Model 350] and the furnace working thermocouple.

The calibration of the thermocouple was determined by measuring the melting points of National Bureau of Standards samples of lead, tin, and aluminum in situ. The deviation between the measured value and the accepted value was less than 0.3°C for all three materials.

As a further check on the reliability and uniformity of the sample temperature some of the measurements made on ^{111}CdNi with the older furnace were repeated. The results were in excellent agreement.

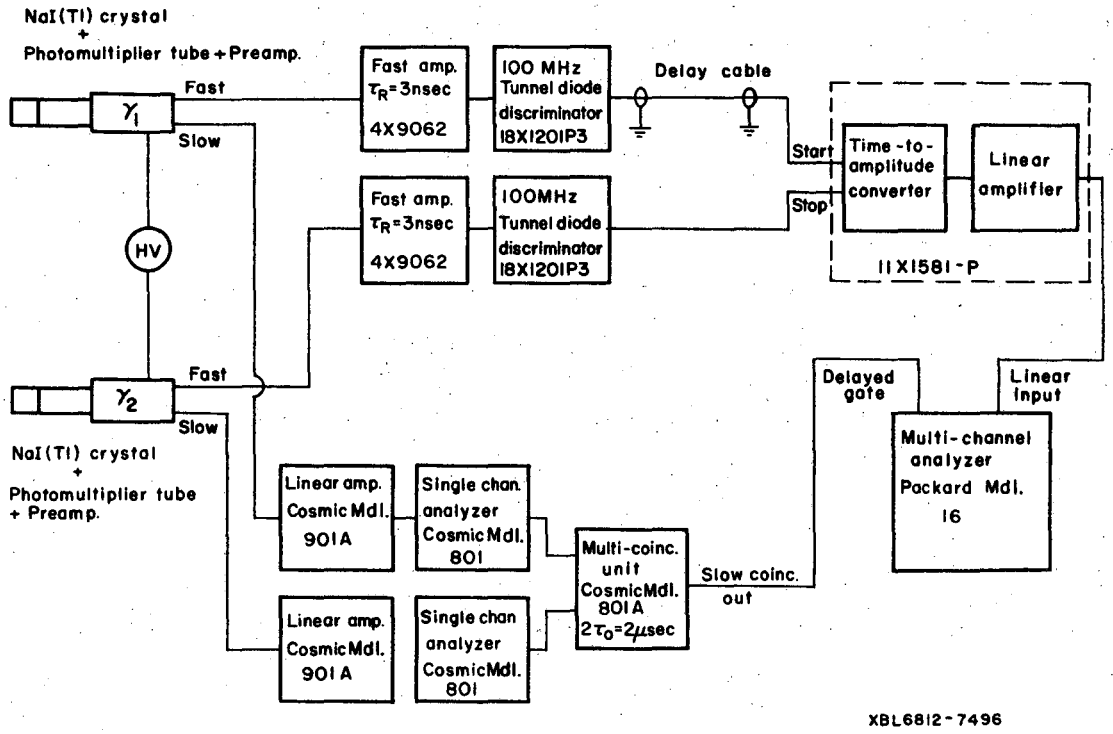
NaI(Tl) crystal
+
Photomultiplier tube + Preamp.
Fast
Slow
γ_1
HV
γ_2
Fast
Slow
NaI(Tl) crystal
+
Photomultiplier tube
+ Preamp.
Fast amp.
τ_R=3nsec
4X9062
100 MHz
Tunnel diode
discriminator
18X120IP3
Delay cable
Fast amp.
τ_R=3nsec
4X9062
100MHz
Tunnel diode
discriminator
18X120IP3
Start
Stop
Time-to-amplitude converter
Linear amplifier
11X1581-P
Delayed gate
Linear input
Multi-channel analyzer
Packard Mdl.
16
Linear amp.
Cosmic Mdl.
901A
Single chan. analyzer
Cosmic Mdl.
801
Multi-coinc. unit
Cosmic Mdl.
801A
$2\tau_o$=2μsec
Slow coinc. out
Linear amp.
Cosmic Mdl.
901A
Single chan analyzer
Cosmic Mdl.
801
XBL6812-7496

Figure IV.1

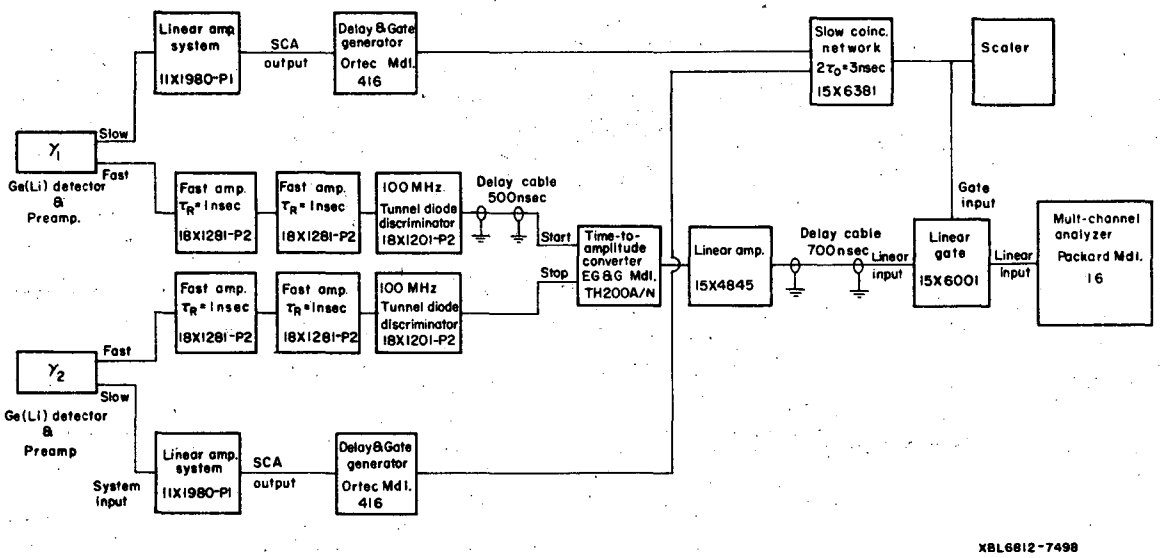
Linear amp. system 11X1980-P1
SCA output
Delay & Gate generator Ortec Mdl. 416
Slow coinc. network 2τ₀=3nsec 15X6381
Scaler
γ1
Slow
Fast
Ge(Li) detector & Preamp.
Fast amp. τR=1nsec 18X1281-P2
Fast amp. τR=1nsec 18X1281-P2
100 MHz. Tunnel diode discriminator 18X1201-P2
Delay cable 500nsec
Start
Stop
Time-to-amplitude converter EG&G Mdl. TH200A/N
Linear amp. 15X4845
Delay cable 700nsec
Linear input
Linear gate 15X6001
Gate input
Linear input
Mult-channel analyzer Packard Mdl. 16
γ2
Fast
Slow
Ge(Li) detector & Preamp
Fast amp. τR=1nsec 18X1281-P2
Fast amp. τR=1nsec 18X1281-P2
100 MHz Tunnel diode discriminator 18X1201-P2
Linear amp. system 11X1980-P1
SCA output
Delay & Gate generator Ortec Mdl. 416
System input
XBL6812-7498

Figure IV.2

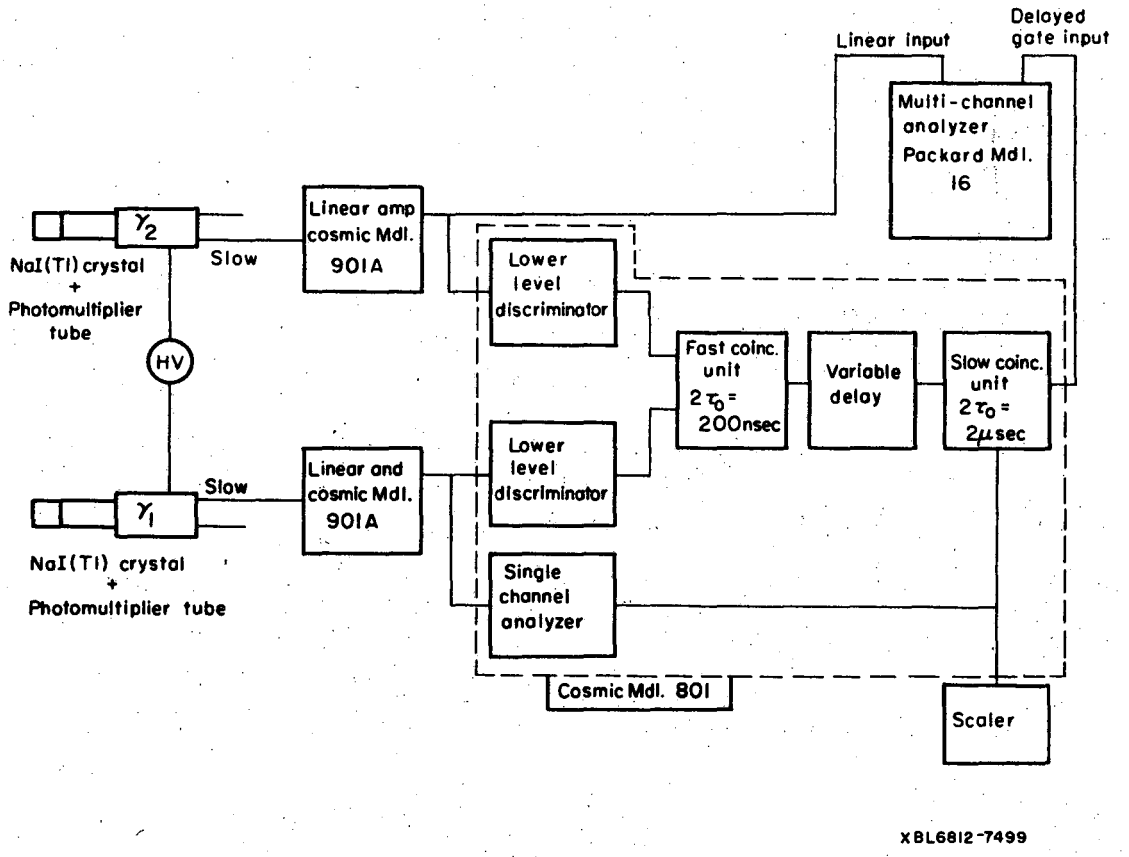
Linear input
Delayed gate input
Multi-channel analyzer Packard Mdl. 16
γ_2
NaI(Tl) crystal + Photomultiplier tube
Slow
Linear amp cosmic Mdl. 901A
HV
Lower level discriminator
Fast coinc. unit $2\tau_0$ = 200nsec
Variable delay
Slow coinc. unit $2\tau_0$ = 2μsec
Lower level discriminator
Linear and cosmic Mdl. 901A
Slow
γ_1
NaI(Tl) crystal + Photomultiplier tube
Single channel analyzer
Cosmic Mdl. 801
Scaler
XBL6812-7499

Figure IV.3

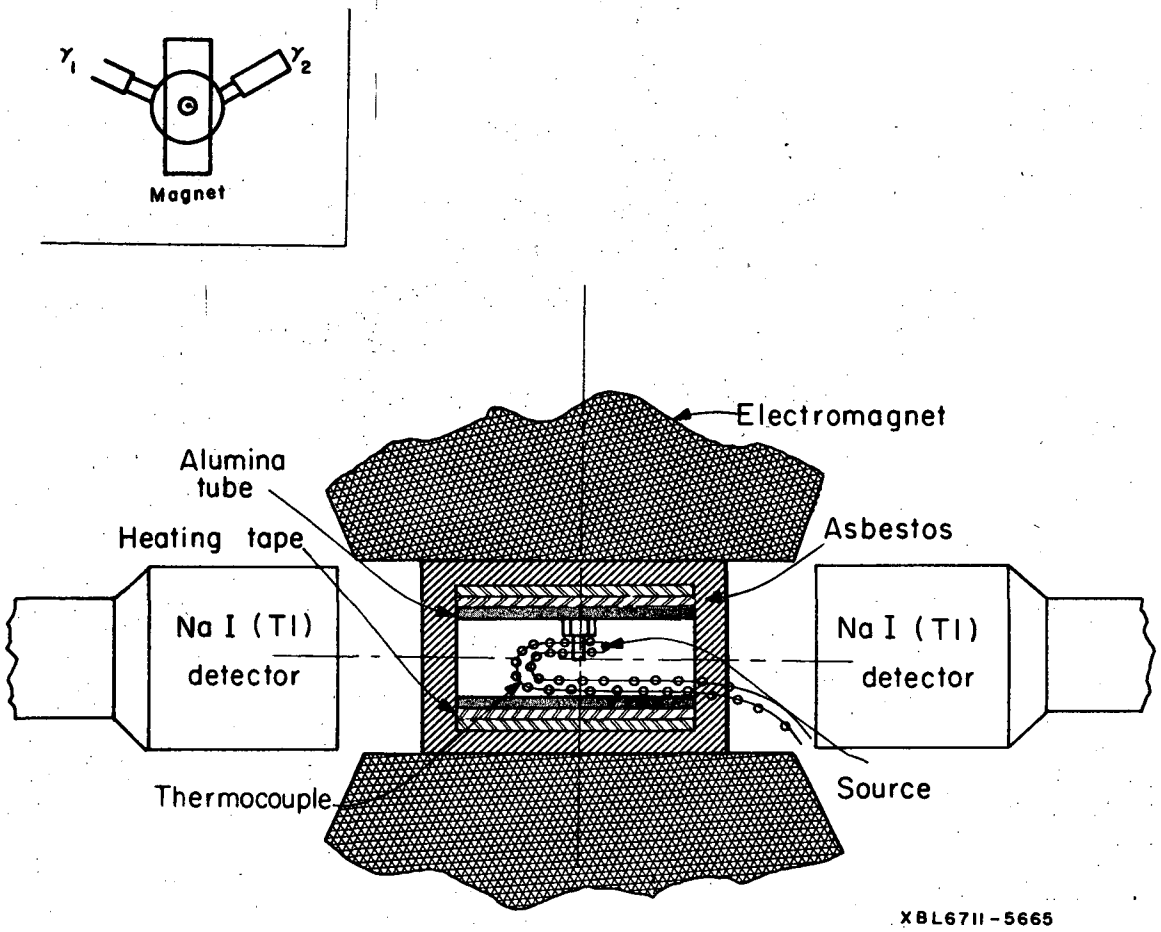
γ_1
γ_2
Magnet
Electromagnet
Alumina tube
Heating tape
Asbestos
Na I (Tl) detector
Na I (Tl) detector
Thermocouple
Source
XBL6711-5665

Figure IV.4

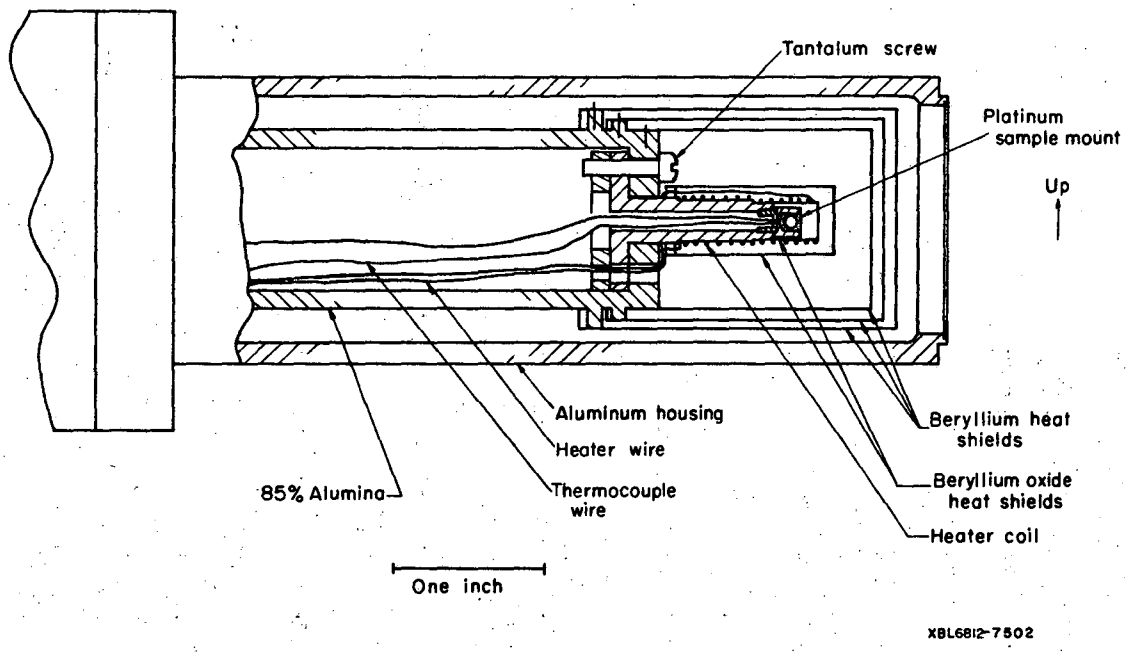
Tantalum screw
Platinum sample mount
Up
Aluminum housing
Heater wire
Thermocouple wire
85% Alumina
Beryllium heat shields
Beryllium oxide heat shields
Heater coil
One inch
XBL6812-7502

Figure IV.5

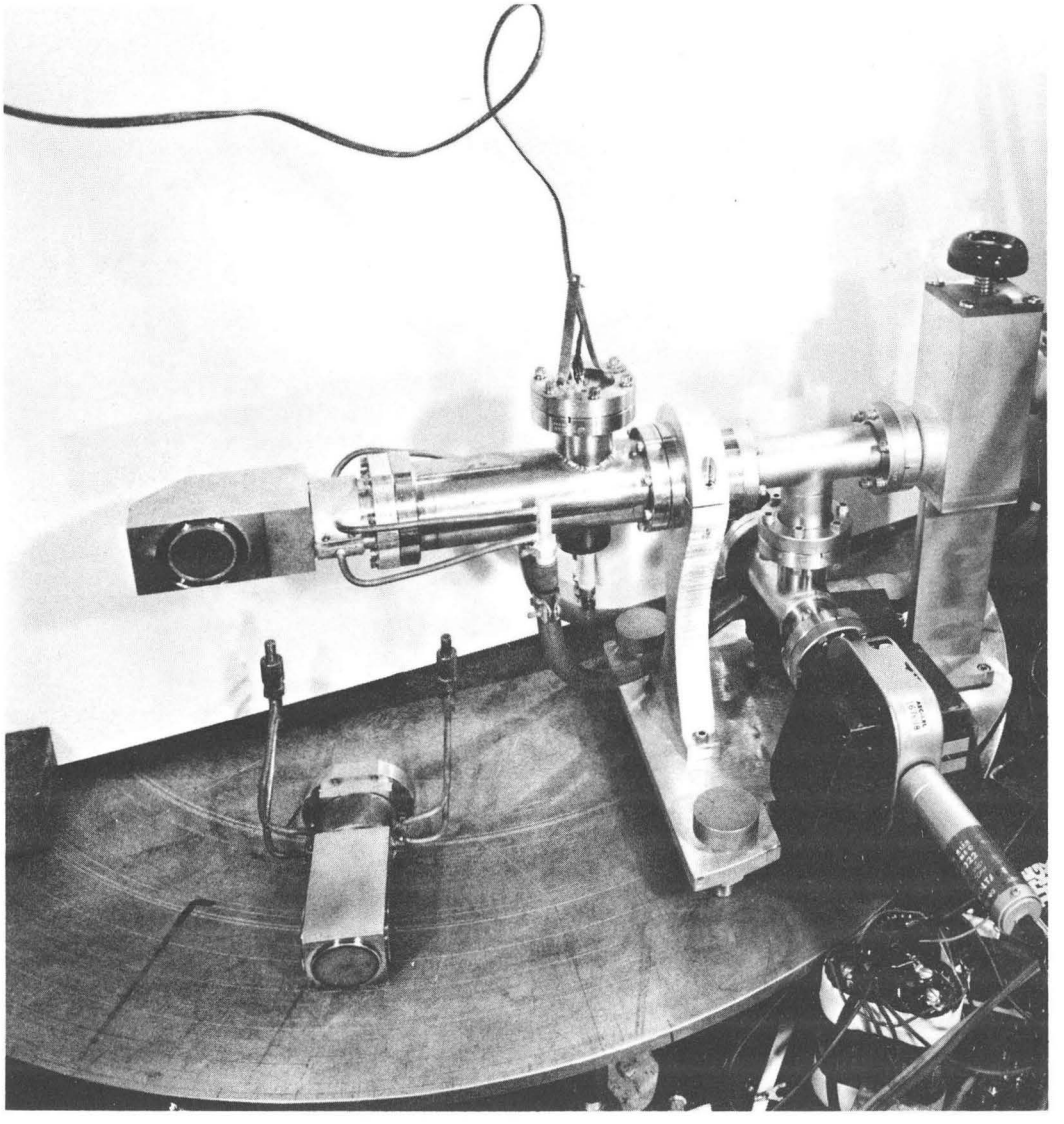

XBB 687-4577

Figure IV.6

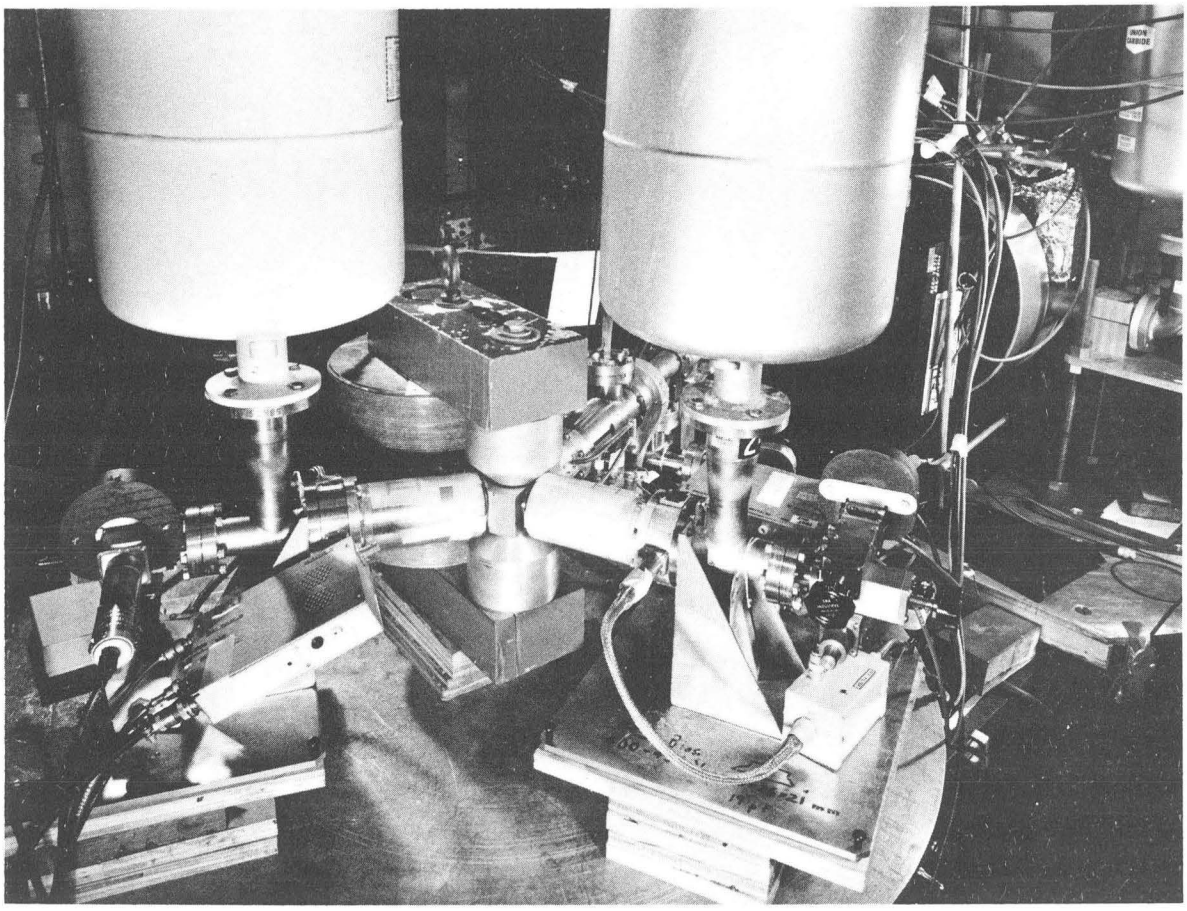

XBB 687-4576

Figure IV. 7

V. CADMIUM-III IN NICKEL

A. Source Preparation

The parent nuclide was prepared via the reaction $^{111}Cd(p,n)^{111}In$ using a 10 MeV proton beam at the Berkeley 88" cyclotron. Natural cadmium foil, 0.005" thick was the target material and the integrated flux was typically 25 μamp-hrs.

The chemical procedure used in the separation of the ^{111}In from the target material was essentially that of E. Jacobi[49] and is as follows:

1. Dissolve the target in a minimum amount of 1:1 HNO_3.
2. Make the solution basic with conc. NH_4OH.
3. Add ∿ 200 $Mg(NO_3)_2 \cdot 6H_2O$ dissolved in minimum volume H_2O.
4. Heat in water bath to digest the precipitate. The $Mg(OH)_2$ carries the $In(OH)_2$ quantitatively. Centrifuge and dissolve the ppt. in hot 2M H_2SO_4.
5. Repeat (2-4) and then dilute the solution with ∿ 4 ml H_2O.
6. Add ammonium formate to buffer the solution at pH 2.
7. Prepare a clean .0005" Ni foil cathode and platinum wire anode. Plate the In at a current density of ∿ 10 ma/cm^2.

These nickel foils were melted in an argon atmosphere at 1500°C for 15 minutes and then quenched to room temperature by removing them from the furnace quickly. The resulting spheroids, generally less than 0.5 mm in diameter, were used as sources.

B. Decay Scheme and Gamma Ray Spectrum

The level at 247 keV in ^{111}Cd provides an excellent case for the TDPAC technique. The significant protion of the decay scheme is given in Fig. V.1. More than 99% of the decays of the parent ^{111}In pass through the 247 keV level via the 173-247 keV cascade, making the true coincidence rate very large for a given source strength. The long half-life of the intermediate state allows the observation of many rotations of the nuclear spin, thus permitting very accurate determination of the rotation frequency. This level has been studied by many workers[50] and the g-factor is accurately known ($g = 0.318 \pm 0.007$).[51,52]

In Fig. V.2 is shown a typical gamma ray energy spectrum of a ^{111}CdNi source taken with our apparatus. The two photo peaks are seen to be well resolved with a very high peak to background ratio.

C. Results for $T < T_c$

Some typical raw data for ^{111}CdNi below T_c is shown in Fig. V.3. No external field was applied for this series of measurements so that Eq. (II.21) for a randomly oriented magnetic interaction was used. For the ^{111}Cd cascade $k_{max} = 2$ so that the actual function used in the least-squares-fitted curve was,[53]

$$F(t) = Ae^{-\lambda t} \{1 + C[1+2\cos(\omega t+\phi) + 2\cos 2(\omega t+\phi)]\} + B \qquad (V.1)$$

The data points were statistically weighted and then the least squares criterion was used to determine the best values of A,B,C,λ,ω, and ϕ. The uncertainty in ω due to statistical variations was generally less than 0.5% for these runs. Each run required about two days to complete.

All the data for ^{111}CdNi for $T < T_c$ is displayed in Fig. V.4 and summarized in Table V.1. The solid curve above the data points is the reduced spontaneous magnetization curve for pure Ni[54] while the dashed curve below the data points is that calculated on the model of Lovesey and Marshall[37] for magnetization of the nearest neighbors of a non-magnetic impurity, σ_1, for both impurity and host spins $S' = S = \frac{1}{2}$. This description makes use of the molecular field theory formalism, postulating a reduction of the local magnetization of the host atoms which are nearest neighbors to a non-magnetic impurity.

The experimental results were expected to lie between the two curves in Fig. V.4 because if the ^{111}Cd hyperfine field is created purely by short range exchange interaction then the data should follow σ_1/σ_0 while long range interactions would make $H(T)/H(0)$ approach σ/σ_0.

D. Results for $T > T_c$

Above T_c, it was no longer possible to work without a polarizing field, and a field of 19.5 kOe was applied. The results in this region are much less accurate than those below T_c since 1) there is an added uncertainty in the magnitude of the external field, and 2) H_{eff} is much smaller, preventing the observation of more than a few cycles of nuclear precession. In Fig. V.5 some typical data are shown. For these measurements, the two scintillation detectors were placed at a fixed position,

135° apart, and counts were taken for magnetic field up and down relative to the detector plane.

The data above T_c are displayed in Fig. V.6. The ordinate is $\beta = H_{eff}/H_{ext} = 1 + K$, where K is the paramagnetic Knight shift discussed in Sec. III.C.3. The solid curve is calculated on the assumption that the solute hyperfine field is produced purely by conduction electron polarization, i.e., directly proportional to the induced lattice magnetization,

$$\beta = 1 + \frac{H_{hf}}{H_{ext}} \quad \frac{\sigma(T,H_{ext})_{Ni}}{\sigma(0,H_{ext})_{Ni}} \qquad (V.2)$$

The excellent agreement between this very simple theory and the data supports the CEP mechanism discussed in Sec. III for the ^{111}Cd hyperfine field in nickel.

Table V.1. ^{111}Cd in Ni below T_c(=628°K).

Temperature °K	T/T_c	$\omega(\frac{\text{radians}}{\text{sec}})\times 10^6$	$\frac{\omega(T)}{\omega(4.2)}$
4.2	0.0067	104.4(2)	[1.000](2)
194.5	0.310	101.3(2)	0.970(3)
293.0	0.467	97.60(20)	0.935(3)
408.0	0.651	88.00(20)	0.843(3)
454.0	0.724	82.55(21)	0.791(3)
501.0	0.799	74.35(10)	0.712(7)
512.0	0.816	71.94(23)	0.689(3)
534.0	0.851	68.24(23)	0.654(2)
569.0	0.907	53.57(31)	0.513(3)
582.0	0.928	49.77(20)	0.477(2)
607.0	0.968	41.63(23)	0.399(2)
621.0	0.973	34.00(21)	0.326(2)

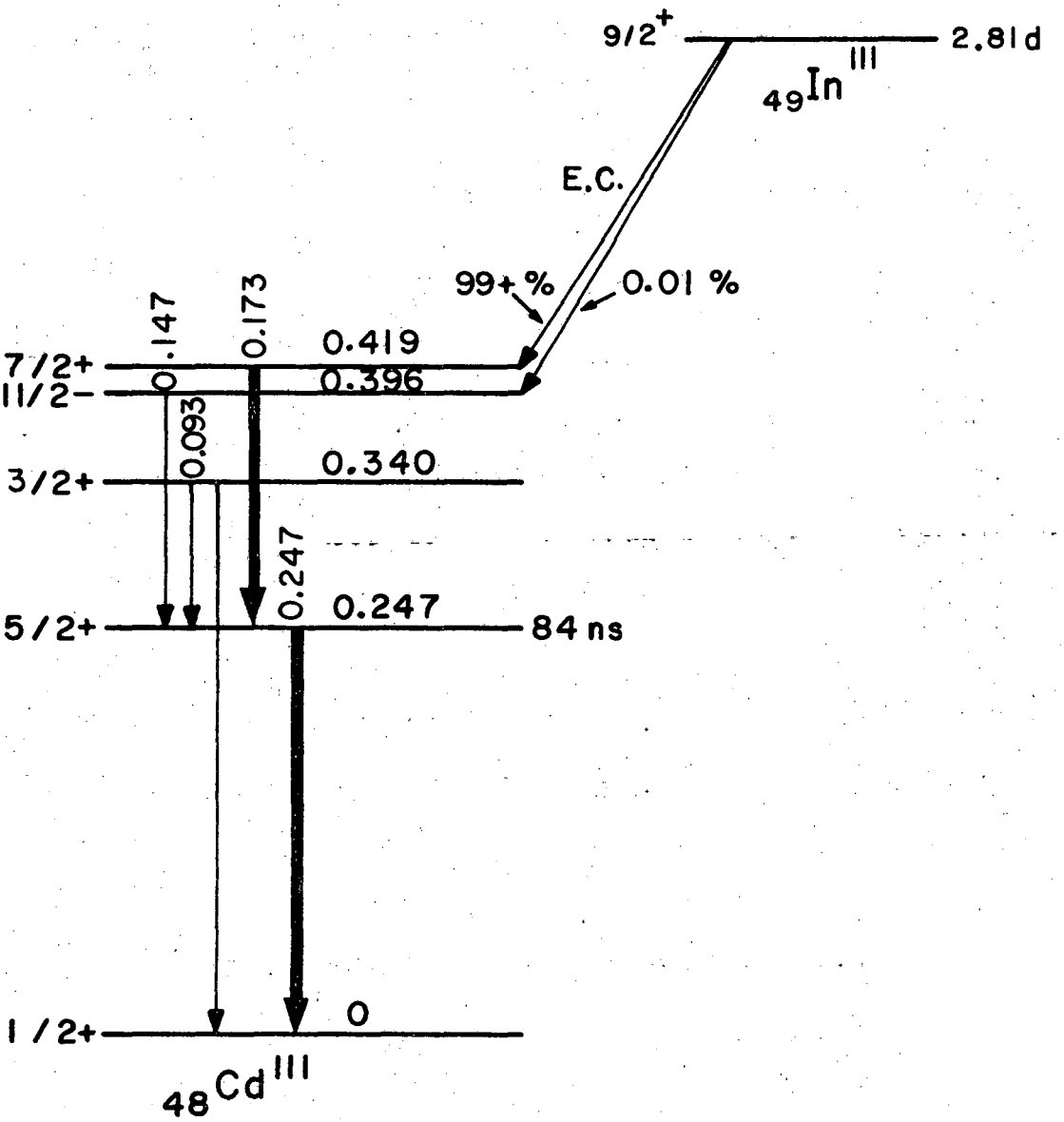
9/2+
2.81d
49In111
E.C.
99+ %
0.01 %
0.147
0.173
0.419
7/2+
11/2-
0
0.396
0.093
0.340
3/2+
0.247
0.247
5/2+
84 ns
1/2+
0
48Cd111
XBL6711-5666

Figure V.1

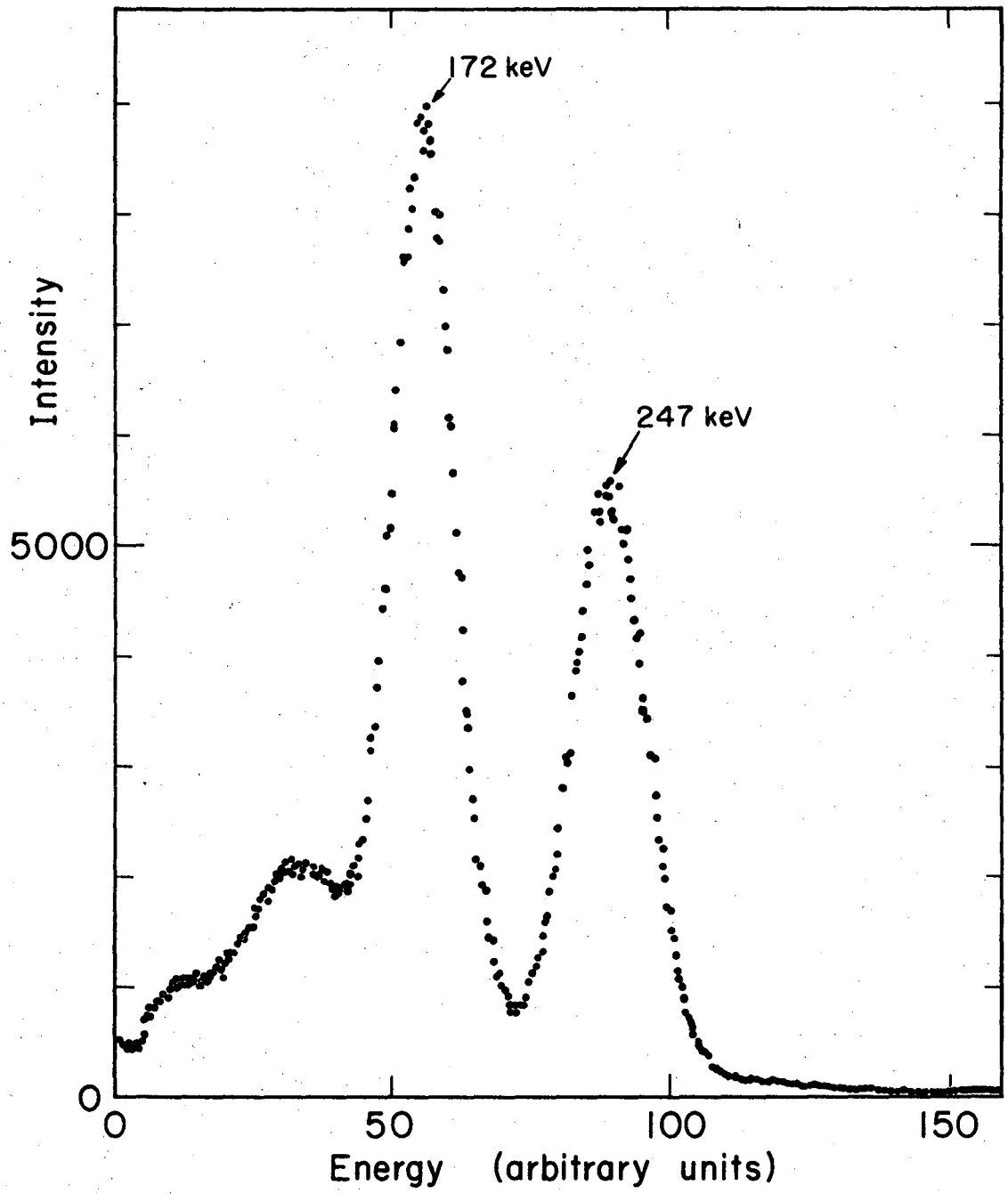

XBL 6812-7501

Figure V.2

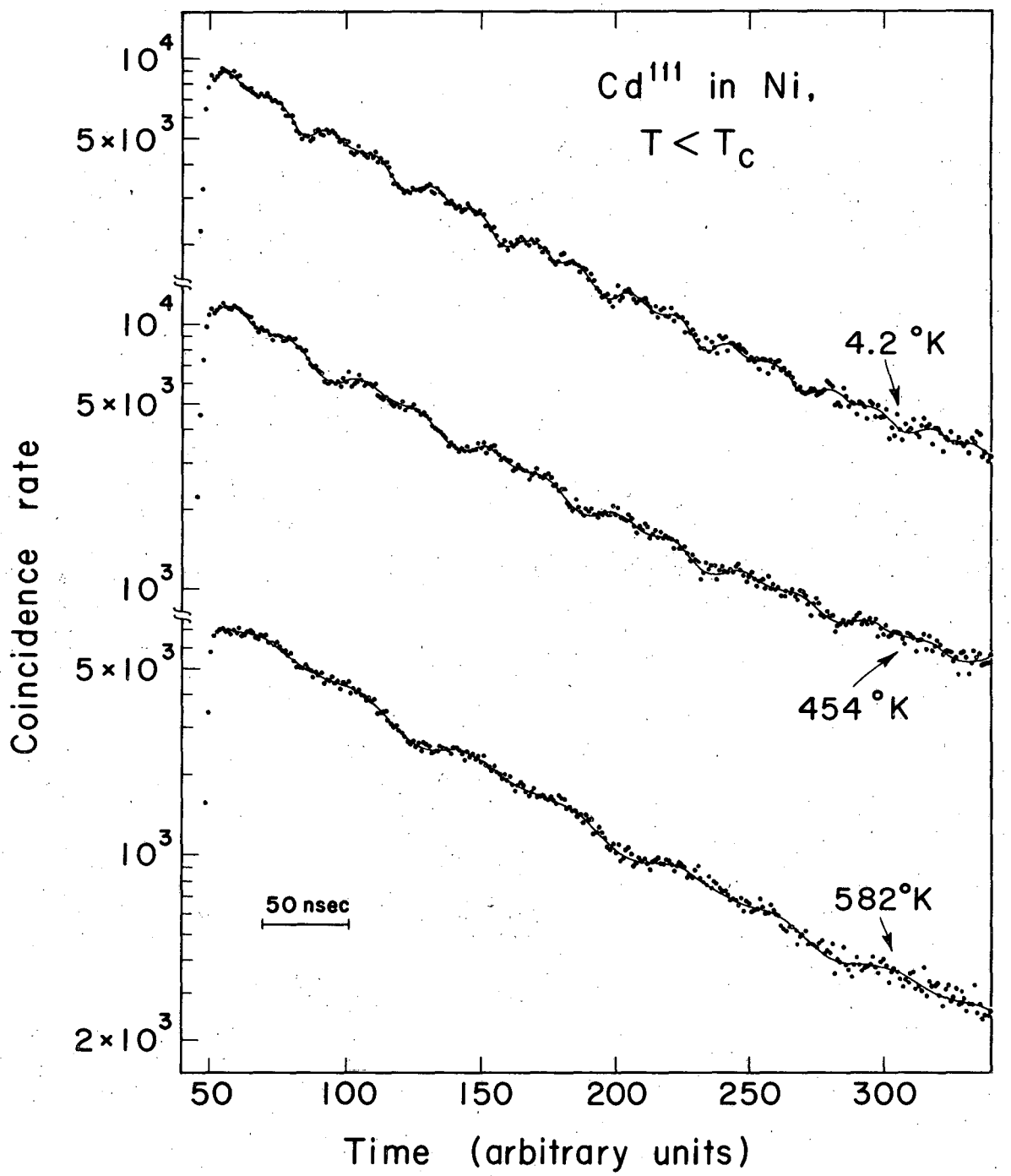
Cd111 in Ni,
T < Tc
4.2 °K
454 °K
582°K
50 nsec
Coincidence rate
Time (arbitrary units)
10^4
5×10^3
10^4
5×10^3
10^3
5×10^3
10^3
2×10^3
50
100
150
200
250
300
MU8-9082

Figure V.3

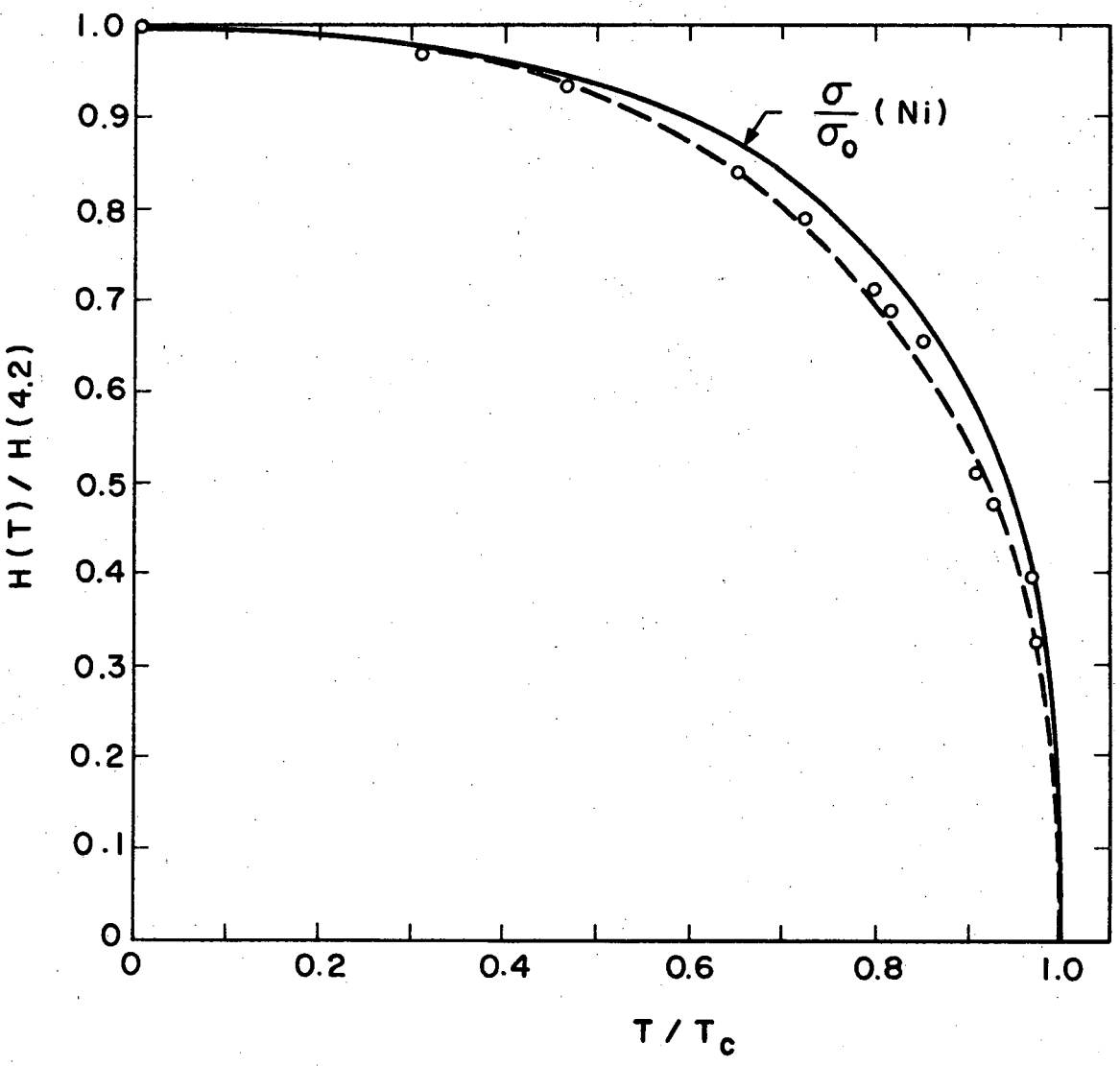
1.0
0.9
0.8
0.7
0.6
0.5
0.4
0.3
0.2
0.1
0
H(T) / H(4.2)
0
0.2
0.4
0.6
0.8
1.0
T / Tc
σ/σo (Ni)
XBL6711-5667

Figure V.4

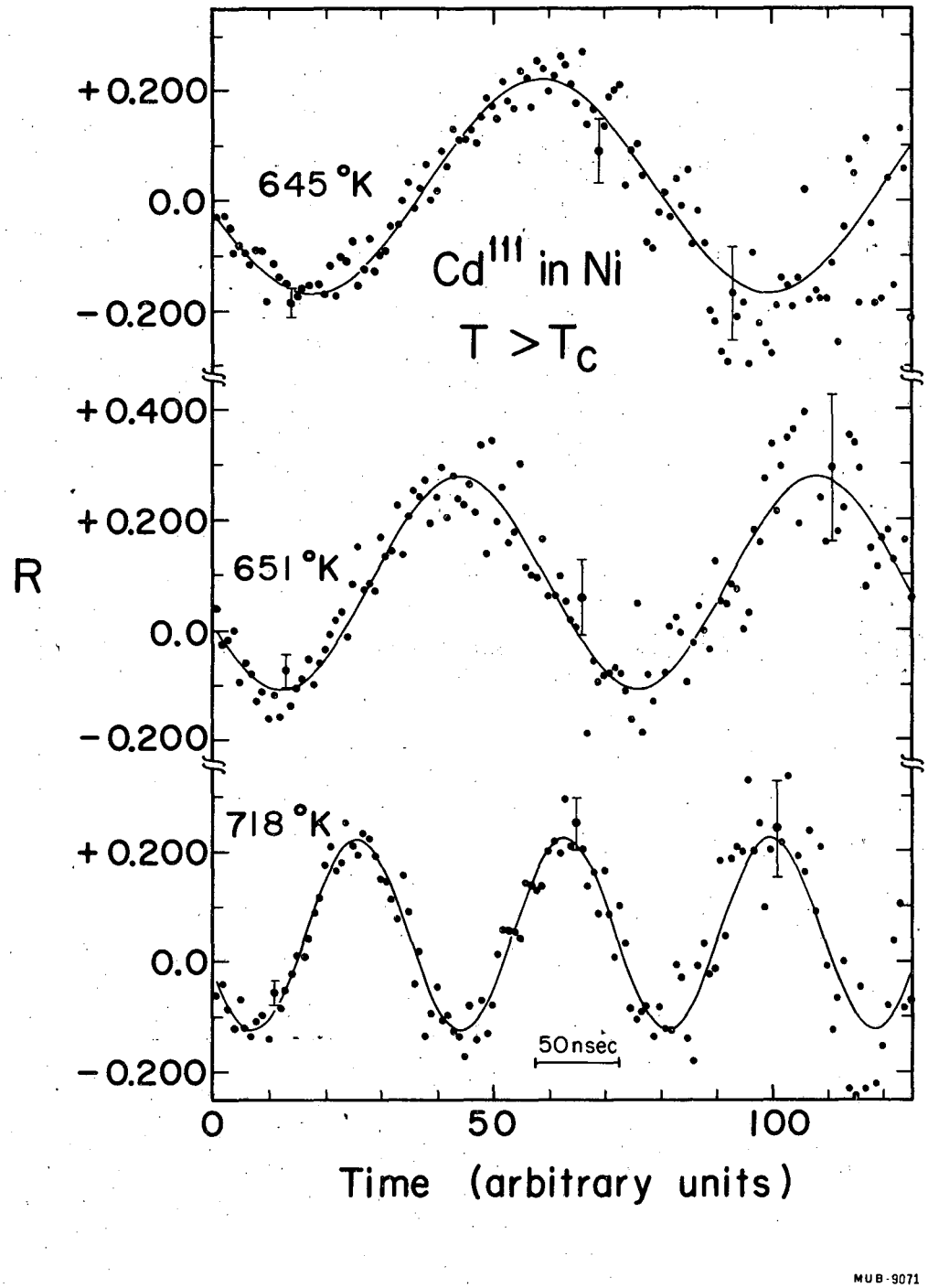
+0.200
0.0
-0.200
645 °K
Cd111 in Ni
T > Tc
+0.400
+0.200
R
651 °K
0.0
-0.200
718 °K
+0.200
0.0
-0.200
50nsec
0
50
100
Time (arbitrary units)
MUB-9071

Figure V.5

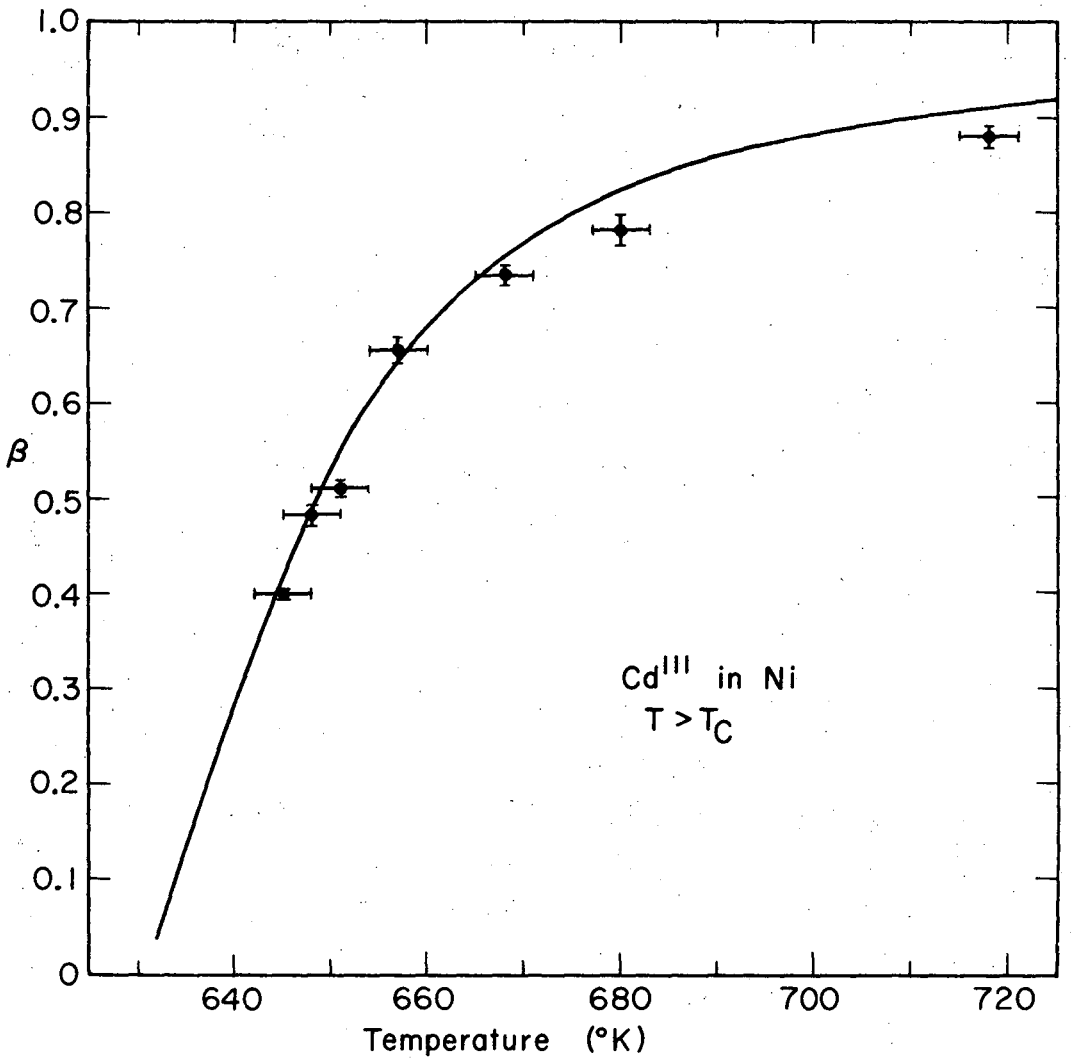
1.0
0.9
0.8
0.7
0.6
β
0.5
0.4
0.3
0.2
0.1
0
640
660
680
700
720
Temperature (°K)
Cd111 in Ni
T > TC
MUB 12003

Figure V.6

VI. RUTHENIUM-99 IN NICKEL

A. Source Preparation

The activity was produced by a (p,n) reaction on ^{99}Ru. Samples of approximately 10 mg of ^{99}Ru metal powder enriched to 98.8% were irradiated with 13 MeV protons at the Berkeley 88" cyclotron. The irradiated powder was then placed inside a weighted nickel container and melted in an argon atmosphere at 1500°C for 30 minutes and quenched to room temperature. The alloys were made up to be 1 atomic percent Ru in Ni. This material, after flattening to a thickness of $\sim$ 1 mm and annealing at 300°C for 1 hour, was used as the source for the experiments reported here.

B. Decay Scheme and Gamma Ray Spectrum

In Fig. VI.1 the pertinent part of the decay scheme of ^{99}Ru is given.[55] The level at 90 keV was that used in all experiments reported here. The decay of the parent ^{99}Rh populates several levels in ^{99}Ru, some of which in turn populate the level at 90 keV. In previous work on this level[56] it was found that both the 354-90 keV and 529-90 keV cascades gave equal counting rates, but the 529-90 keV cascade gave a slightly larger anisotropy. For this reason, the latter cascade was used in all experiments discussed here. A gamma ray energy spectrum of the region of interest, taken with a lithium-drifted germanium detector, is shown in Fig. VI.2.

Since all work was done with NaI(Tl) scintillation detectors, it is clear that the energy windows taken included more than just a single transition. However, these difficulties are small since these

transitions are seen to be weak compared to the 529 and 90 keV and often not in cascade with the 90 keV level. Also, in this previous work,[56] the g-factor was accurately measured [g = -0.189(4)] making it possible to get accurate values for the magnetic hyperfine fields.

C. Results for $T < T_c$

In Fig. VI.3 are shown some typical data for this set of measurements, all of which were carried out in a small external polarizing field. The ordinate is the function,

$$R(t) = \frac{W(3\pi/4,H_{\downarrow},t) - W(3\pi/4,H_{\uparrow},t)}{W(3\pi/4,H_{\downarrow},t) + W(3\pi/4,H_{\uparrow},t)} \qquad \text{(VI.1)}$$

where $W(3\pi/4,H,t)$ is given by Eq. (II.19) with $k_{max} = 2$. For this case, $R(t)$ is of the form

$$R(t) = A\cos(\omega t + \phi) + B \qquad \text{(VI.2)}$$

It is clear, however, that the oscillations are damped out. Therefore we decided to carry out our least-squares fit with the function,

$$R(t) = Ae^{-\lambda t}\cos(\omega t + \phi) + B \qquad \text{(VI.3)}$$

with A, λ, ω, ϕ, and B the adjustable parameters. All the data on ^{99}RuNi for $T < T_c$ was analyzed using Eq. (VI.3).

At the time that these data were reported[21] we were unsure as to whether this damping was due to a magnetic field distribution or to the existence of at least two different magnetic sites for Ru atoms. Recent NMR measurements by Budnick and Murphy[57] on both 0.3 atomic percent Ru in Ni and 1.3 atomic percent Ru in Ni and earlier work by Kubo et al.[58] indicate that as concentration of Ru increases, the single, slightly asymmetric Ru resonance broadens, becomes more asymmetric and shifts to lower frequency. Also, in the 1.3 atomic percent Ru data there is a pronounced satellite peak below the main peak. This is shown in a plot of Budnick and Murphy's data in the inset in Fig. VI.4. Since this satellite does not appear in the 0.3 atomic percent data, this is strong evidence that it is due to Ru-Ru interactions. As a further check of the consistency of our data with Budnick and Murphy's, we have fitted their 1.3 atomic percent Ru data roughly with Lorentzian lineshapes to find the centroids and linewidths of the peaks. We then plot the Fourier transform of these lines, normalized to our data on RuNi at 4.2°K. Since our alloy was 1 atomic percent Ru the results should be comparable. The rough Fourier transform plotted over our data is shown in Fig. VI.4. It is to be emphasized that this is not a fit and does not take account of the fact that different applied fields were used. It also does not take into account the pronounced asymmetry in the NMR lineshape.

The final results for ^{99}RuNi for $T < T_c$ are given in Table VI.1 and plotted in Fig. VI.5. The Curie temperature of our 1 atomic percent Ru in Ni alloy was determined by extrapolating the measured induced magnetization vs. temperature curve at its region of greatest slope. T_c was found to be 610°K, in very good agreement with the results of Sadron.[59]

The two broken curves in Fig. VI.5 are those calculated from Eq. (III.12), for $j = \frac{1}{2}$ and $j = \frac{5}{2}$. It is clear that the quality of the fit to the data is equally good in these two cases. In fact, for all $\frac{1}{2} \leq j \leq \frac{5}{2}$ the fits were uniformly good, thus indicating that one cannot uniquely determine the spin of the local moment from this type of analysis. The values of f and ζ for the best fits for all spins, j, are given in Table VI.2. It may be noted from Table VI.2 that the fit for $j = \frac{1}{2}$ requires the smallest contribution from polarized conduction electrons (19%). This indicates that the JWW model would probably give a best fit for this case.

It may also be noted that the model described by Eq. (III.11) requires the separability of $H_c(0)$ and $H_L(0)$. Since the local moment probably carries the conduction electrons through s-d exchange, this assumption is somewhat dubious. An indication of this lack of rigor is that $H_c(0)$ and $H_L(0)$ are predicted to be antiparallel, a result contrary to all previous experience.

In view of this quantitative failure of the model, the following calculation of the magnitude of the local moment is given as a <u>qualitative</u> estimate, using the results for $j = \frac{1}{2}$ (Table VI.2). From Eq. (III.11), $H_L(0) = fH_{hf}(0) = (1.194)(217)$kG, and making the same arguments as for Eq. (III.4) assuming $g = 2.0, \langle \mu_z \rangle = \frac{(1.194 \times 217)}{370} = 0.7$ Bohr magneton.

Using the arguments in Sec. III on hyperfine field systematics, Shirley, Rosenblum, and Matthias[21] calculate a local moment for Ru in Ni of 0.4 Bohr magnetons. This lack of quantitative agreement is not surprising in view of the crude assumptions inherent in both methods.

In summary, two comments may be made about ^{99}RuNi:

1. Both methods of analysis, hyperfine field vs. atomic number and H(T)/H(0), agree that a local moment is present.
2. The magnitude of the local moment is not well established as these methods do not agree very well. However, for Ru in Ni it seems likely that $S \leq 1$.

D. Results for $T > T_c$

In raising the alloy temperature above T_c, it no longer was possible to use TDPAC since the precession frequency becomes too small to observe in this manner, even in an external field of 19.5 kOe. Thus it was necessary to use the less accurate time integral perturbed angular correlation technique. The integral results were then normalized to several time-differential results at high temperatures. The data consisted of counts for field up and field down at a fixed detector angle of 135°. The results are displayed in Fig. VI.6. The horizontal line for $\beta = 1$ would be the expected behavior if the Ru moment were completely localized above T_c. The lower curve corresponds to the reduced magnetization of pure nickel. It is reasonable that the hyperfine field lie between these limits.

Two points should be made regarding these data. First and foremost, since they measure the time integrated spectrum, we can say nothing about the time dependence (or equivalently, the frequency spectrum) of the source. Thus, if any relaxation effects were to occur, such as will be seen to occur for ^{100}RhNi in Sec. VII, these would require modification of our data analysis.

Secondly, since it appears that the hyperfine field for ^{100}Rh in Ni tends to follow the lattice magnetization above T_c, and since ^{100}Rh in Ni is expected also to form a local moment, this casts some doubt on the idea that this hyperfine field dependence is accurate.

Table VI.1. ^{99}Ru in Ni below T_c (=610°K for 1 atomic % alloy).

Temperature °K	T/T_c	$H_{hf}(T)$ kOe	$\frac{H_{hf}(T)}{H_{hf}(4.2)}$
4.2	0.00656	217.20(113)	[1.000](7)
77.0	0.126	212.50(147)	0.978(8)
194.5	0.319	206.58(45)	0.951(6)
298.0	0.489	175.60(148)	0.808(8)
396.0	0.649	141.70(338)	0.652(16)
444.0	0.728	126.39(319)	0.582(15)
506.0	0.829	98.89(271)	0.455(13)
568.0	0.931	60.00(166)	0.276(8)

Table VI.2. ^{99}Ru in Ni.

$$\frac{H(T)}{H(4.2)} = (1-f)\,\frac{\sigma}{\sigma_0} + f\,B_J\left(\zeta\frac{\sigma}{\sigma_0}\cdot\frac{T_c}{T}\right) \qquad T_c = 610^\circ K$$

Values of parameters for best fits

J	f	ζ
1/2	1.194	0.621
1	1.490	1.049
3/2	1.965	1.416
2	2.209	1.662
5/2	1.958	1.757

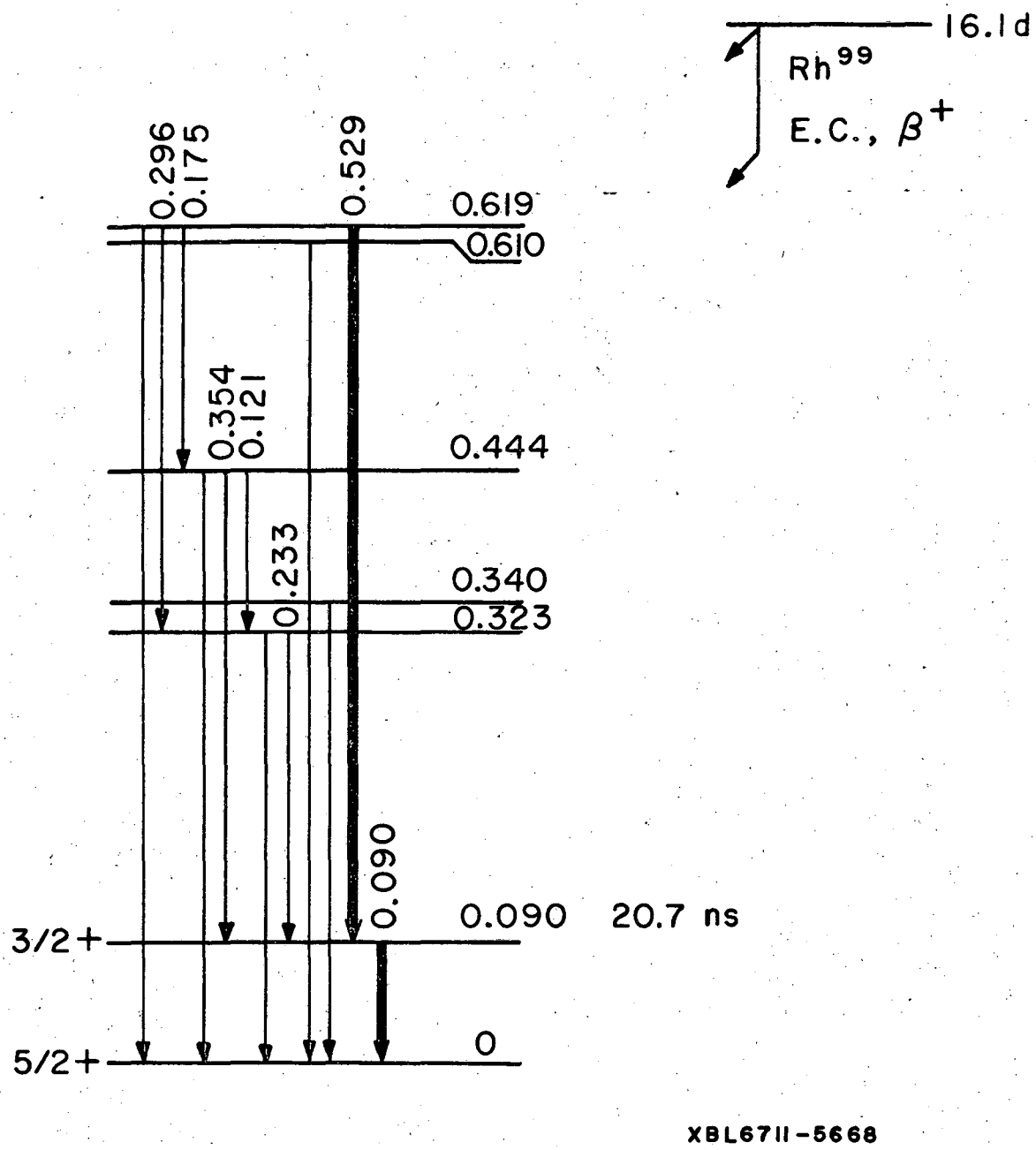
16.1d
Rh 99
E.C., β+
0.296
0.175
0.529
0.619
0.610
0.354
0.121
0.444
0.233
0.340
0.323
0.090
0.090
20.7 ns
3/2+
0
5/2+
XBL6711-5668

Figure VI.1

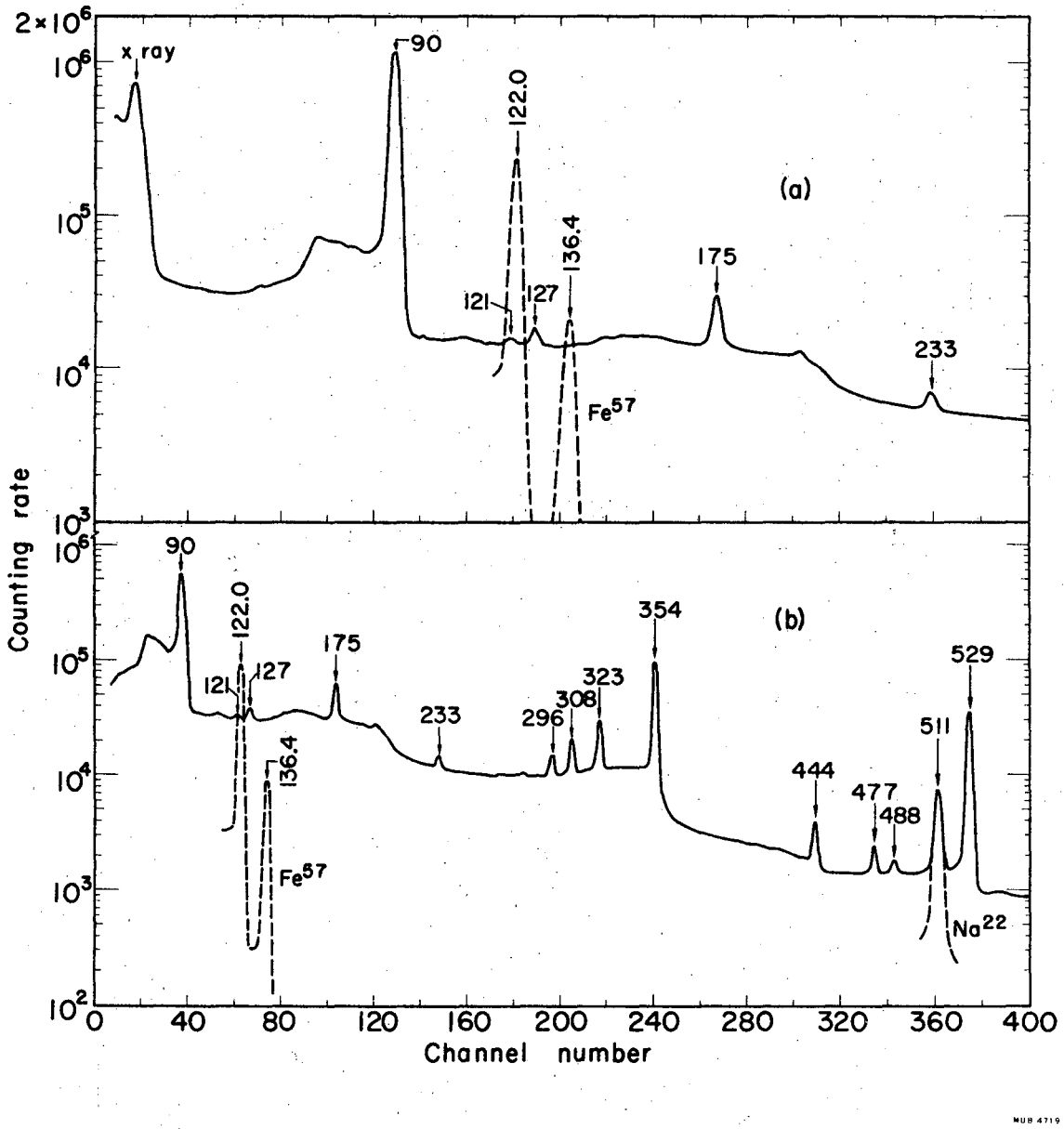
2×10^6
10^6
10^5
10^4
10^3
x ray
90
122.0
136.4
121
127
175
233
Fe^57
(a)
Counting rate
90
122.0
121
127
136.4
175
233
296
308
323
354
(b)
529
511
444
477
488
Na^22
Fe^57
10^2
0
40
80
120
160
200
240
280
320
360
400
Channel number
MUB 4719

Figure VI.2

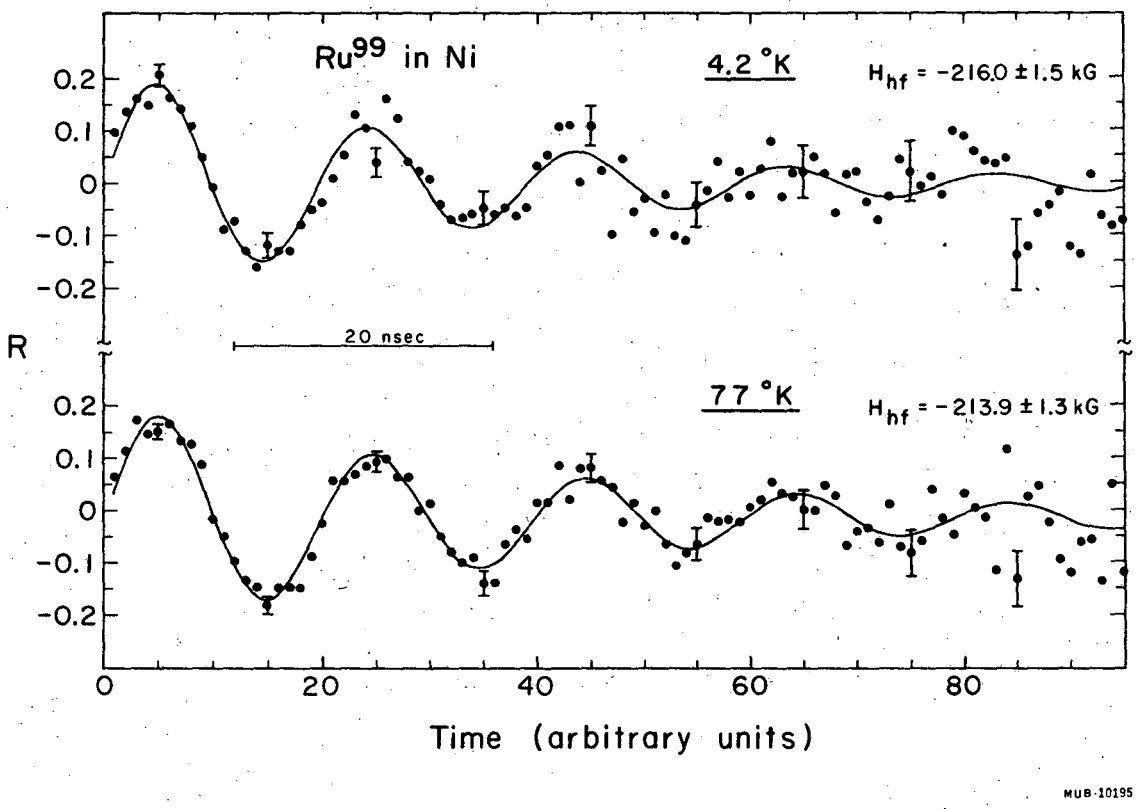
Ru99 in Ni
4.2 °K
Hhf = -216.0 ± 1.5 kG
77 °K
Hhf = -213.9 ± 1.3 kG
20 nsec
R
0.2
0.1
0
-0.1
-0.2
0
20
40
60
80
Time (arbitrary units)
MUB-10195

Figure VI.3

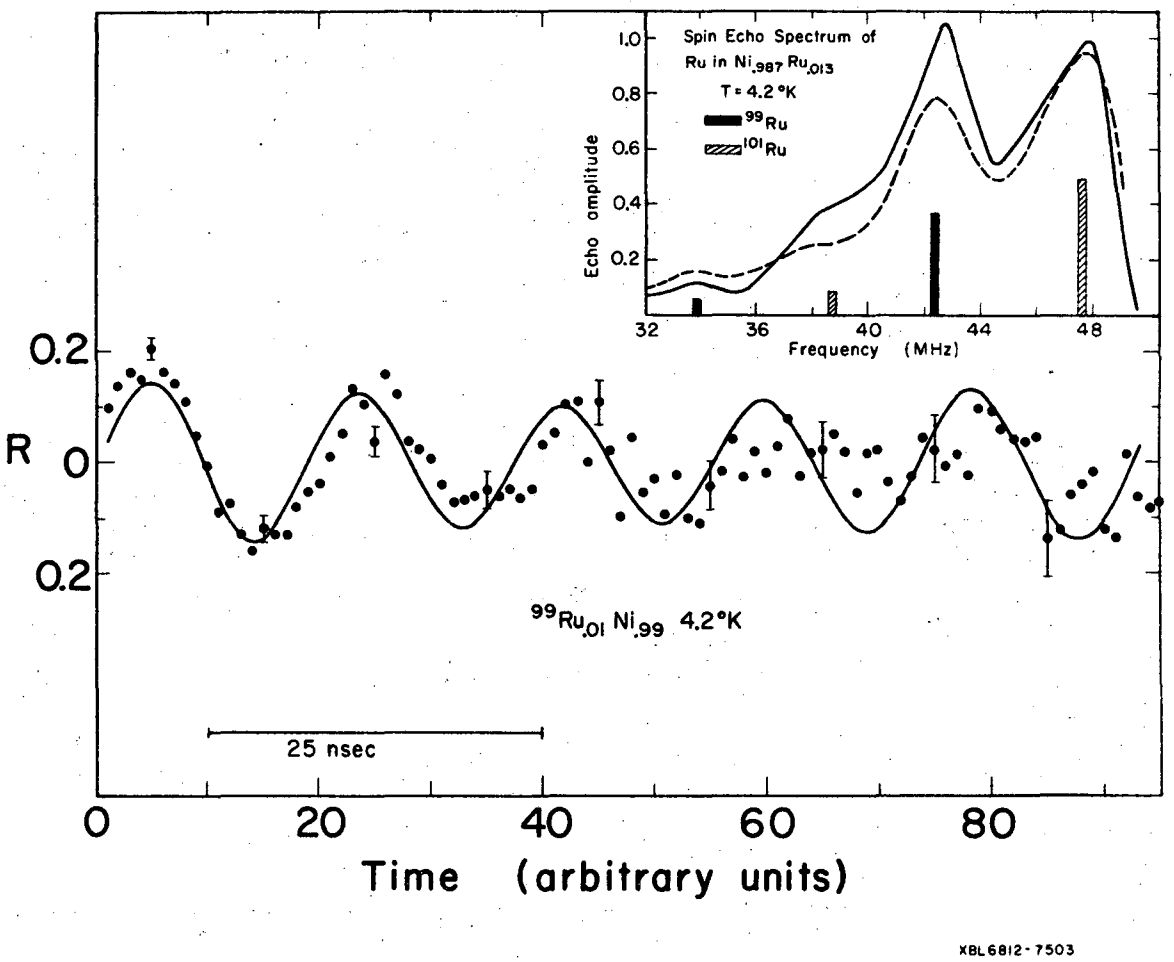
Spin Echo Spectrum of
Ru in Ni.987 Ru.013
T = 4.2 °K
99Ru
101Ru
Echo amplitude
1.0
0.8
0.6
0.4
0.2
32
36
40
44
48
Frequency (MHz)
0.2
R 0
0.2
99Ru.01 Ni.99 4.2°K
25 nsec
0
20
40
60
80
Time (arbitrary units)
XBL6812-7503

Figure VI.4

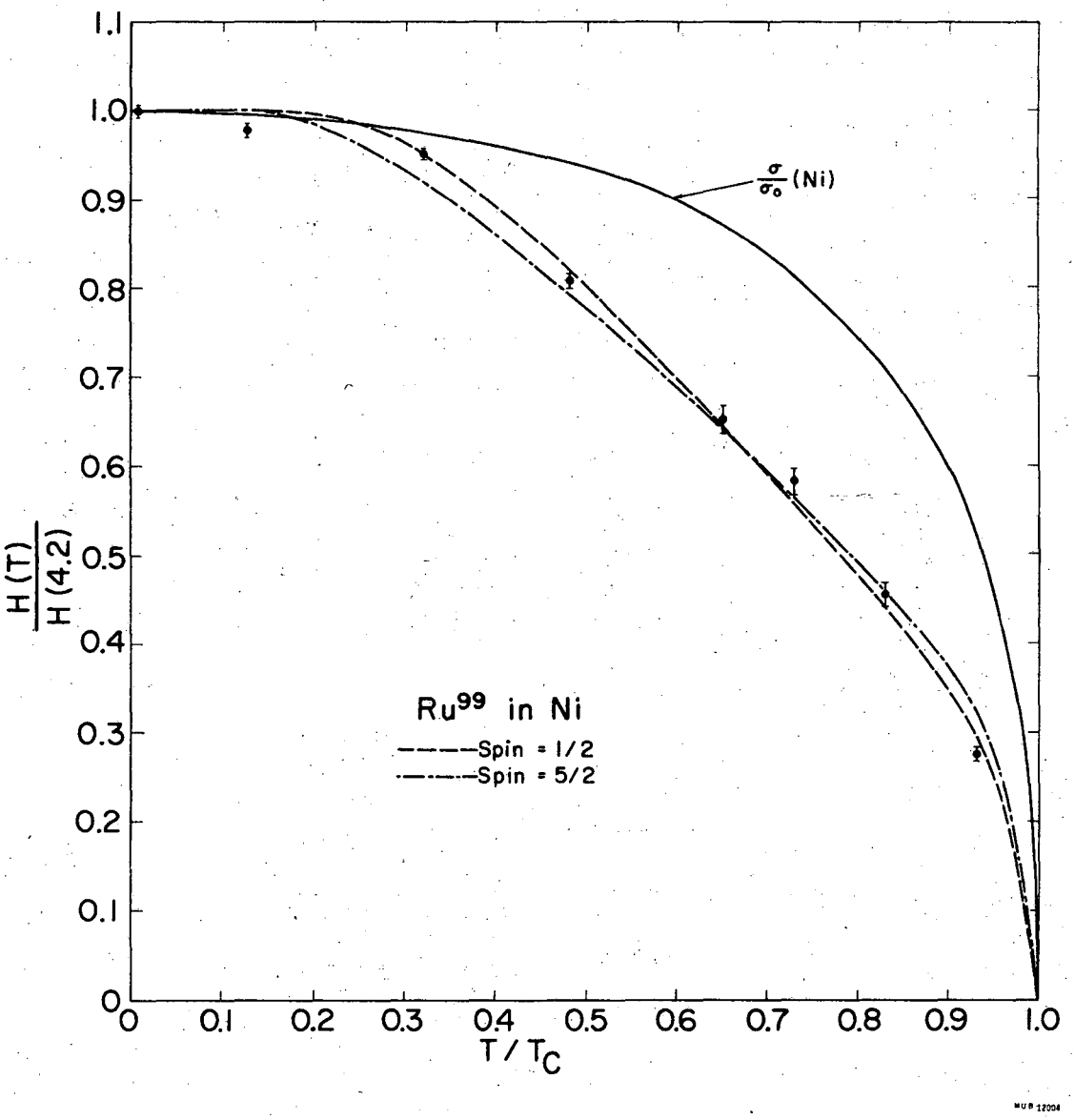
1.1
1.0
0.9
0.8
0.7
0.6
0.5
0.4
0.3
0.2
0.1
0
0
0.1
0.2
0.3
0.4
0.5
0.6
0.7
0.8
0.9
1.0
H(T)/H(4.2)
T/Tc
σ/σ0 (Ni)
Ru99 in Ni
Spin = 1/2
Spin = 5/2
MUB 12004

Figure VI.5

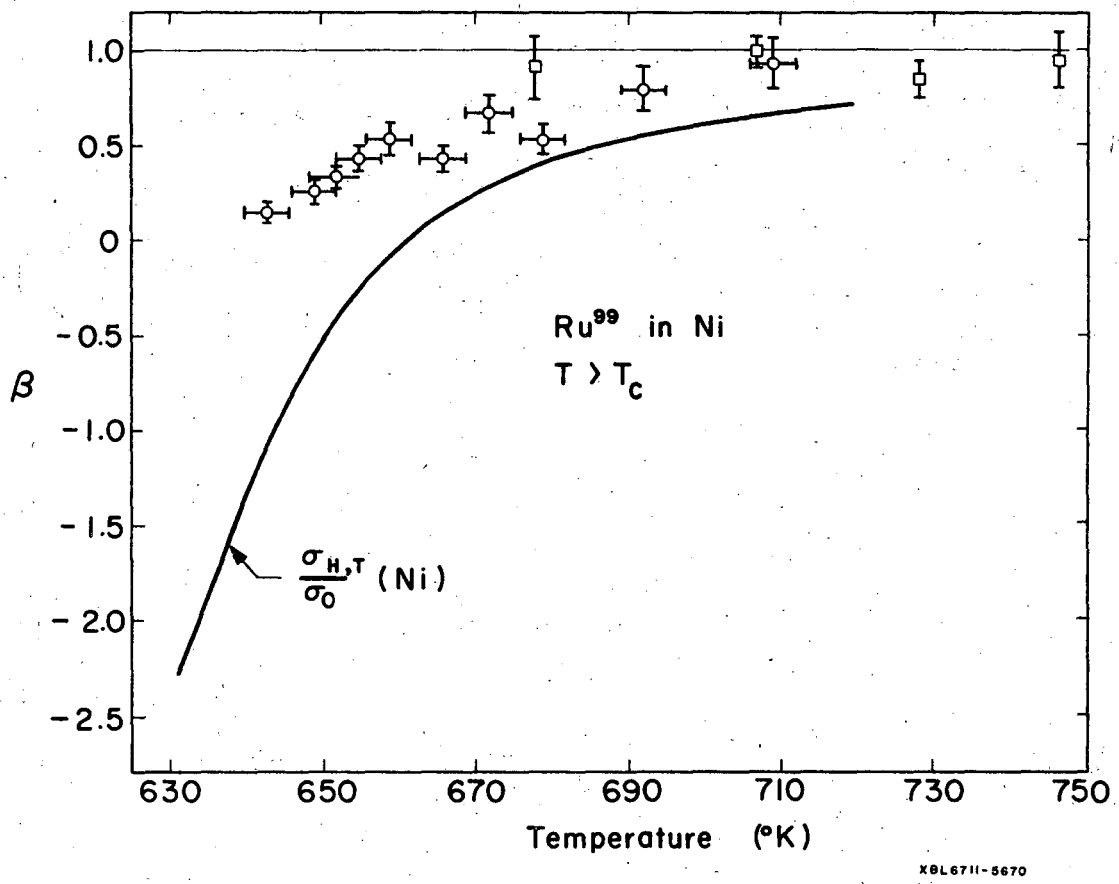
1.0
0.5
0
-0.5
-1.0
-1.5
-2.0
-2.5
β
630
650
670
690
710
730
750
Temperature (°K)
Ru99 in Ni
T > Tc
σH,T/σ0 (Ni)
XBL6711-5670

Figure VI.6

VII. RHODIUM-100 IN NICKEL

A. Source Preparation

The parent ^{100}Pd was produced by a (p,4n) reaction on natural rhodium metal powder which was carefully purified and spectroscopically analyzed. It was found to have less than .01% Pd, Fe, and Co. The only significant impurity was $\sim$.1% Cu. The samples were irradiated with 45 MeV protons at the Berkeley 88" cyclotron at a total integrated flux of 20 μamp-hrs. The radioactive ^{100}Pd was separated from the target using a procedure similar to that described by Evans et al.[60] and is basically as follows:

1. Place $\approx$100 mg. target material in a crucible and fuse at dull red heat with 20 ml. $KHSO_4$ powder for 30 minutes.
2. Dissolve the fusion in 100 ml. of boiling water.
3. Cool the solution and add 0.5 ml. of a saturated solution of dimethyl glyoxime in ethanol. This forms a complex with the palladium. This complex is then solvent-extracted into chloroform.
4. Wash the chloroform twice with 1N H_2SO_4 and then back-extract the Pd with 14 M NH_4OH. Evaporate this solution almost to dryness.
5. Take up the remainder in a minimum volume of 0.05 M $(NH_4)_2SO_4$ solution and adjust to pH 11 with NH_4OH.

The carrier free ^{100}Pd was plated from this solution onto either a 0.5 mil Ni foil or an Ni single crystal, both of 5-9's purity. The sources were then sealed inside cleaned quartz tubes with 10^{-3} torr of H_2 gas

inside. The foils were then melted for 30 minutes at 1475°C, removed from the furnace, rolled out to ≈.001" in thickness and annealed for 12 hours at 1200°C inside a similarly sealed quartz tube.

The plated single crystal samples were similarly sealed inside quartz tubes and the activity diffused in at 1200°C for 12 hours.

These sources were then mounted in the furnace described in Sec. IV.E.3.

B. Decay Scheme and Gamma Ray Spectrum

In Fig. VII.1 the pertinent part of the decay scheme of the 4.0 day ^{100}Pd parent is shown. 96% of the decays populate the 158.8 keV level which decays 70% through the 84.0-74.8 keV cascade. The anisotropy of this cascade has been shown to be large (A=+(29.7±1.8%)) and the g-factor has been accurately measured (g=2.151(4)).[61]

Since the energies of these two transitions are so close, it was necessary to employ lithium-drifted germanium detectors to resolve the energies. A gamma-ray energy spectrum of the region of interest taken with one of these detectors is shown in Fig. VII.2.

C. Temperature Dependence of the Magnetic Hyperfine Field

Figures VII.3 and VII.4 present some data taken in a transverse magnetic field and at an angle of 180° between the detectors. The data was least-squares fitted to a function of the form

$$W_{\perp}(\pi,H_o,t) = Ae^{-t/\tau_N}\left\{1 + Be^{-3t/T_1}\left[1 - 3e^{-4t(1/T_2-1/T_1)}\right.\right.$$

$$\left.\left.\cos(2\omega_L t + \phi)\right]\right\} + C \qquad \text{(VII.1)}$$

with A, τ_N, B, T_1, T_2, ω_L, ϕ, and C the adjustable parameters. This form of the equation is obtained from the theory of Gabriel described in Sec. II.C, replacing the spectral density functions by the better known T_1 and T_2, the longitudinal and transverse relaxation times. For our data we always set $T_1 = T_2$.

It is clear from the data that in a constant applied field the relaxation rate is slow at high temperatures and increases as the temperature decreases. This behavior will be discussed in the next part of this section.

All the data taken on the hyperfine field of ^{100}Rh<u>Ni</u> are presented in Fig. VII.5. Here we have again plotted β vs. temperature. The solid curve was calculated assuming only CEP contributions to H_{eff}, i.e., with $H_L(0) = 0$ in Eq. (IV.13) using $H_{hf}(0) = 213$ kOe.[62] The agreement of this curve with the data is strong evidence that there is <u>no</u> local moment for Rh in Ni above T_c. This, of course, in no way determines whether a local moment does or does not exist below T_c.

At present a series of experiments is being carried out in this laboratory by Quitmann and Pollak[63] on ^{100}Rh<u>Ni</u> below T_c. They are using the technique of nuclear magnetic resonance destruction of angular correlations[64] and are attempting to determine the temperature dependence of

the hyperfine field. Preliminary indications are that a local moment, if present, is not as large as that found for ^{99}Ru.

D. Nuclear Magnetic Relaxation

The attenuation of the TDPAC pattern could result from either a static or a time-dependent interaction. The static interaction could arise from either an anisotropic magnetic interaction, a quadrupole interaction, a broad magnetic field distribution or different magnetic sites (as is probably the case for our RuNi data).

In order to eliminate the first two possibilities, we performed measurements on ^{100}Rh in single crystals of nickel. These experiments were carried out by mounting the single crystal in the Gamma furnace, allowing it to stabilize at a constant temperature and applied field and rotating the entire furnace so that the (100) and (111) crystal axes were alternately parallel to the applied field. The detectors were in a plane perpendicular to the field direction at an included angle of 180°. The values of ω_L from these measurements, obtained by least-squares analysis using Eq. (VII.1), are given in Table VII.1. There is clearly no difference between these results and those from polycrystalline samples.

Since our samples were very dilute in Rh and Pd (less than 10 ppm by spectroscopic analysis), it is unlikely that two different magnetic sites could appear since these would have to arise from Rh-Rh interactions.

To further establish that our results were due to a time dependent interaction, we performed several decoupling experiments. As is well known,[8] if one applies a large magnetic field parallel to one of the

propagation directions, all static interactions on the nucleus can be decoupled. In the absence of time dependent interactions the unperturbed angular correlation is restored. A set of raw data from one of these experiments, in which one detector is placed along the field direction and the other is moved between the 180° and 90° positions, is shown in Fig. VII.6. These data clearly show that the anisotropy still disappears, indicating that the interaction is time dependent.

Using Gabriel's formalism,[18] we find that the angular distributions for these geometries are,

$$W_{\parallel}(\pi,H_o,t) = Ae^{-t/\tau_N}(1 + Be^{-3t/T_1}) \qquad \text{(VII.2a)}$$

$$W_{\parallel}(\pi/2,H_o,t) = Ae^{-t/\tau_N}(1 - \frac{B}{2}e^{-3t/T_1}) \qquad \text{(VII.2b)}$$

From least-squares analysis of these data we are able to extract T_1, while from the experiments described by Eq. (VII.1) we get a combination of T_1 and T_2. From measurements under the same conditions of temperature and applied magnetic field, we can extract T_1 and T_2 separately. These results are displayed in Table VII.2, where T_1 is seen to be equal to T_2 within two standard deviations.

The magnetic field dependence of this relaxation rate is demonstrated by the data presented in Fig. VII.7. According to the exchange-narrowing model developed in Sec. III.C.3 we expect to see a linear relationship between the relaxation rate and the square of the induced

magnetization. This expectation is borne out by Fig. VII.8, where all the relaxation rate data is presented.

As a further check of the consistency of our model with the data, we need to make an order of magnitude calculation of the relaxation rate using Eq. (III.23b). Following Silbernagel et al.,[47] we calculate τ_c by assuming that it arises from indirect coupling of the d-spins. Using the "golden rule" and the free-electron gas density-of-states,

$$\tau_c = \frac{\hbar E_f}{J_{sd}^2} \approx (7\times10^{-14}\ \text{ev-sec})\ \frac{(3\text{ev})}{(.2\ \text{ev})^2} = 5\times10^{-12}\ \text{sec} \qquad \text{(VII.3)}$$

J_{sd} is the exchange integral between s and d electrons and is taken from a paper by Salamon.[65]

If we now insert this value into Eq. (III.23b), taking $z = 12$, $A/\hbar \approx 2\times10^9$ rad/sec, and $\sigma/Ng\beta \approx 1/60$,[54]

$$\frac{1}{T_2} \sim 30 \times [2\times10^9]^2 \times [5\times10^{-12}]\ [2\times10^{-2}]^2 \sim 2\times10^5\ \text{sec}^{-1}$$

This underestimate of the rate by an order of magnitude is disturbing, but might be expected in view of the crudity of our assumptions. However, the good agreement in functional dependence indicates that the model does take account of the principal features of the relaxation rate.

It should also be pointed out that this relaxation rate is much faster than would be predicted by the Korringa relation, which does not take the exchange interaction into account, and which also predicts the wrong temperature dependence.

Table VII.1. ^{100}Rh in Ni single crystal.

Temperature (°C)	Magnetic field (gauss)	Crystal axis	$\omega_L (10^6 \frac{rad}{sec})$
365	200	111	8.3(6) 8.1(8) 11.4(9) } $\langle \omega_L \rangle = 8.9(6)$
		100	8.1(8) 9.4(8) } $\langle \omega_L \rangle = 8.8(6)$
362	200	111	18.0(19)
		100	18.2(9)

Table VII.2. ^{100}RhNi-relaxation rates.

Temperature °C	Magnetic field (gauss)	T_1 (nanoseconds)	T_2 (nanoseconds)
360	164	930(160)	580(65)
365	164	1670(600)	1000(140)

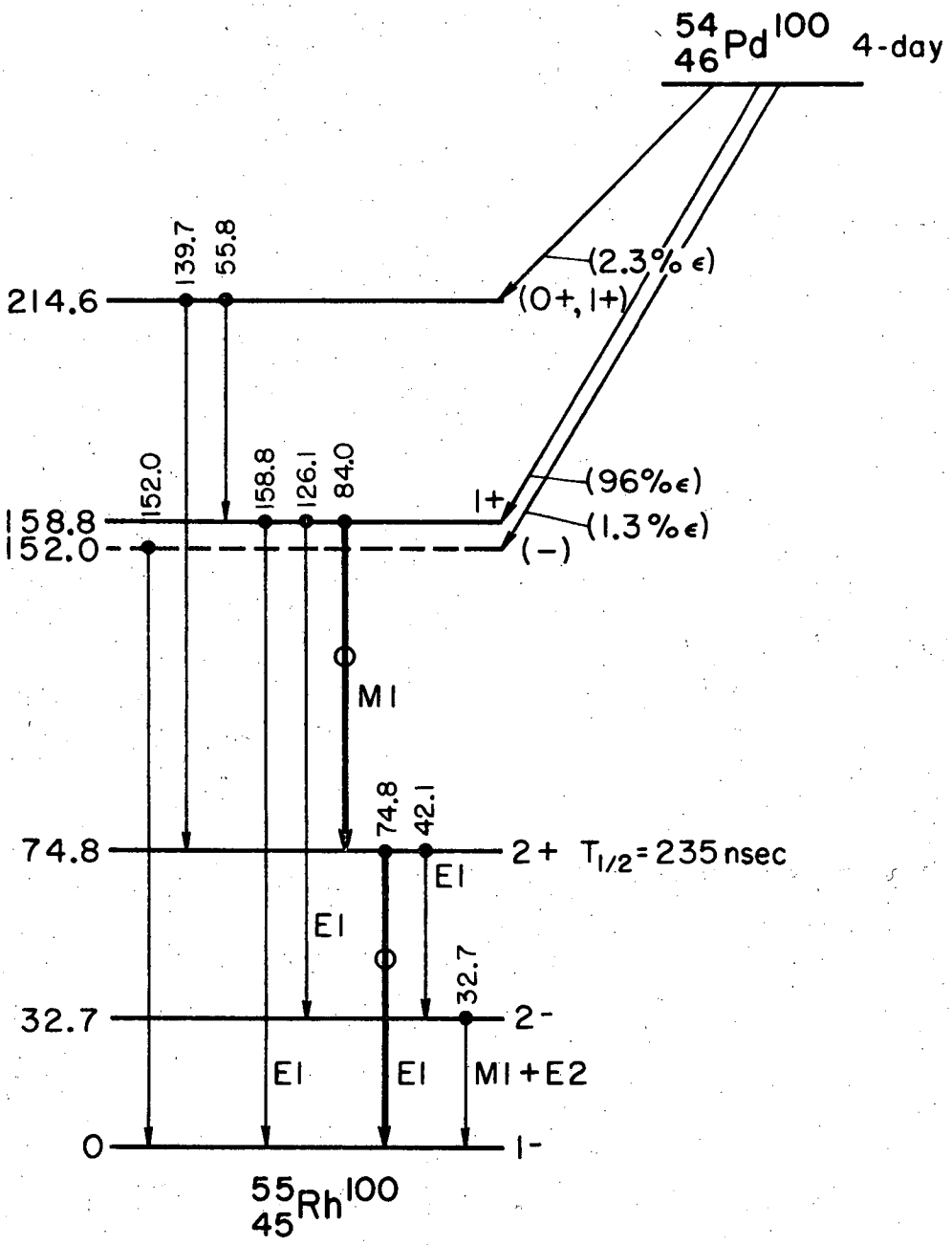
$^{54}_{46}Pd^{100}$ 4-day
(2.3% ε)
(0+, 1+)
214.6
139.7
55.8
(96% ε)
1+
(1.3% ε)
158.8
152.0
(−)
152.0
158.8
126.1
84.0
M1
74.8
42.1
2+ $T_{1/2}$ = 235 nsec
E1
E1
32.7
2−
E1
E1
M1+E2
0
1−
$^{55}_{45}Rh^{100}$
MUB-6309

Figure VII.1

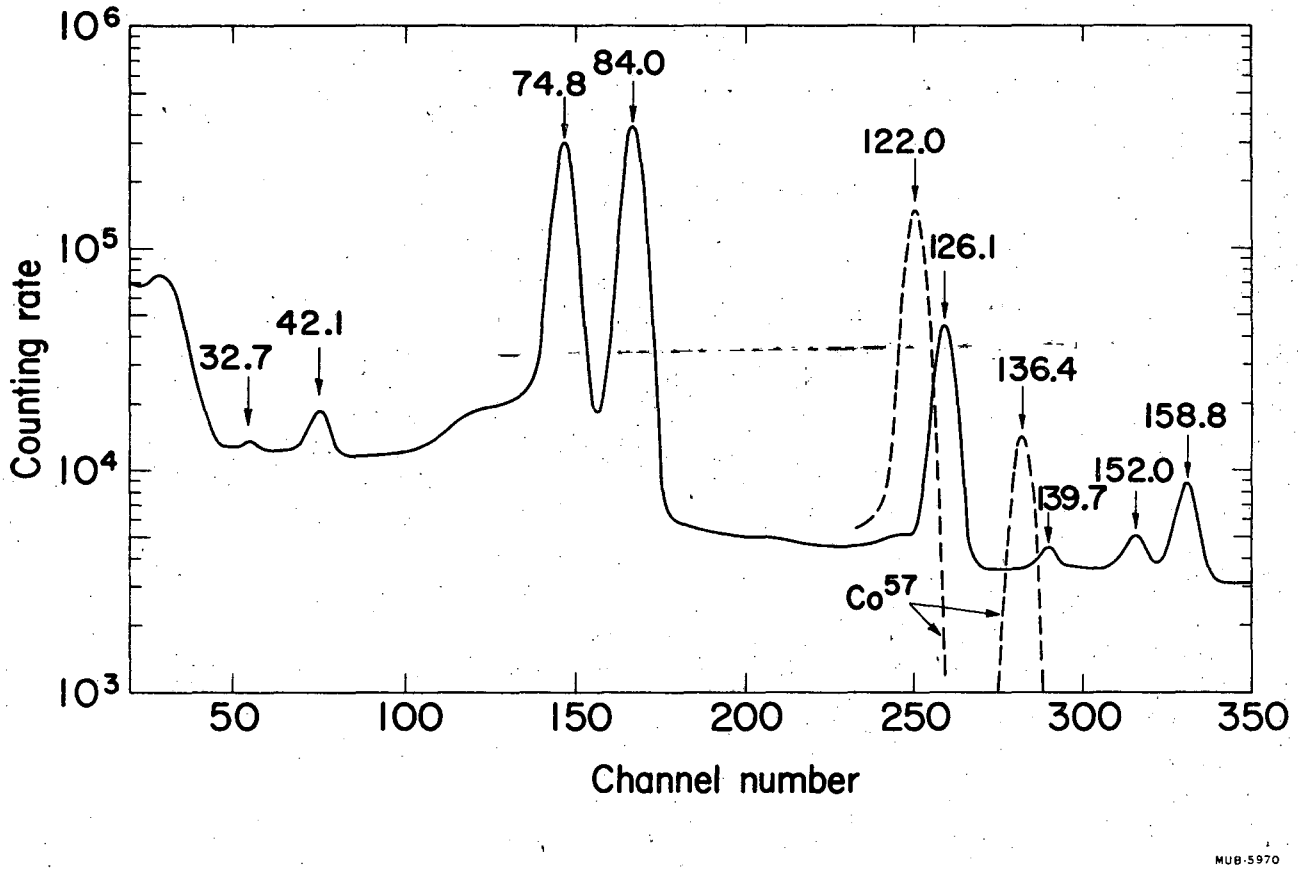
10^6
10^5
10^4
10^3
Counting rate
74.8
84.0
122.0
126.1
32.7
42.1
136.4
158.8
152.0
139.7
Co^57
50
100
150
200
250
300
350
Channel number
MUB-5970

Figure VII.2

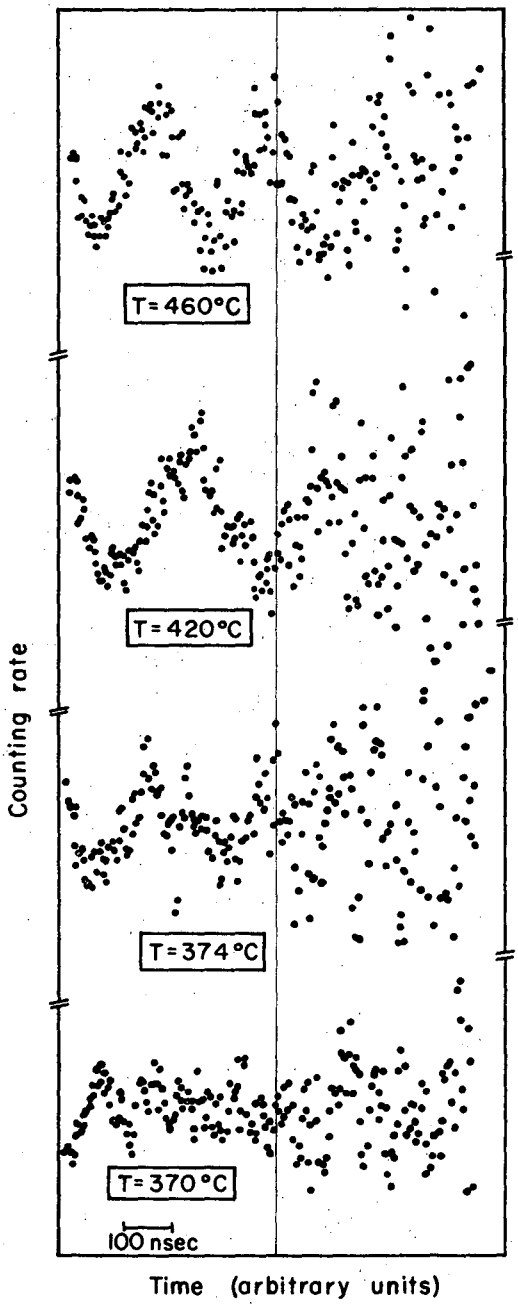
T=460°C
T=420°C
T=374°C
T=370°C
100 nsec
Counting rate
Time (arbitrary units)
XBL6812-7500

Figure VII.3

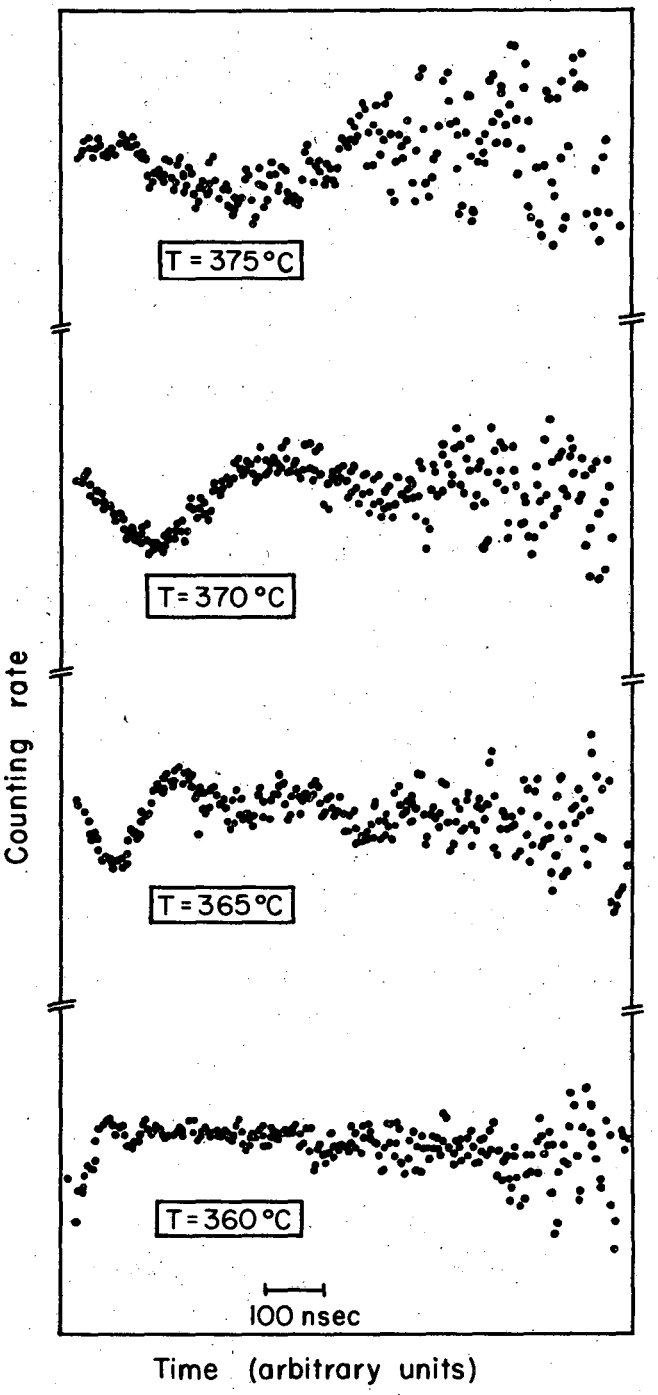
T = 375 °C
T = 370 °C
T = 365 °C
T = 360 °C
Counting rate
100 nsec
Time (arbitrary units)
XBL691-1527

Figure VII.4

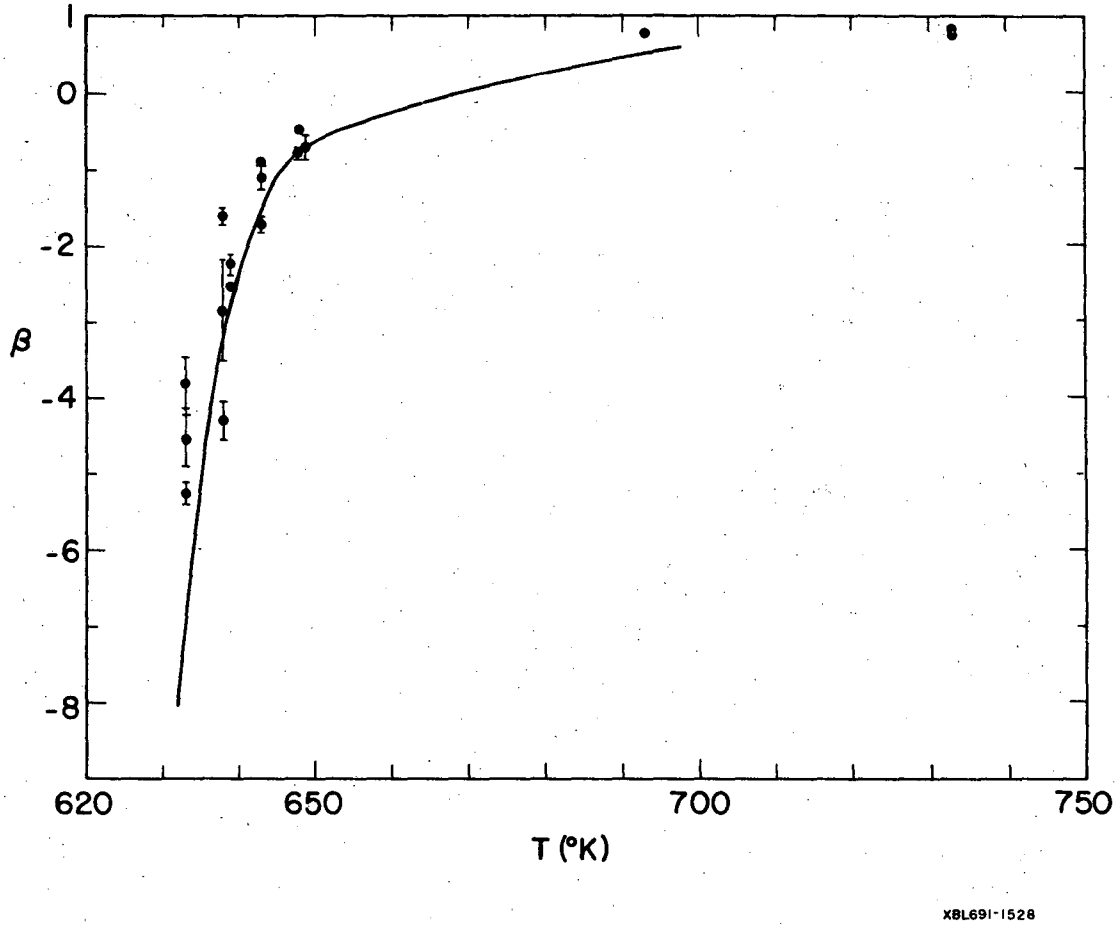

Figure VII.5

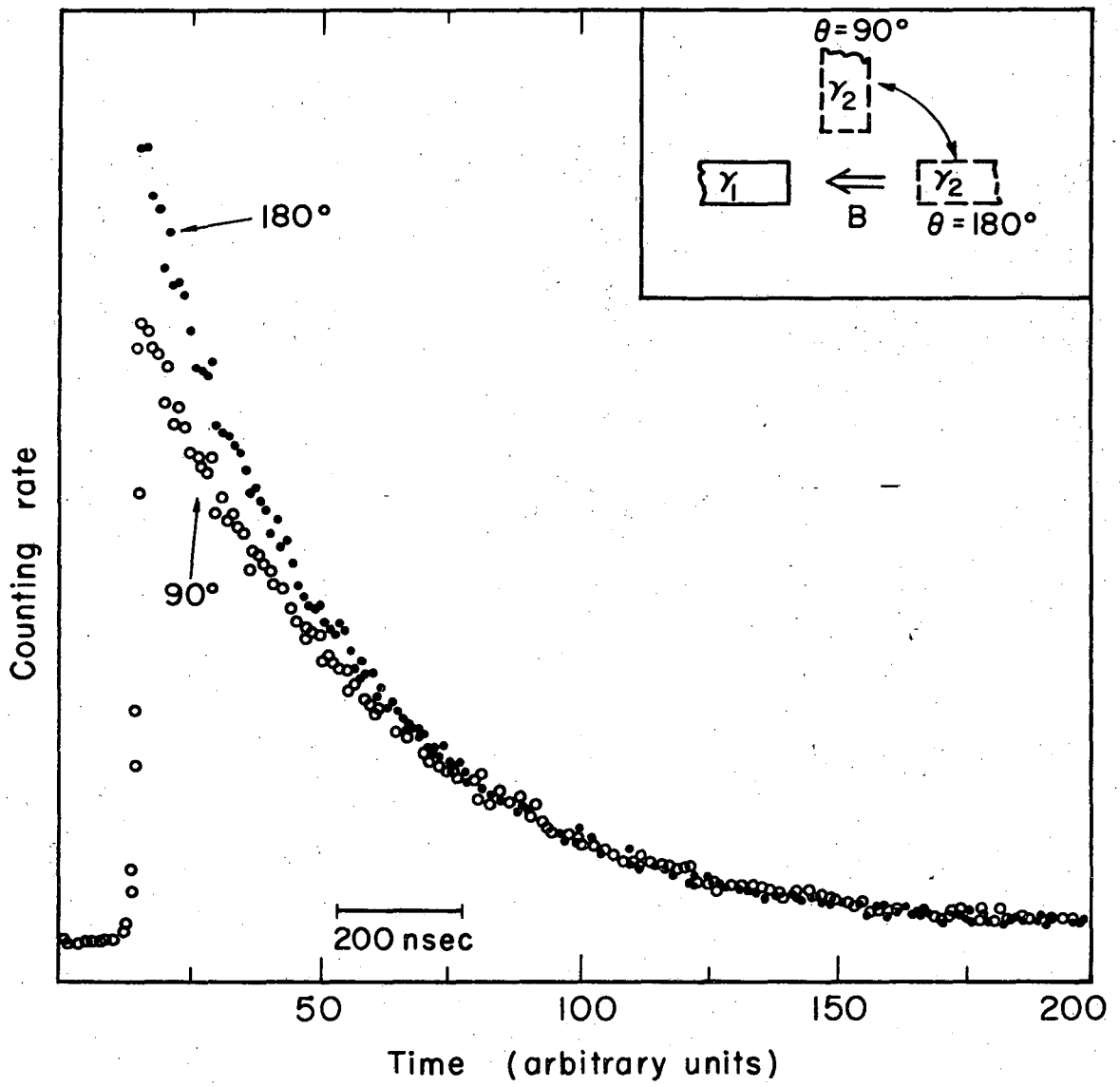
θ=90°
γ2
γ1
B
γ2
θ=180°
180°
90°
Counting rate
200 nsec
50
100
150
200
Time (arbitrary units)
XBL691-1530

Figure VII.6

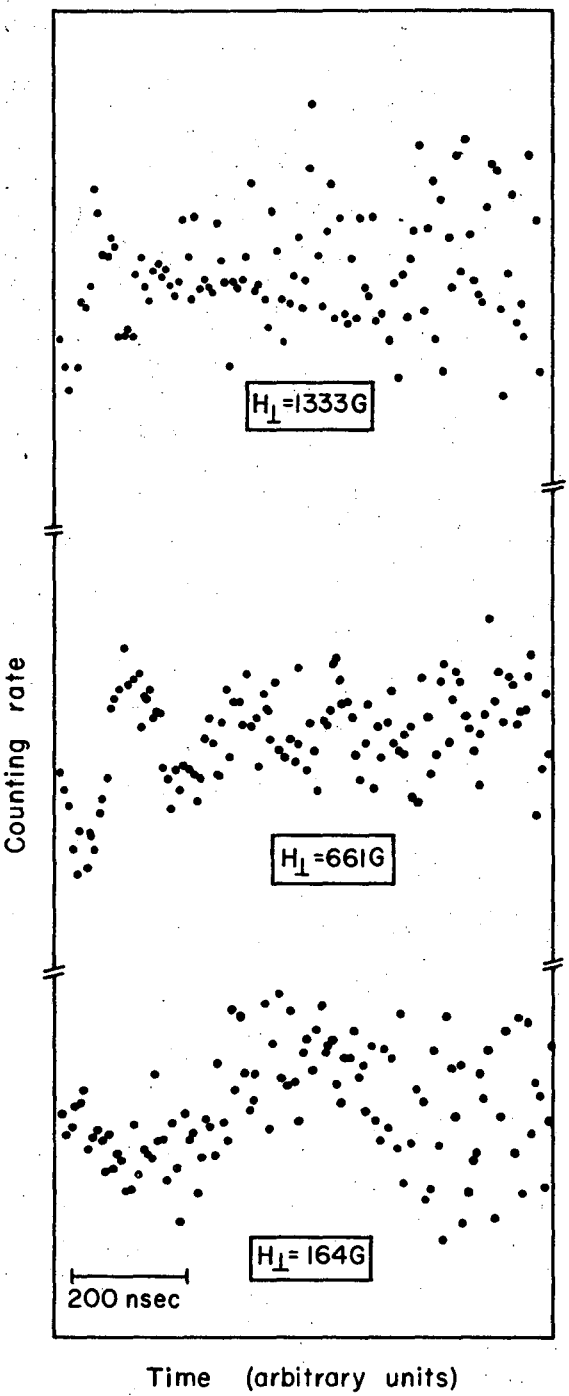
$H_\perp$=1333G
$H_\perp$=661G
$H_\perp$= 164G
200 nsec
Counting rate
Time (arbitrary units)
XBL691-1529

Figure VII.7

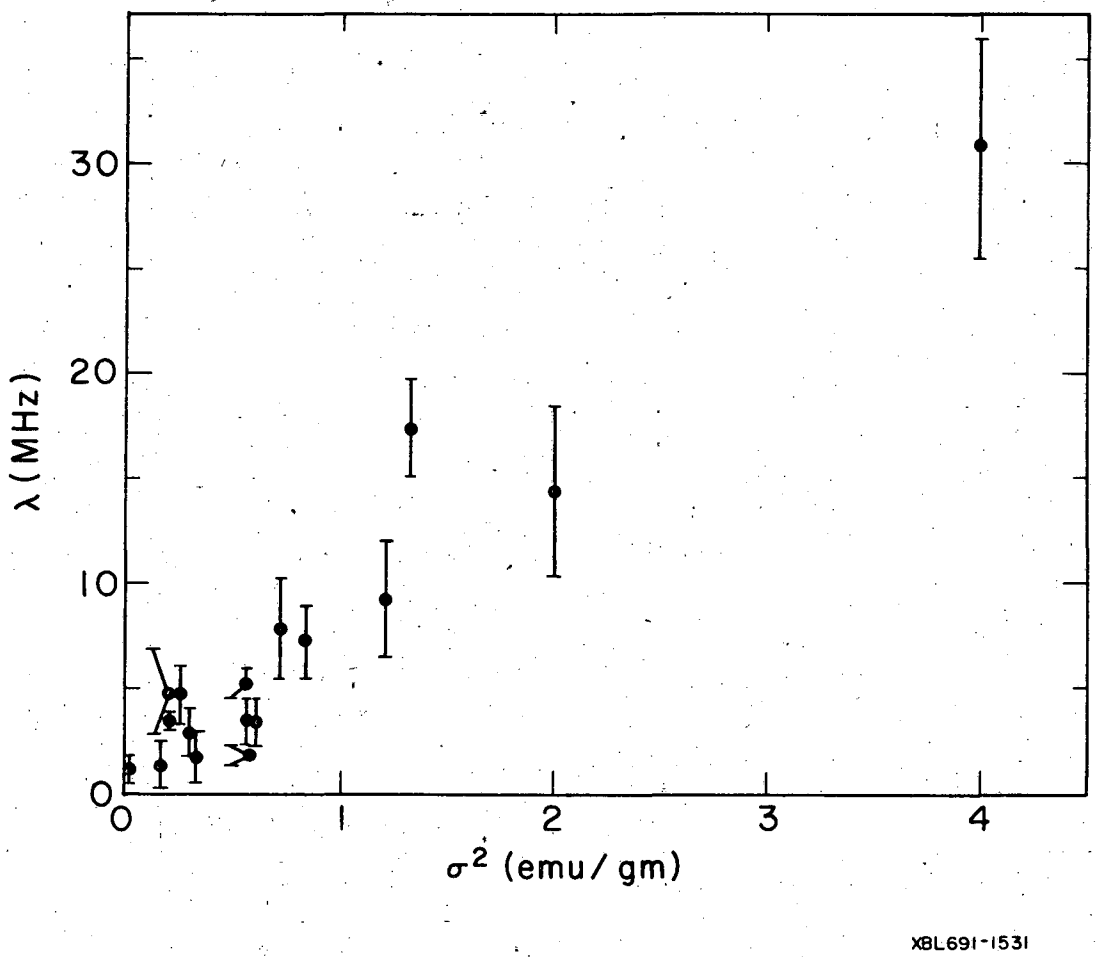

Figure VII.8

VIII. SUMMARY

We have described here the mechanisms responsible for magnetic hyperfine fields in ferromagnets and a molecular field model which predicts the temperature dependence of the hyperfine field for all three systems studied.

For the case of ^{111}CdNi, we were able to make measurements of the hyperfine field accurate to 0.1%, indicating that in favorable cases, time differential perturbed angular correlation measurements are competitive with NMR in accuracy. For this system, we expected no local moment, and none was seen. The hyperfine field was found to be proportional to the lattice magnetization both above and below the Curie point.

For the case of ^{99}RuNi, both hyperfine field systematics and neutron diffraction results led us to expect a local moment. The temperature dependence of the hyperfine field deviated markedly from that of the lattice magnetization both above and below T_c. The molecular field model used to describe the data below T_c required a local moment of approximately 1 Bohr magneton on the Ru atom. For $T > T_c$, further work needs to be done to better establish the nature of the local moment indicated by the time integral perturbed angular correlation measurements.

For ^{100}RhNi, we again expected to find a local moment both from hyperfine field systematics and neutron diffraction results. Above the Curie point, the hyperfine field was proportional to the lattice magnetization, indicating that there is no local moment. This does not preclude the possibility that there is a local moment below T_c. No measurements were

carried out in this region because of insufficient instrumental time resolution. However, this work is now being carried out using the technique of NMR detected by perturbed angular correlations and will determine if there is a local moment below T_c. For this system above T_c we also observed a time dependent interaction, whose temperature and magnetic field dependence is very well described by a molecular field model based on the exchange narrowing of a broadened Zeeman transition. This model predicts that the relaxation rate is proportional to the square of the lattice magnetization. This expectation is borne out by the experimental results.

ACKNOWLEDGMENTS

It is clear that no type of experimental scientific work can be done without technical support. This work was no exception. First of all, then, I would like to express my gratitude to the multitude of un-named members of the Lawrence Radiation Laboratory staff who contributed to this thesis.

I would next like to thank my research director, Professor David A. Shirley, who guided both this research and my scientific development. In addition to suggesting this problem, his ideas have strongly influenced the interpretation of the results.

It is a pleasure to acknowledge the help and friendship of Professor Eckart Matthias, who initiated me into the mysteries of the perturbed angular correlation technique and provided an example of scientific professionalism for me to follow.

It is also a great pleasure to acknowledge my fellow graduate student and office-mate, Dr. James Huntzicker. Our many conversations throughout the five years that I have known him have helped me in understanding many scientific problems better. Our many discussions as friends and comrades-in-arms were equally valuable and illuminating, although they do not appear directly in this thesis. In addition, I would like to thank all the graduate students and postdoctoral fellows in our research group for many stimulating exchanges; in particular, Drs. Helmut Gabriel and Dieter Quitmann, who were of great aid in understanding the ^{100}Rh data.

The help of Mr. Dimitri,"Ed" Voronin and Mr. Richard Reimers in the design and construction of the Gamma furnace is gratefully acknowledged. I would also like to thank Miss Claudette Rugge who wrote many of the computer programs used in the analysis of the data. It is a pleasure to recognize the chemical expertise and readiness to help of Mrs. Winifred Heppler, whose technical skill is matched only by her sunny disposition.

Finally, I would like to thank my parents for their unfailing confidence in me, and the support and encouragement they have provided throughout my educational career.

The financial support of the U. S. Atomic Energy Commission during the last four years is also gratefully acknowledged.

REFERENCES

1. M. A. Grace, C. E. Johnson, N. Kurti, R. G. Scurlock, and R. T. Taylor, Conference du Physique des Basses Temperatures, Paris Sept. 2-8, 1955.

2. G. R. Khutsishvili, Zh. Eksperim. i. Teor.Fiz. 29, 894 (1955); [English translation: Soviet Physics--JETP 2, 744 (1956)].

3. B. N. Samoilov, V. V. Sklyarevskii, and E. P. Stepanov, Zh. Eksperim. i. Teor. Fiz. 36, 644 (1959). [English Translation: Soviet Physics--JETP, 36, 448 (1959)].

4. A. J. Freeman and R. E. Watson, Hyperfine Interactions in Magnetic Materials, in Magnetism, G. T. Rado and H. Suhl, editors, (Academic Press, New York, 1965), Vol. IIA, p. 168ff.

5. V. Jaccarino, in Proceedings of the International School of Physics "Enrico Fermi", XXXVII Course; Theory of Magnetism in Transition Metals, W. Marshall, editor (Academic Press, New York, 1967), p. 335ff.

6. Y. Koi, A. Tsujimura, and J. Hihara, J. Phys. Soc. Japan 19, 1493 (1964).

7. V. Jaccarino, L. R. Walker, and G. K. Wertheim, Phys. Rev. Letters 13, 752 (1964).

8. E. Karlsson, E. Matthias, and K. Siegbahn, editors, Perturbed Angular Correlations (North Holland Pub. Co., Amsterdam, 1964).

9. A. J. Ferguson, Angular Correlation Methods in Gamma Ray Spectroscopy (North Holland Pub. Co., Amsterdam, 1965).

10. H. Frauenfelder and R. M. Steffen, Angular Correlations in Alpha-, Beta-, and Gamma-Ray Spectroscopy, K. Siegbahn, editor (North

Holland Pub. Co., Amsterdam, 1965), p. 997ff.

11. R. M. Steffen, Lectures on Angular Correlations of Nuclear Radiations, (Tata Institute of Fundamental Research, Bombay, 1965).

12. Rolf M. Steffen, Angular Distributions and Correlations of Nuclear Radiations, 3 volumes, unpublished, Purdue University, Lafayette, Indiana, 1965-66.

13. J. W. Gardner, Proc. Phys. Soc. (London) A62, 763 (1949).

14. U. Fano, Phys. Rev. 90, 577 (1953).

15. F. Coester and J. M. Jauch, Helv. Phys. Acta 26, 3 (1953).

16. F. Coester, Phys. Rev. 93, 1304 (1954).

17. Albert Messiah, Quantum Mechanics (North Holland Pub. Co., Amsterdam, 1961), Vol. 1, p. 260ff.

18. Helmut Gabriel, Theory of the Influence of the Environment on the Angular Distribution of Nuclear Radiation, University of California, Lawrence Radiation Laboratory Report UCRL-18496, Sept. 1968.

19. R. Zwanzig, Physica 30, 1109 (1964).

20. A. Abragam and R. Pound, Phys. Rev. 92, 943 (1953).

21. D. A. Shirley, S. S. Rosenblum, and E. Matthias, Phys. Rev. 170, 363 (1968).

22. A. Abragam and M. H. L. Pryce, Proc. Roy. Soc. A205, 135 (1951).

23. D. A. Shirley and G. A. Westenparger, Phys. Rev. 138, A 170 (1965).

24. A. J. Freeman and R. E. Watson, Hyperfine Interactions in Magnetic Materials, op. cit. p. 259 ff.

25. W. Marshall, Phys. Rev. 110, 1280 (1958).

26. G. T. Rado and H. Suhl, editors, Magnetism (Academic Press, New York, 1966), 4 vols; R. M. Bozorth, Ferromagnetism (Van Nostrand Pub. Co., Princeton, 1951); A. H. Morrish, The Physical Principles of Magnetism, (John Wiley and Sons, New York, 1965).

27. J. S. Kouvel and D. S. Rodbell, Phys. Rev. Letters 18, 215 (1967).

28. E. C. Stoner, Proc. Roy. Soc. A165, 373 (1938).

29. H. B. Callen, Phys. Rev. 130, 890 (1963).

30. H. A. Brown and J. M. Luttinger, Phys. Rev. 100, 685 (1955).

31. D. Nagle, P. P. Craig, P. Barrett, D. R. F. Cochran, C. E. Olson, and R. D. Taylor, Phys. Rev. 125, 490 (1962).

32. G. B. Benedek and J. Armstrong, J. Appl. Phys. Suppl. 32, 106S (1961).

33. R. S. Preston, S. S. Hanna, and J. Heberle, Phys. Rev. 128, 2207 (1962).

34. R. L. Streever and L. H. Bennett, Phys. Rev. 131, 2000 (1963).

35. L. H. Bennett and R. L. Streever, J. Appl. Phys. Suppl. 33, 1093 (1962).

36. V. G. Bhide and G. K. Shenoy, J. Phys. Soc. Japan 21, 625 (1966).

37. S. W. Lovesey and W. Marshall, Proc. Phys. Soc. (London) 89, 613 (1966).

38. A. J. Freeman, B. Bogus, and R. E. Watson, Colloq. Intern. Centre Natl. Rech. Sci. (Paris), # 164 (1966).

39. A. M. Clogston, V. Jaccarino, and Y. Yafet, Phys. Rev. 134A, 650 (1964).

40. M. F. Collins and G. G. Low, Proc. Phys. Soc. (London) 86, 535 (1965).

41. I. A. Campbell, Proc. Phys. Soc. 89, 71 (1966).

42. H. Callen, D. Hone, and A. Heeger, Phys. Letters 17, 233 (1965).

43. D. Hone, H. Callen, and L. R. Walker, Phys. Rev. 144, 283 (1966).

44. G. G. Low, Phys. Letters 21, 497 (1966).

45. P. W. Anderson and P. R. Weiss, Revs. Mod. Phys. 25, 111 (1953).

46. Ryogo Kubo and Kazuhisa Tomita, J. Phys. Soc. Japan 9, 888 (1954).

47. B. G. Silbernagel, V. Jaccarino, P. Pincus, and J. H. Wernick, Phys. Rev. Letters 20, 1091 (1968).

48. Ryogo Kubo, A Stochastic Theory of Line Shape and Relaxation, in, Fluctuation, Relaxation, and Resonance in Magnetic Systems, D. Ter Haar, editor (Plenum Press, New York, 1961), p 23ff.

49. E. Jacobi, Helv. Phys. Acta 22, 66 (1949).

50. C. M. Lederer, J. M. Hollander, and I. Perlman, Table of Isotopes, 6th edition (John Wiley and Sons, New York, 1967), p. 252.

51. E. Matthias, L. Bostrom, A. Maciel, M. Salomon, and J. Lindquist, Nucl. Phys. 40, 656 (1963).

52. E. C. O. Bonacalza and G. B. Holm, Phys. Letters 4, 343 (1963).

53. E. Matthias, S. S. Rosenblum, and D. A. Shirley, Phys. Rev. Letters 14, 46 (1965).

54. P. Weiss and R. Forrer, Ann. Phys. (Paris) 15, 153 (1926).

55. Table of Isotopes, op. cit., p. 235

56. E. Matthias, S. S. Rosenblum, and D. A. Shirley, Phys. Rev. 139, B532 (1965).

57. J. I. Budnick and J. J. Murphy, private communication.

58. H. Kubo, M. Kontani, and J. Itoh, J. Phys. Soc. Japan 22, 929 (1967).

59. C. Sadron, Ann. Phys. (Paris) 17, 371 (1932).

60. J. S. Evans, E. Kashy, R. A. Naumann, and R. F. Petry, Phys. Rev. 138, B 9 (1965).

61. E. Matthias and D. A. Shirley, Nucl. Instr. Methods 45, 309 (1966).

62. M. Kontani and J. Itoh, J. Phys. Soc. Japan 22, 345 (1967).

63. D. Quitmann and R. Pollak, private communication.

64. E. Matthias, Angular Correlation and Mössbauer NMR, in Hyperfine Structure and Nuclear Radiations, E. Matthias and D. A. Shirley, editors (North Holland Pub. Co., Amsterdam, 1968), p. 815 ff.

65. M. B. Salamon, Phys. Rev. 155, 224 (1967).

FIGURE CAPTIONS

Fig. II.1 A two photon cascade described by the angular correlation formalism.

Fig. III.1 Variation of H_{hf} with atomic number for 4d and 5d solutes in iron showing the abrupt increase above CEP estimates.

Fig. III.2 Derived localized moments for solutes in iron.

- O This work
- ● Ref. 40
- ■ Ref. 41

Fig. IV.1 Block diagram of time-differential perturbed angular correlation spectrometer using NaI(Tl) detectors.

Fig. IV.2 Block diagram of time-differential perturbed angular correlation spectrometer using Ge(Li) detectors.

Fig. IV.3 Block diagram of a time integral perturbed angular correlation spectrometer using NaI(Tl) detectors.

Fig. IV.4 Early furnace and angular correlation apparatus.

Fig. IV.5 Vertical sectional view of Gamma furnace.

Fig. IV.6 Gamma furnace with 135° window assembly in place and 180°-90° window assembly on table.

Fig. IV.7 Typical experimental arrangement showing the Gamma furnace inside the small electromagnet (Sec. IV.B.2) with two Ge(Li) detectors in counting position at a relative angle of 135°.

Fig. V.1 Partial decay scheme, $^{111}In \rightarrow {}^{111}Cd$.

Fig. V.2 Gamma ray spectrum of ^{111}Cd.

Fig. V.3 Time differential angular correlation for ^{111}CdNi below the Curie point. The time spectra were recorded at a detector angle of 180° and no external field was used. The modulation pattern is characteristic of a randomly oriented magnetic interaction. The solid curve represents the weighted least-squares fit to the data of Eq. (V.1).

Fig. V.4 Reduced hyperfine field vs. reduced temperature for ^{111}CdNi below the Curie point. (T_c=627.2°K, the value for pure Ni.) ——— $\frac{\sigma}{\sigma_0}$ for pure Ni, Weiss and Forrer (Ref. 54);----- $\frac{\sigma_1}{\sigma_0}$ Lovesey and Marshall (Ref. 37), showing demagnetization of first nearest neighbors by a nonmagnetic impurity.

Fig. V.5 Time differential perturbed angular correlation spectra for ^{111}CdNi with $T > T_c$. The function,

$$R = [W_\perp(\tfrac{3\pi}{4},t,+H_{ext}) - W_\perp(\tfrac{3\pi}{4},t,-H_{ext})]/[W_\perp(\tfrac{3\pi}{4},t,+H_{ext}) + W_\perp(\tfrac{3\pi}{4},t,-H_{ext})]$$

is least-squares fitted to Eq. (II.19) with $k_{max} = 2$.

Fig. V.6 Temperature dependence of $\beta = H_{eff}/H_{ext}$, for ^{111}CdNi, measured with a polarizing field of 19.5 kOe. The curve was calculated using Eq. (V.2) with $H_{hf}(0)$=68.52 kOe.

Fig. VI.1 Partial decay scheme for ^{99}Rh → ^{99}Ru.

Fig. VI.2 Relevant portion of the gamma ray spectrum of ^{99}Ru taken with a Ge(Li) detector.

Fig. VI.3 Time-differential perturbed angular correlation spectra for ^{99}RuNi with a polarizing field of 5.00 kOe. The indicated hyperfine fields have been calculated using g=0.189(4), Ref.56.

Fig. VI.4 The data of Fig. VI.3 at 4.2°K fitted with a curve calculated from the spectrum of Budnick and Murphy (Ref. 57) shown in the inset. In the inset, the bar graphs show the positions and relative intensities chosen for the lines and the dashed line shows the resulting calculated fit which we Fourier transformed.

Fig. VI.5 Reduced hyperfine vs. reduced temperature for ^{99}RuNi below the Curie temperature (T_c=610°K for the 1 at.% alloys used) and $H_{hf}(0)=H_{hf}(4.2)$=217.2 kOe. The broken curves are theoretical fits based on Eq. (II.12). The values of the parameters are given in Table VI.2.

Fig. VI.6 Temperature dependence of $\beta=H_{eff}/H_{ext}$, for ^{99}RuNi in an external field of 19.5 kOe. □ measured by time-differential perturbed angular correlation; ○ measured by time-integral perturbed angular correlation.

Fig. VII.1 Partial decay scheme, ^{100}Pd → ^{100}Rh.

Fig. VII.2 Relevant portion of the gamma spectrum of ^{100}Rh taken with a Ge(Li) detector.

Fig. VII.3 Data taken in an applied transverse field, H=1614 gauss with detectors at 180° angle. The decay due to the nuclear level lifetime, τ_N, in Eq. (VII.1) has been removed.

Fig. VII.4 Data taken in an applied transverse magnetic field H=810 gauss with detectors at a 180° angle. The decay due to the nuclear level lifetime, τ_N, in Eq. (VII.1) has been removed.

Fig. VII.5 Temperature dependence of $\beta=H_{eff}/H_{ext}$ for ^{100}RhNi. The solid curve is calculated assuming H_{hf} is proportional to the lattice magnetization.

Fig. VII.6 Raw data from a typical decoupling experiment described by Eq. (VII.2). The inset shows the experimental geometry.

Fig. VII.7 Data taken at a constant temperature, T=365°C, and varying transverse magnetic fields at a detector angle, $\theta=135°$. The function R, described under Fig. V.5, is plotted.

Fig. VII.8 Nuclear relaxation rate for ^{100}RhNi for $T > T_c$ as a function of the square of the lattice magnetization.

TECHNICAL INFORMATION DIVISION
LAWRENCE RADIATION LABORATORY
UNIVERSITY OF CALIFORNIA
BERKELEY, CALIFORNIA 94720